

FABRICATION AND CHARACTERIZATION OF MACROPOROUS SILICON

Dissertation

zum Erlangen des akademischen Grades

Doctor rerum naturalium

(Dr. rer. nat.)

vorgelegt der

Naturwissenschaftlichen Fakultät II

der Martin-Luther-Universität Halle-Wittenberg

von

Herrn Dipl. Phys. Andreas Langner

geb.: 04.12.1978 in Berlin

Gutachter:

1. Prof. Dr. U. Gösele
2. Prof. Dr. H. Föll
3. Prof. Dr. H. Graener

Halle (Saale), 31. März 2008

Verteidigt am 01. Juli 2008

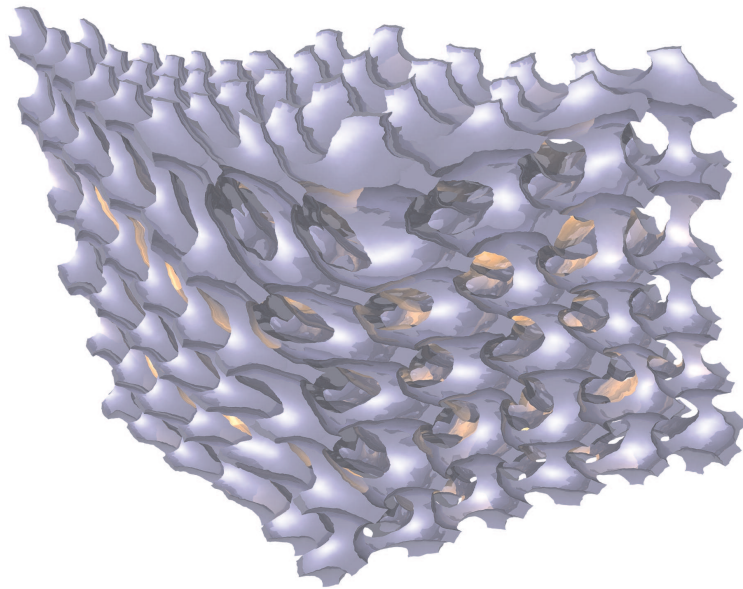
urn:nbn:de:gbv:3-000014114

[<http://nbn-resolving.de/urn/resolver.pl?urn=nbn%3Ade%3Agbv%3A3-000014114>]

*Between nature and me there is a giant battle going on
because I have to improve nature.*

*Zwischen der Natur und mir ist eine große Schlacht im Gange,
denn ich muss die Natur verbessern.*

Salvador Dalí



A three-dimensional photonic crystal structure as Salvador Dalí might have seen it.

*Don't fool yourself with wanting to improve mistakes in nature.
There is no mistake in nature, the mistake is in yourself.*

*Mach Dir nicht vor, Du wolltest Irrtümer in der Natur verbessern.
In der Natur ist kein Irrtum, sondern der Irrtum ist in dir.*

Leonardo da Vinci

Contents

Nomenclature	1
Preface	3
1 Macroporous Silicon	5
1.1 Porous Silicon	5
1.2 Electrochemical Macropore Formation in n-Type Silicon	6
1.3 Post Treatment of Macroporous Silicon	15
1.3.1 Oxidation	15
1.3.2 Isotropic Etching	15
1.3.3 Anisotropic Etching	16
1.4 Alternative Methods to Fabricate Ordered Porous Structures	17
1.4.1 Top-down	17
1.4.2 Bottom-up	17
2 Macroporous Silicon in Materials Science	19
2.1 Various Shapes of Macroporous Silicon	19
2.2 Surface Treatment and Replication with Atomic Layer Deposition	21
3 Photonic Crystals	25
3.1 Introduction	25
3.2 Theory: Interaction of Light with Matter	27
3.3 Calculation of Photonic Band Structures	28
3.4 The Photonic Band Gap	30
3.4.1 Selected Designs with a Complete Photonic Band Gap in 3D	30
3.4.2 2D Photonic Crystals	32
3.4.3 Defects in Photonic Crystals	33
3.4.4 3D Simple Cubic Photonic Crystal	34
3.5 Fourier Transform-Infrared Spectrometry	36
3.6 Summary	37
4 Etching Macroporous Silicon in the Sub-Micrometer Range	39
4.1 Etching of Straight Pores	40
4.2 Etching of Modulated Pores	42
4.3 Influence of the Lithography	43

4.4	Etching of Strongly Modulated Pores	45
4.5	Space Charge Region and Breakdown	51
4.6	Photonic Stop Band at 1.5 μm Wavelength	55
4.7	Summary	56
5	Photonic Crystals Beyond the Photonic Band Gap	59
5.1	Introduction	59
5.1.1	The Complete Dispersion Relation of a 2D Hexagonal Lattice	60
5.1.2	Determination of Beam Propagation	61
5.1.3	Selected Effects Related to the Dispersion Relation of Photonic Crystals	64
5.2	'Real' 3D Photonic Crystal Structure	67
5.2.1	Derivation of the Model Structure	67
5.2.2	Results of the Calculation	68
5.3	Discussion	70
5.4	Summary	73
6	Experimental Characterization of the Refraction Properties	75
6.1	Introduction	75
6.2	Experimental Setup	76
6.3	Results and Discussions	77
6.4	Summary and Outlook	86
	Conclusions	87
	Bibliography	89
	Acknowledgment	99
	Statutory Declaration	101
	Curriculum Vitae	103
	Scientific Contributions	105

Nomenclature

2D	two-dimensional
3D	three-dimensional
ALD	atomic layer deposition
BZ	Brillouin zone
CVD	chemical vapor deposition
EFC	equi-frequency contour
FDTD	finite-difference time-domain
FT-IR	Fourier transform-infrared
HF	hydrofluoric acid
KOH	potassium hydroxide
MCT	mercury cadmium telluride
NIM	negative-index material
PVC	polyvinyl chloride
RIE	reactive-ion etching
SCR	space charge region
SEM	scanning electron microscope
TE	transverse electric
TM	transverse magnetic

Preface

Since time immemorial, silicon compounds served the mankind as valuable source of progress. About one quarter of earth's crust is silicon. Already in the ancient world silicon compounds were used as building material for edifices, streets, or pottery. As a pure element in crystalline form it was first produced in 1854 by Henri Étienne Sainte-Claire Deville via electrolysis. After the invention of the transistor in 1947 and the first integrated circuit in 1957 it took another decade before silicon became the principal component for integrated circuits instead of germanium.

The efforts in the second half of the last century were dedicated to shrinking integrated circuits and increasing their performance. Naturally, there are physical limits in miniaturization processes. Thus, beside geometrical scaling new concepts were introduced. For instance, enhanced charge carrier mobility due to mechanically strained silicon or alternative gate dielectric materials such as hafnium oxide [1]. Furthermore, other materials like carbon nanotubes, III-V compounds or germanium are investigated as well.

With the electronic age also the global interconnection grew and the fast transfer of large amount of data gained importance in our everyday life. Nowadays, mostly photons instead of electrons are used as information carriers due to their lower interaction with matter resulting in higher speed and lower power consumption. Silicon with its indirect electronic band gap has only poor light emitting capabilities. Traditionally, III-V compounds are used in optoelectronic devices. In recent years, however, the dogma was successfully disproven that silicon is not suited for the photonic age. Doped or nanocrystalline silicon can be used for photon generation [2, 3]. Stimulated Raman scattering is used to amplify light in silicon and thus an all-silicon laser was realized [4, 5, 6]. A modulator is necessary to encode a light wave with information [7, 8] while for the detection silicon germanium detectors are used [9]. Meanwhile, a silicon modulator with 40 gigabit per second transfer rate has been developed at the Photonics Technology Lab of Intel and in combination with III-V compounds very large scale photonic circuits will be realized very soon [10].

Beside active optical elements that alter the energetic state of a photon, passive elements are of importance, too. An electron in an integrated circuit is guided between electronic devices by an applied potential in a metallic conductor. Similar tasks have to be fulfilled for a photon in an optical circuit. Thereby, a strong coupling with the photon without attenuation of its energy is required. While a charged particle is influenced by an electric field, a photon will always obey Fermat's principle saying that its optical path length must be extremal. Thus, the challenge is to design an environment for the photon which makes it run the proper way. This task can be fulfilled by artificially produced dielectric structures, the photonic crystals. Silicon with its high dielectric constant seems to be an ideal candidate for this purpose, too. But it has to be combined

in an ordered manner with a material of low dielectric constant, for instance air.

Parallel to the invention of electronic integrated circuits in silicon also various porous forms of silicon have been investigated. Electrochemical processes cause the formation of porous silicon. Nowadays, the formation of pores in silicon can be induced in a controlled manner to fabricate highly ordered porous structures. The present work will deal with a certain form of porous silicon: Macroporous silicon. Formed in a controlled manner it can be used to create highly ordered artificial porous structures. The aspects of fabrication will be presented in the first chapter. In the second chapter the application of macroporous silicon as a versatile template material in materials science is highlighted. Apart from various shapes that can be achieved with macroporous silicon, its usage in conjunction with atomic layer deposition will be demonstrated.

The main part of the work, however, is dedicated to silicon photonics. After an introduction to photonic crystals in the third chapter the fourth chapter will deal with electrochemical pore formation on a size scale below one micrometer. The motivation for this topic derives from the demands associated with potential applications in telecommunication industry. Experimental results regarding the pore formation as well as theoretical considerations will be presented and discussed.

Beside the fabrication process of macroporous silicon a further aspect shall be considered in this work: The optical utilization of etched three-dimensionally modulated macroporous silicon samples. This task will be treated theoretically in chapter five as well as experimentally in chapter six. Based on the design of etched three-dimensional structures their dispersion relation is calculated. The analysis of the obtained results will reveal the refraction properties of the sample under consideration and serve as an indication for the design of the subsequent experiment. The data obtained by the experiment, in turn, can be discussed comparatively to the theoretical findings since the theoretical findings are based on the structure of the considered sample. In the end concluding remarks will complete the circle of fabrication and characterization of macroporous silicon.

Chapter 1

Macroporous Silicon

Porous materials are characterized by a large surface-to-volume ratio. This makes them very attractive for scientific and technological purposes because the entire bulk of a porous solid can interact with atoms and molecules. Examples for porous materials are zeolites, porous metal-organic frameworks, and aerogels. Typical applications can be found in catalysis and particle separation, in adsorption and storage, or in tissue engineering and environmental technology.

Beside the increased surface-to-volume ratio, controlling the size of the building blocks (e.g. the walls as well as the voids) is of interest, too. This can improve the performance of the structures and open up new fields of application, e.g. as template materials or as photonic crystals. A review on ordered porous materials and their applications can be found in Ref. [11].

The material system utilized in this work is called macroporous silicon and is considered in more detail in this chapter. After a short introduction to porous silicon, the necessary background is provided to get familiar with major aspects of fabrication of macroporous silicon. Finally, a selection of alternative methods for the fabrication of ordered porous materials is given.

1.1 Porous Silicon

The formation of porous silicon in an anodization setup is known since the 1950s from the pioneering work by Uhlir and Turner at Bell Labs [12, 13]. It was observed that smooth etching occurs at higher current densities with a dissolution valence¹ of four. At lower current densities the dissolution valence was about two and etching took place under hydrogen evolution. After the electrochemical etching the samples exhibited a non-reflecting dark film. In the following decades the electrochemistry of silicon and the formation of porous silicon was a research topic of raising interest.

The etching of silicon and therefore the “growth” of pores with a certain diameter covers several orders of magnitude. According to the International Union of Pure and Applied Chemistry (IUPAC) nomenclature for porous materials [14], structures with a pore width below two nanometers are called microporous. The mesoporous structures range from two to fifty nanometers. Bigger pores are referred to as macropores.

The obtained pore morphology of porous silicon is dependent on a number of parameters. These are for instance the properties of the material (doping, resistivity, and orientation), the

¹The dissolution valence gives the ratio of exchanged charge carriers per dissolved silicon atom.

composition of the electrolyte (organic, inorganic, concentration, and additives), as well as external parameters such as temperature, voltage, and illumination intensity. Among the different electrolytes hydrofluoric acid (HF) is most prominent. While silicon dioxide is dissolved in HF, silicon requires to be anodically biased to dissolve efficiently.

The formation of microporous silicon is a result of quantum confinement effects [15, 16]. It is independent of doping and crystal orientation and a layer of microporous silicon often covers the walls of meso- or macropores. For the mesoporous and macroporous structures the formation of a space charge region (SCR) in an electrochemical setup is necessary. Mesopores are formed mainly by tunneling processes within the SCR [17] while macropores are formed as a result of thermionic emission (for p-type doping) [18] or the collection of minority charge carriers (for n-type doping) [19, 20]. The growth direction of meso- and macropores is dependent on crystal orientation and shows a preference of the $\langle 100 \rangle$ direction.

Detailed information on porous silicon and its electrochemistry can be found in review articles (e.g. [21, 22]) or books (e.g. [23, 24]). The macropore formation in n-type silicon will be discussed in the frame of this work. The most important points of this special form of porous silicon formation will be introduced in the following sections.

1.2 Electrochemical Macropore Formation in n-Type Silicon

Among the different ways of fabricating porous silicon, macroporous structures etched in an aqueous solution of HF allow to design the sample parameters specifically. Since its invention in 1990 [19] this method has developed to a well understood and viable tool for device and template fabrication. One significant advantage is the possibility to produce ordered pore arrays with defined diameters and lengths. The pore diameters can be adjusted between a few hundred nanometers and several micrometers. The potential to etch pores of a few hundred micrometers in depth is especially remarkable. Thus, aspect ratios of 500 : 1 and even more can be obtained without losing the ordering and the defined shape of the pores. The underlying mechanisms of macropore formation in n-type silicon exposed to aqueous HF will be discussed in more detail in the following.

Space Charge Region

Starting with the bulk material, structures are designed by dissolving part of the silicon – a typical top-down approach. In Fig. 1.1a a sketch of an anodization setup is shown. The silicon wafer is clamped between two parts of a polyvinyl chloride (PVC) cell which is inert to low concentration of HF. One side – herein after called front side – of the wafer is exposed to HF. Such an intersection between a moderately doped semiconductor and an electrolyte resembles a behavior similar to a Schottky contact. The electrochemical potential between both materials adjusts by forming a thin (approximately 0.3 nm) Helmholtz double layer. In the electrolyte, the charge carriers (ions) are mobile and can therefore screen the electric field within a few nanometers. In the semiconductor free charge carriers can only be generated from the fixed dopants. The density of these dopants is much lower than the charge carrier density in the electrolyte. Consequently, the electric field evolves inside the silicon and forms a SCR (Fig. 1.1b). For the case of a planar

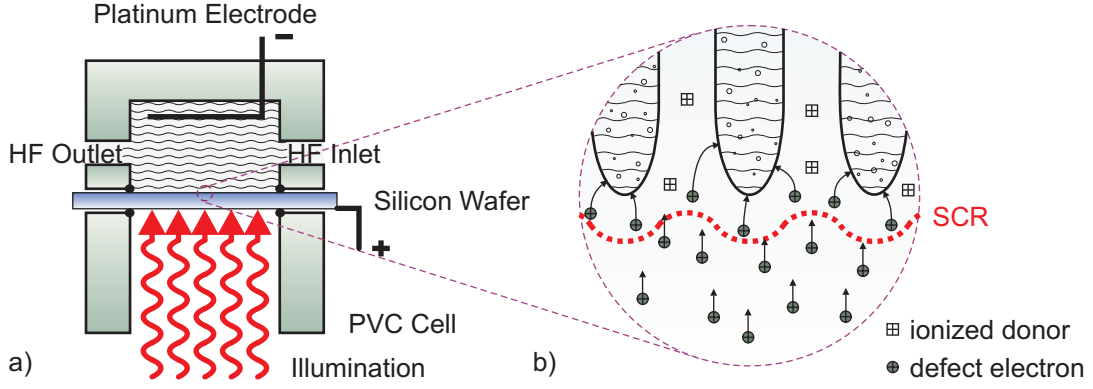


Figure 1.1: a) Sketch of an electrochemical etching setup for the growth of macroporous silicon. The silicon is anodically biased, the front side is exposed to HF and the back side is illuminated to generate electron-hole pairs. b) An enlarged view of the situation at the bottom of the pores: The SCR extends to the red line in the silicon. Hence, this region is depleted and an electric field forms that focuses the minority charge carriers to the pore tips.

interface, the width of this region W_{SCR} can be defined as

$$W_{\text{SCR}} = \sqrt{\frac{2\epsilon\epsilon_0 V}{eN_D}} \quad (1.1)$$

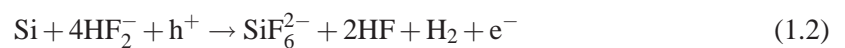
where $\epsilon = 11.9$ is the dielectric constant of silicon, ϵ_0 the permittivity of the free space, e the elementary charge and N_D the density of dopants. The voltage V is the difference between the built-in potential V_{bi} of the silicon-HF contact (about 0.5 V) and the external applied voltage V_{appl} and the thermal voltage kT/e : $V = V_{\text{bi}} - V_{\text{appl}} - kT/e$. There is no further reference electrode necessary in this setup because the voltage drop over the SCR is significantly larger than the electrochemical potential. Furthermore, the chemical reaction is limited by the charge carriers generated due to the back side illumination.

Although Eq. 1.1 is only valid for a one-dimensional geometry, it is a good approximation for the width of the SCR for pores within the micrometer range. For example, a moderate doping density of 10^{15} cm^{-3} and a voltage of 2 V would result in a width of the SCR of $1.6 \mu\text{m}$.

Electrochemistry

In Fig. 1.2 the current-voltage profile of an n-type silicon-electrolyte junction is depicted. The forward-biased regime (negative potential) is characterized by a charge carrier flow of majority charge carriers (i.e. electrons in n-type silicon) from the silicon to the electrolyte. This case is of minor interest because it only leads to a reduction of H^+ -ions and hence hydrogen is produced in the electrolyte.

In the anodic regime where the voltage is reverse-biased, two different processes have to be distinguished. The transition between these two regions is defined by a critical current density J_{PS} . It was found experimentally that J_{PS} is dependent on HF concentration and temperature [20]. For current densities below J_{PS} divalent dissolution of silicon takes place:



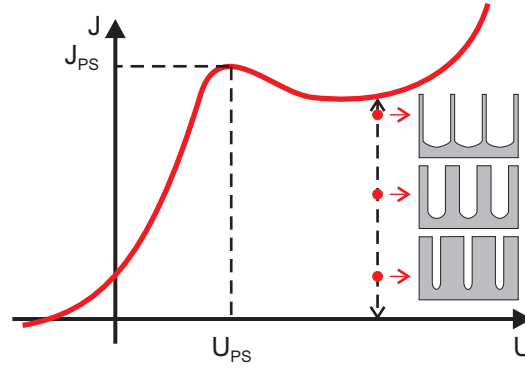
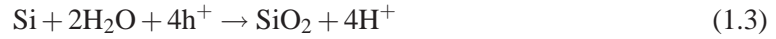
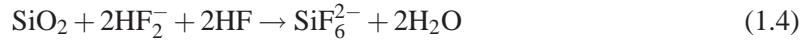


Figure 1.2: Schematic of the current-voltage curve of an illuminated reverse-biased silicon-HF contact. The critical current density J_{PS} marks the transition from divalent to tetravalent dissolution. The limitation of the overall current density to values below J_{PS} by illumination from the back side adjusts the diameter of the pores.

Thereby, two charges per dissolved silicon atom are measured in the electric circuit: One defect electron (h^+), moving from the silicon to the electrolyte, and one electron (e^-), moving in the opposite direction through the interface. Current densities exceeding the critical value J_{PS} are leading to a tetravalent dissolution. First, the silicon is oxidized anodically whereby four holes are consumed:



The formed silicon dioxide is chemically dissolved by the HF containing electrolyte:



Both, the divalent and the tetravalent reaction lead to a dissolution of silicon. The dissolution product of silicon in HF is always fluosilicic acid (in a dissociated state: $\text{H}_2\text{SiF}_6 \rightarrow \text{SiF}_6^{2-} + 2\text{H}^+$). While the tetravalent dissolution shows no dependence on crystal orientation, the divalent dissolution does. Thus, only the divalent reaction (Eq. 1.2) leads to a formation of pores in silicon. During the divalent dissolution the whole surface is covered by Si-H. In the presence of fluoride the Si-H bonding with a bonding energy of 3.5 eV is replaced by the stronger Si-F bonding (6 eV). The strong polarizing effect of fluor leads to a weakening of the silicon backbonds. HF and H_2O are then breaking the bonds and the surface is H-terminated again. Fig. 1.3 reveals the reason for the anisotropic behavior of the divalent dissolution: In the (110) plane and (100) plane the polarization force of the fluor atom is sufficient to break the backbonds while in the (111) plane the silicon atom is strongly bond.

During the tetravalent reaction the silicon is oxidized anodically. Since this oxide formation is independent of the crystal geometry, the tetravalent dissolution is isotropic.

Etching Speed

During the etching of macropores the current density at the pore tip is always J_{PS} . It is limited by reaction kinetics and mass transport in the electrolyte. Therefore, J_{PS} is dependent on the HF concentration c_{HF} and electrolyte temperature T . The following correlation was found

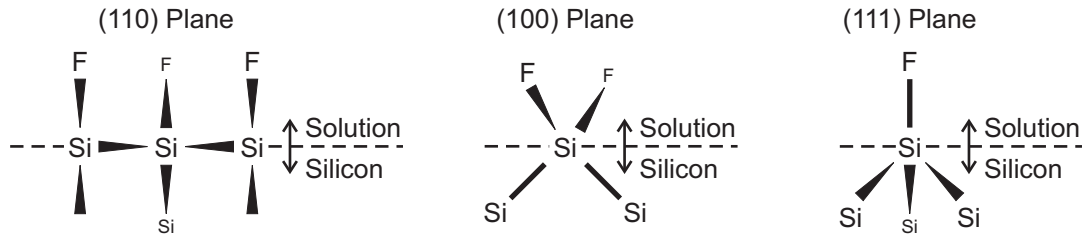


Figure 1.3: Anisotropy of silicon dissolution during the divalent reaction. The polarizing effect of the fluor atom is responsible for the dissolution of silicon. Due to the higher number of silicon backbonds in the (111) plane the polarizing effect is insufficient to dissolve the silicon. [25]

experimentally:

$$J_{PS} = C_{PS} c_{HF}^{1.5} \exp(-E_a/kT) \quad (1.5)$$

with $C_{PS} = 3300 \text{ A cm}^{-2} \cdot (\% \text{HF})^{-1.5}$ and an activation energy of $E_a = 0.343 \text{ eV}$. HF concentration and temperature determine the magnitude of J_{PS} and thus the etching speed of the whole process. Increasing both quantities (c_{HF} and T) enhances the etching speed. However, it has turned out that moderate values will give the best results. For example, an etching speed of nearly $1 \mu\text{m/min}$ is obtained for an acid concentration of 5 wt% and an electrolyte temperature of 10°C .

Porosity

As mentioned before, n-type doped silicon is used in this process. Therefore, the defect electrons (holes) which are needed in the dissolution process (Eqs. 1.2 and 1.3) are the minority charge carriers. Generated by, for example, back side illumination with an LED-array working at a wavelength of 780 nm (cf. Fig 1.1), the minority charge carriers are obtained from electron-hole pairs. Due to the concentration gradient, the holes will diffuse towards the front side and take part in the dissolution of silicon.

For sufficiently high current densities the dissolution reaction is limited by the chemistry. This situation is represented by the red curve in Fig. 1.2. Lower currents can be adjusted by a decreased back side illumination intensity. Experiments have shown that the etching speed is unaffected by an altered current density. With less charge carriers available, however, the etched area decreases because the current density at the pore tip is still J_{PS} . Therefore, the porosity p of the sample is altered, too. This correlation is summarized in the following equation:

$$p = \frac{J}{J_{PS}} \quad (1.6)$$

This means that the porosity p of a sample can be adjusted by the current density J . It is controlled by the back side illumination intensity independently from the voltage.

Pore Wall Passivation

The width of the SCR is a critical factor in the etching process. It prevents the pore walls from being post-etched. In the SCR there are no free charge carriers available. The silicon is depleted and therefore no charge transfer through the silicon-electrolyte interface occurs. As can be seen in Eq. 1.1 the width W_{SCR} can be adjusted by the voltage V and the doping density N_D . Controlling

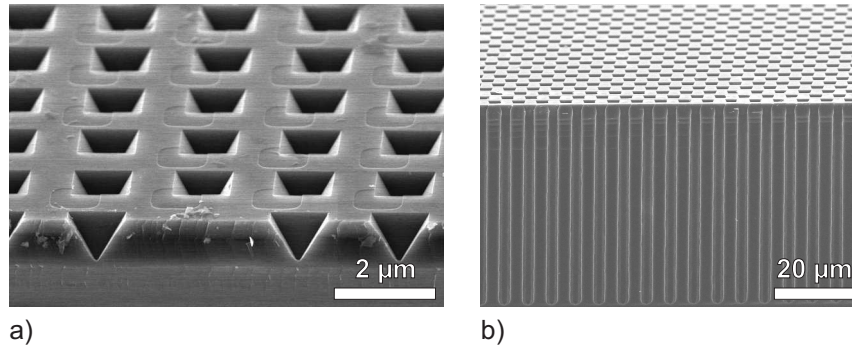


Figure 1.4: Scanning electron microscope (SEM) images of macroporous silicon: a) Bird's eye view of KOH etch pits formed at the silicon surface prior to the etching process in a square arrangement with a lattice constant of $a = 2\text{ }\mu\text{m}$ (taken from Ref. [26]). b) Straight pores with $50\text{ }\mu\text{m}$ in depth etched into silicon with a predefined hexagonal lattice of $6\text{ }\mu\text{m}$ pore-to-pore distance.

W_{SCR} by the voltage is limited to smaller changes only: A decreased voltage will diminish the focusing effect of the electric field on the charge carriers towards the pore tips. In contrast, an increased voltage leads to a higher amount of dark currents that cannot be controlled. Consequently, the preferred way is to tune W_{SCR} by the doping density of the material.

Material

The silicon wafers used are (100) oriented. Phosphorus is used as a dopant for a homogeneous n-type doping of the wafers. Since the minority charge carriers are generated at the back side they have to diffuse towards the front side where they promote the dissolution of silicon. Thus, the lifetime has to be long enough to allow for diffusion lengths in the order of the wafer thickness (typically 500 to 600 μm for a six inch wafer). To prevent recombination of electron-hole pairs monocrystalline silicon grown in a float-zone process is preferred because of its high degree of purity.

In order to establish an ohmic contact, the back side of the wafer is highly doped (n^+) with a doping concentration in excess of 10^{19} cm^{-3} . In contact with a metal clamp the back side establishes an ohmic contact transparent for illumination. Furthermore, the induced electronic band bending supports charge carrier separation.

Lithography

In contrast to the anodization of metals (e.g. aluminum, titanium) the growth of macropores in silicon is not a self-ordering process. The pores do not form a periodic arrangement naturally. The pore position, however, can be predefined by lithography and subsequent etching in potassium hydroxide (KOH). The obtained etch pits work as nucleation sites for the pore growth (Fig. 1.4a). The advantage of this process is that there is no restriction to a hexagonal pore arrangement only. Rather, the pre patterning can be varied in the pore arrangement and pore size and hence allows for specifically designed samples.

Although the etching process is not a self-ordering process, it is a self-organizing one. For a given doping density, applied voltage and back side illumination an average porosity and pore diameter will arise. Therefore, the lithography has to fit with the intrinsic material parameters.

The passivation of the pore walls and thus the prevention of the pore walls from being post-etched is a consequence of the SCR. For a stabilized pore growth the remaining silicon between neighboring pores should be completely depleted from charge carriers. From this requirement a rule of thumb can be derived for the lattice constant of the lithography: The interpore distance a has to be chosen twice as large as the width W_{SCR} . It implies, that higher doped material is preferentially used for smaller interpore distances and vice versa.

For a given lattice geometry the porosity p as defined by Eq. 1.6 determines the ratio of the pore area to the whole area of a single unit cell:

$$p = \frac{J}{J_{\text{PS}}} = \frac{A_{\text{pore}}}{A_{\text{unit cell}}} \quad (1.7)$$

For a square and a hexagonal pore arrangement the porosity is then given as:²

$$\text{square : } p = \frac{\pi r^2}{a^2} \quad \text{hexagonal : } p = \frac{3\pi r^2}{\frac{3}{2}a^2\sqrt{3}} = \frac{2}{\sqrt{3}} \frac{\pi r^2}{a^2} \quad (1.8)$$

Surfactant

A surfactant is necessary to avoid hydrogen bubbles sticking to the surface. Furthermore, it has also some influence on the pore formation. In the experiments carried out two different surfactants were used: SDS (from SIGMA) and NCW-1002 (from WAKO). SDS is sodium dodecyl sulfate ($\text{C}_{12}\text{H}_{25}\text{O}_4\text{SNa}$), a common anionic surfactant normally used in household products as well as chemical industry. NCW-1002 is a trade name and it is an aqueous solution with ten percent polyoxyalkylene alkyl ether and of nonionic nature. In former work it was shown that SDS is well suited for etching of straight pores while NCW is used for diameter-modulated pores. A more detailed investigation of different surfactants can be found in Ref. [27].

HF Consumption

In the divalent as well as in the tetravalent dissolution of silicon (cf. Eqs. 1.2 to 1.4), six fluor atoms per dissolved silicon atom are required and thus HF concentration diminishes steadily. The concentration loss can be estimated: For a typical sample with straight pores of a diameter half the lattice constant (porosity of 20% to 25%), an etched area of 3.14 cm^2 , and a reservoir of 900 ml HF (5 wt%) the concentration drops by 0.1 wt% per $1000 \mu\text{m}$ etching depth. So the concentration loss during the etching of several tens to a few hundred micrometers can be neglected. To ensure reproducible etching conditions, however, a new HF solution should be prepared after $1000 \mu\text{m}$ have been etched. Another possibility would be to adjust the value of J_{PS} by this rough approximation or by measuring the charges in the electric circuit.

The discussion of this issue has some importance because based on HF concentration and temperature the value J_{PS} is calculated and used as an external parameter in the etching process. A lower than expected HF concentration means a smaller value of J_{PS} (Eq. 1.5) and thus a higher porosity (Eq. 1.6). The result would be pores with an increased diameter but decreased length compared to the expected morphology. The reverse is true for a higher than expected HF con-

²Assuming squared pores instead of circular ones changes A_{pore} to $4r^2$ instead of πr^2 .

centration. Especially for modulated structures, where stable and unstable pore etching processes take turns, this can easily lead to a complete failure. Furthermore, the optimization of the pore shape is not reproducible when not carried out for an exactly determined concentration.

Current Burst Model

The model presented here is sufficient to describe the etching process and the obtained results. Nevertheless, this continuum-like theory is based on macroscopical findings. A detailed description on an intrinsic time and length scale is given by the current burst model [21, 28].

In the SCR model it is assumed that the chemical reaction processes are homogeneously, i.e. the current density $j = j(x, y, t)$ is macroscopically defined and remains more or less constant in time and space. However, based on the different chemical reactions (Eqs. 1.2 to 1.4) and the experimentally observed dissolution valence of about 2.6 [20] to 2.7 [21] it can be concluded that locally – on a nanometer scale – different processes take place successively. A sequence of events (e.g. direct dissolution, oxidation, oxide dissolution, surface passivation) is thereby called a current burst. It has a certain probability to occur and is dependent on the surface state as well as on surrounding events in space (x, y) and time (t) . A detailed presentation of this model is beyond the scope of this work but it is required for a more profound understanding of pore formation in silicon.

Stability

Concerning the stability of the etching process several points are relevant. First, the etching speed is affected by the electrolyte temperature. To avoid inhomogeneities during etching the temperature has to be kept constant within 0.1 K. Another important point is the fact that during the pore etching HF-molecules are consumed and hydrogen is produced. To avoid hydrogen bubbles to stick at the surface the electrolyte needs to be stirred or pumped. In addition, some surfactant should be added as mentioned earlier.

The consumption of HF-molecules can be neglected as long as the volume of the electrolyte is large compared to the dissolved volume of silicon. However, things are different at the micrometer scale inside the pores. While a pore is growing, the exchange of reactants with the HF-basin at the front side of the sample becomes more and more affected by diffusion processes. A concentration gradient establishes between the pore bottom and the opening of the pore at the sample surface. Consequently, with a lower concentration the critical current density J_{PS} diminishes and the etching speed slows down. According to Eq. 1.6, a decreasing J_{PS} results in an increasing porosity p if the illumination intensity and thus the current density J is kept constant. The pores grow larger in diameter and finally – for $J_{PS} < J$ – electropolishing sets in. To avoid this situation a correction parameter is introduced for the illumination intensity in dependence on the pore depth. In that way, a uniform pore pattern with aspect ratios of several hundreds to one can be obtained.

After defining the starting conditions with a pattern of pore nucleation sites, the etching process itself is self-stabilizing. The porosity is controlled by the current density J over the entire etched surface. Hence, there is no direct control mechanism for an individual pore. The self-stabilizing effect is based on the fact that the HF concentration determines the etching speed

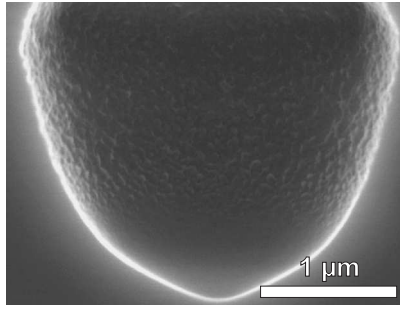


Figure 1.5: SEM micrograph of a pore bottom. While the tip of the pore has a smooth electropolished surface the walls are covered with a rough layer of microporous silicon (picture taken from Ref. [26]).

given by J_{PS} . In a situation where one pore is somewhat ahead of the surrounding ones, this pore collects more charge carriers because of its enlarged SCR. However, the excess of consumed charge carriers decreases the concentration of the HF in this pore. As a consequence, the etching speed is reduced and the offset to neighboring pores is compensated. Analogous argument holds for pores staying behind the surrounding ones. Because of this feedback interaction the pore depth is the same for all pores (Fig. 1.4b).

Surface Roughness

The adjustment of the effective current density controlled by the back side illumination is done over the whole etched area. However, the local current density at the tip of the pore is always J_{PS} and decreases towards the pore walls. Consequently, the bottom of the pore is electropolished and a very smooth surface is obtained (Fig. 1.5). In contrast, the pore walls exhibit a layer of microporous silicon with a certain roughness. The reason for this layer can be found in a kind of post etching process. While at the outermost pore tip electropolishing occurs the current drops gradually along the pore wall and therefore the already etched pore walls are being post-etched. Both, the divalent and the tetravalent dissolution of silicon as shown in Eqs. 1.2 to 1.4 take place simultaneously. This is experimentally confirmed by the fact that the number of charge carriers required for the dissolution of one silicon atom is about 2.7. Additionally, there is always a certain amount of dark currents, e.g. charge carriers generated by tunneling processes, thermal excitation, or avalanche breakdown. The morphology of the microporous layer depends on the applied voltage and illumination intensity as well as on the mixture of the electrolyte, especially on the added surfactants.

Limits

Naturally, the question arises what are the limits of this process? It appears in Eq. 1.1 that any width W_{SCR} can be obtained just by the proper doping of the material. In lowly doped material, large interpore distances and pore diameters can be realized, e.g. etching of pore diameters up to 100 μm were reported [29]. For small interpore distances, highly doped substrates are required. The pore formation process then is limited by electrical breakdown because the critical voltage at which charge carriers are generated by electrical breakdown approaches only a few volts. It has to be considered that the local electric field strength at the pore bottom is increased due to the curvature of the pore tip. In this case the field strength is significantly higher than that for a planar interface. This effect is most pronounced in the small interpore distance region. The lower

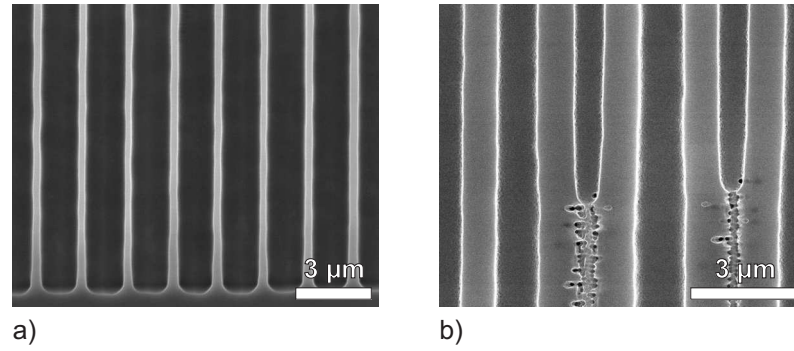


Figure 1.6: Cross section SEM of a) pores with a diameter close to the interpore distance and b) dying pores when the diameter is not big enough. The amount of holes generated by electrical breakdown is increased leading to corroded pore walls and mesopores growing perpendicular to the main pore.

limit for homogeneous pore formation as described by the presented model is reached at a lattice constant of about 500 nm.

The same arguments are true for the pore diameter. With a fixed doping density and a given lattice constant pores with diameters close to the interpore distance are possible (Fig. 1.6a). The limit for diameters that are small compared to the interpore distance is determined by the local breakdown voltage. If the pores are too small in diameter the resulting small radius of curvature will locally boost the electrical field strength and unintentional charge carrier generation can no longer be prevented. Furthermore, charge carriers can bypass the region of the pore tip and post-etch the pore walls. Therefore, small pores with diameters of only a few hundred nanometers or even less can be grown, but the pore walls show a ragged and non-uniform surface (Fig. 1.6b). Mesopores grow resulting in sponge-like structures and the continuum model discussed so far is no longer valid any more.

A further limiting factor comes from the lifetime of the minority charge carriers. In general, their lifetime is limited by recombination processes. Radiative recombination is only of minor impact because of the indirect band gap of silicon. Recombination at impurities or lattice defects is minimized by the float zone process for wafer fabrication. This kind of recombination mechanism is called Shockley-Read-Hall recombination. In contrast, intrinsic Auger recombination cannot be prevented. With higher doping density – as necessary for smaller lattice constants – the probability of energy transfer to a third carrier increases. Thus, the minority carrier lifetime is reduced and hence also their diffusion length which reduces the efficiencies of the charge carrier generation by the back side illumination process.

Pores with Modulated Diameter

The presented photo-assisted electrochemical etching process is not only limited to the formation of straight pores. As mentioned in Eq. 1.6 the porosity is given by the back side illumination intensity. This dependence can be applied to alter the pore diameter during the etching. Thus, sinusoidally diameter-modulated pores are obtained [30]. The formation of pores with sharp kinks, however, requires an additional adaption of the SCR via the applied potential. As shown by Matthias et al. in Ref. [31], an increase of the voltage in the beginning of a new modulation

can be used to form pores with very small diameters. During this step, a certain amount of charge carriers are generated by breakdown. After a tiny pore has formed, this unstable regime is left by decreasing the voltage again and the pore is widened in its diameter by an increased back side illumination intensity. Since the formation of strongly diameter-modulated pore is mandatory for the fabrication of 3D photonic crystals, the underlying mechanisms will be discussed in more detail in chapters three and four.

1.3 Post Treatment of Macroporous Silicon

After the etching process in aqueous HF the silicon surface is hydrogen-terminated. In ambient atmosphere this surface coverage is not stable and after some hours an oxide layer forms. The thickness of this layer is reported to be between ten and thirty angstrom and remains stable. Due to the humidity the surface bonds are saturated with hydroxyl molecules. The hydrogen-terminated silicon surface is hydrophobic. In contrast, an oxidized silicon surface and also a surface terminated with Si–OH (silanol) groups is hydrophilic.

1.3.1 Oxidation

The ease of forming an oxide layer is one of the most valuable properties of silicon. Thermal oxidation of silicon is typically performed at temperatures between 800°C and 1200°C, either in a dry or wet atmosphere. In a dry oxidation process the environment contains only oxygen. The grown films are very uniform and denser than films grown under wet conditions (i.e. in the presence of water). The growth rate of a dry oxide, however, is much slower than that for wet oxidation.

The growth rates given in literature are mostly obtained for planar surfaces. The oxidation of curved surfaces on the other hand is – dependent on the diameter of the pores – retarded compared to flat interface conditions [32]. The reason is the strain induced during the growth of the oxide layer. The volume of silicon dioxide is 2.25 times larger than that of bulk silicon. Inside a pore the grown silicon dioxide layer cannot relax in the same way as on a planar surface. This additional induced strain significantly lowers the diffusion of oxygen through the silicon dioxide layer towards the silicon interface where the oxide growth takes place. Hence, also the growth rate is reduced and the oxidation process – especially for thick silicon oxide layers of several ten to hundred nanometers – is retarded.

While for bulk silicon the maximum oxide thickness is limited to a few micrometers, macroporous silicon structures can be completely oxidized [33]. Due to the higher volume fraction of silicon oxide the pore diameters are reduced and the sample gets bent.

1.3.2 Isotropic Etching

The thermal oxidation of silicon yields uniform oxide layers with a thickness determined by the oxidation conditions (atmosphere, temperature, time). Oxide removal is performed in HF-containing acids such as aqueous HF or NH_4F . Since this process is selective between silicon and silicon dioxide it can be used for isotropic etching of the porous structures. The advantage of this process compared to an isotropic etching in, e.g., a mixture of HF/ HNO_3 is the precise thickness

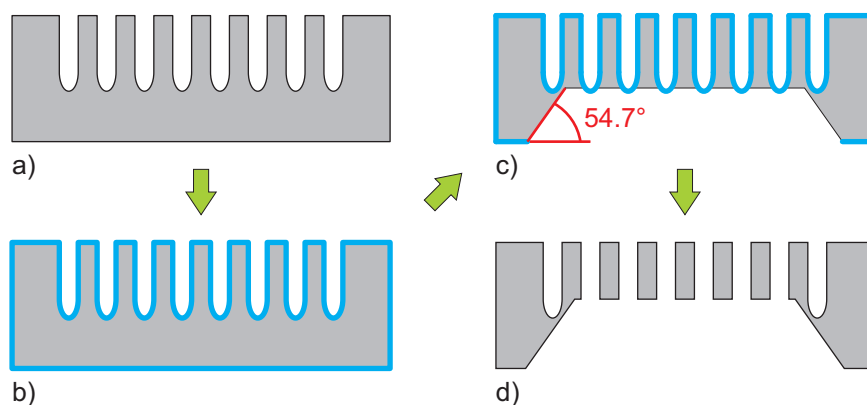


Figure 1.7: Schematic representation of membrane fabrication: The etched macroporous silicon (a) is oxidized (b). After the oxide is removed from the back side the silicon is etched in KOH until the pore bottoms are reached (c). The angle between the (100) oriented surface and the remaining (111) pore wall is 54.7° , defined by crystallography. The silicon dioxide can be removed with an HF-dip and a porous membrane is obtained (d).

control: The amount of silicon removed by this procedure is determined by the thickness of the grown oxide layer. This allows for tuning the pore diameter after the etching.

Although this process seems to be straightforward, some restrictions have to be kept in mind. For thin oxide layers (short oxidation times) the oxide growth speed is very high. Hence, statistical fluctuations during the growth can have undesired effects such as large deviations in the oxide layer thickness. In the case of thick oxide layers the dominating factor is the induced stress. Therefore, the possibility of damaging the macroporous structure has to be taken into account. An oxide layer thickness of 50 to 100 nm is an optimum value avoiding both, inhomogeneity and cracking. If thicker layers have to be removed it is recommended to split this procedure into several sequential oxidation and oxide removal steps.

1.3.3 Anisotropic Etching

In alkaline etchants silicon is etched anisotropically under evolution of hydrogen (two H_2 molecules per dissolved Si-atom). During the etching the surface is covered with Si-OH and Si-H groups. The ratio depends on pH-value and temperature. In this work KOH was used at a concentration of 25 wt%. The {100} planes and the {110} planes are preferentially etched and the etch rate is one to two orders of magnitude larger than that for the {111} planes [34]. The reason for the anisotropic etching in KOH is analogously to the anisotropic divalent dissolution of silicon in HF (cf. section Electrochemistry on page 7). Instead of the fluor atoms the OH-groups are now responsible for the weakening of the silicon backbonds due to polarizing effects.

Aside from an anisotropic pore etching the alkaline etching is used to fabricate membranes, i.e. porous structures with both ends of the pores opened. This means that the remaining silicon from the back side up to the pore bottoms has to be removed. Therefore, a further property of KOH is considered: The etch ratio between silicon and silicon oxide can reach a factor of several thousands and thus a silicon dioxide layer can be used as an etch stop. Based on this property the porous structure is first oxidized for two hours at 900°C . Afterwards, the oxide is removed from the back side in NH_4F and the silicon is etched in KOH. When the pore bottoms are reached, the

silicon oxide protects the porous structure from the KOH for a couple of minutes which gives enough time to stop the process. Subsequently, the oxide is etched away in an HF-containing solution and a macroporous membrane is obtained (Fig. 1.7).

1.4 Alternative Methods to Fabricate Ordered Porous Structures

1.4.1 Top-down

Aside from the macroporous silicon material system there are further approaches to fabricate ordered porous structures. At the lower end of the reachable pore diameters in macroporous silicon follows the anodization of aluminum (Fig. 1.8a). Although a prestructuring of the aluminum chips can be done, e.g. by nanoimprint lithography [35, 36], the pore growth is self-ordered in a hexagonal arrangement [37]. Using different acids (e.g. sulphuric, oxalic, or phosphoric acid) and voltages (25 – 200 V) the obtainable interpore distances can be varied between 50 nm and 500 nm [38]. Thereby the voltage controls the interpore distance and the pH-value of the acid is responsible for the pore diameter.

This anodization process is not limited to the anodization of aluminum. The anodic oxidation of several other metals was reported, e.g. titanium [39], zirconium [40], niobium [41], hafnium [42], tungsten [43], zinc [44], tin [45], tantalum [46], and others. However, while two-dimensional (2D) structures can be realized very well with the anodization of metals the ability to modulate the pore diameter and therefore to obtain real three-dimensional (3D) structures is still limited to minor diameter modulations.

Especially for the preparation of 2D structures in a number of materials reactive-ion etching (RIE) is used. Dependent on the material that has to be etched a proper etching plasma is generated. The etching process itself consists of two different mechanisms, the chemical reaction of the plasma radicals with the material and a physical etching due to ion bombardment. Necessarily, the material under consideration has to have a mask that can be written with electron beam or optical lithography.

Beside silicon, other semiconductors were electrochemically etched, too. In [47] the pore formation in germanium is shown for a couple of different parameters like doping type and density, crystal orientation, and etching solution. Furthermore, there are efforts to etch pores in III-V semiconductors such as GaAs, GaP, and InP. In references [48] and [49] the morphology of the pore formation is considered in detail and is compared with the findings from etching porous silicon.

1.4.2 Bottom-up

3D structures can be also manufactured in bottom-up processes. A typical example is the self-assembly of spherical particles to large-scale structures (Fig. 1.8b). Therefore, equally shaped particles are dispersed in a liquid and during evaporation they assemble themselves in a closely-packed face centered cubic lattice, the opal. The drawbacks of this method are the shrinkage of the particles during the drying process, local defects due to missing particles and a lack of long-range order due to defects like grain boundaries. Nevertheless, remoulding of this opal structure gives nice photonic crystals, the inverted opals (cf. section 3.4).

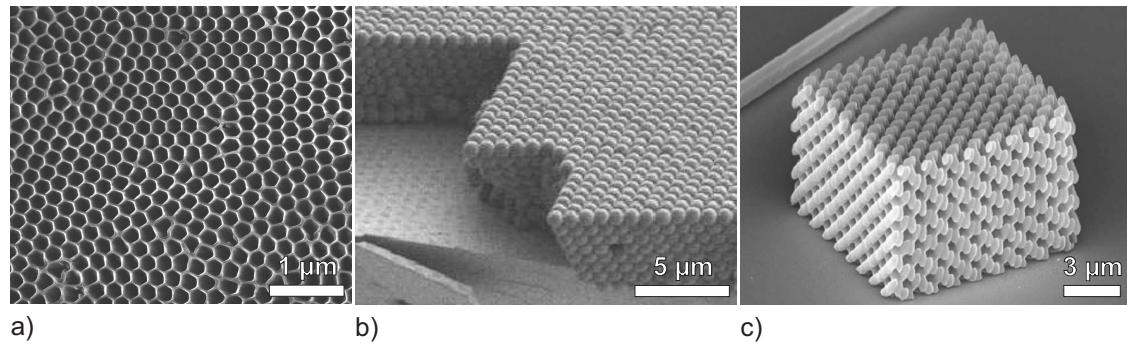


Figure 1.8: a) Self-ordered aluminum oxide anodized in phosphoric acid (H_3PO_4). b) An example for self-assembly of silica spheres with 855 nm diameter on a silicon wafer (picture taken from Ref. [50]). c) A so-called slanted-pore photonic crystal made by direct laser writing in SU-8 photoresist (reproduced from Ref. [51]).

A versatile approach of transferring a model to an SU-8 block is proposed in Ref. [52]. SU-8 is a photoresist capable of sub-100 nm resolution. The method is called holographic lithography because it uses the interference of several (four in this case) non-coplanar laser beams (wavelength $\lambda = 355\text{ nm}$) to irradiate a $30\text{ }\mu\text{m}$ thick layer of SU-8. The interference pattern gives a localized intensity distribution inside the photoresist. The parts of the photoresist that are highly exposed are rendered insoluble whereas the unexposed parts can be chemically dissolved after baking the structure. The interference pattern can be altered with a considerable degree of freedom and because of its translational symmetry it is reproduced in all three spatial dimensions.

In addition to this process or even as a stand-alone method direct laser writing by multiphoton polymerization was developed [53, 54, 51]. Similar to the holographic lithography a photoresist is illuminated with different intensities and after exposure the unexposed areas can be dissolved (Fig. 1.8c). In contrast to the parallel holographic lithography process direct laser writing is a serial writing process. A laser beam with an energy below the photopolymerization threshold of the resist is used. By focusing the beam to a narrow spot the light intensity may exceed the threshold and photopolymerization takes place. Both methods, holographic lithography and direct laser writing are able to produce arbitrarily shaped 3D structures. However, one challenge in this process is the compensation of shrinkage effects [55]. Further processing steps have to be performed to transfer the form into a material different from the photoresist. This is necessary, e.g., for photonic crystal applications where a high dielectric contrast is required. Only recently it was shown, that this process can also be used to directly photopolymerize a TiO_2 resist and thus 3D structures can be written directly into a material with a high refractive index as demanded in photonic crystal applications [56].

Chapter 2

Macroporous Silicon in Materials Science

Within the scope of this work the macroporous silicon material system was used for a number of applications in the field of materials science. Therefore, different techniques and procedures were used to achieve the required pore geometry or surface condition. However, since the main part of this work is dedicated to the fabrication and utilization of macroporous silicon as a photonic device, this chapter should give a condensed survey of the most important findings.

2.1 Various Shapes of Macroporous Silicon

Macroporous silicon with its well defined pore shape is often used as a template material. Samples with straight pores and different aspect ratios were prepared and applied as a template to form polymers filled inside the pores [57, 58] or as a microreactor array for oxidation experiments [59].

For the membrane fabrication method presented in section 1.3.3 a treatment in KOH is required to open the pore bottoms of the etched samples from the back side. However, the macropo-

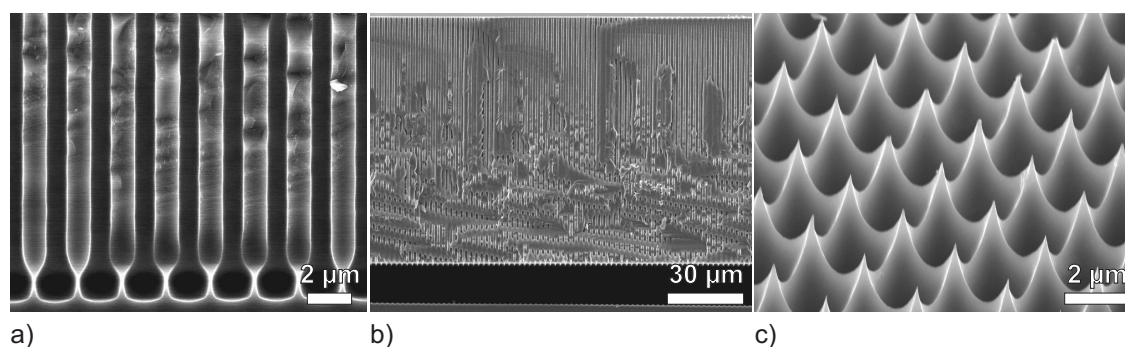


Figure 2.1: SEM micrographs of macroporous silicon with 2 μm interpore distance in a square pore arrangement. a) Cross sectional view of straight pores with increased pore diameter at the pore bottom. b) Released layer of straight pores. The gap between the porous layer and the remaining bulk silicon at the bottom edge of the picture indicates the successful release of the porous membrane. c) Bird's eye view of the remaining bulk silicon surface after the macroporous layer has been released. The sharp silicon spikes can be used for instance as an imprint stamp.

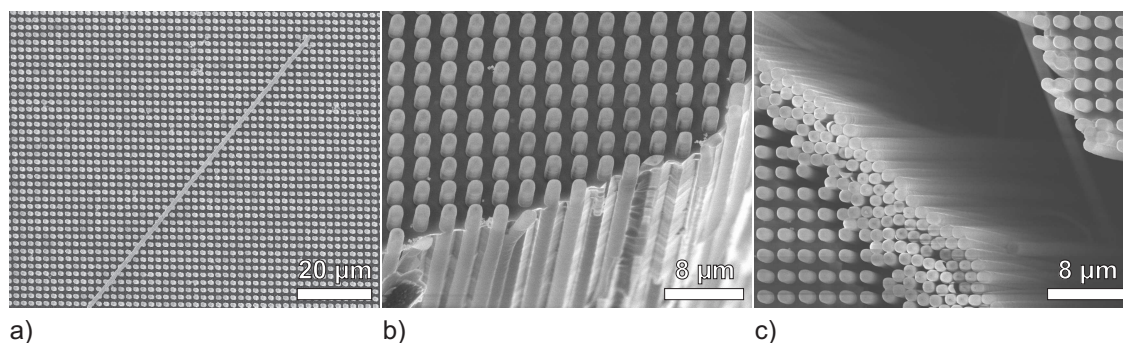


Figure 2.2: SEM micrographs of macroporous silicon with $2\text{ }\mu\text{m}$ inter pore distance in a square pore arrangement. a) An array of oxidized macroporous silicon tubes (bright spots) after partly removing the silicon from the back side with KOH. On top of this array a silicon dioxide tube is shown. b) Bird's eye view onto a bottom edge of this sample. The thickness of the tube's pore walls is about 100 nm and depends on the oxidation parameters time, temperature, and atmosphere. c) Fully released silicon dioxide microtubes after several hours of etching in KOH. The length of these tubes is $200\text{ }\mu\text{m}$.

orous layer can be already released from the bulk silicon during the etching process. Therefore, the back side illumination intensity is strongly increased by a factor of 2.5 over a length of $2\text{ }\mu\text{m}$ at the end of the etching process (Fig. 2.1a). Now, neighboring pores are almost touching each other and the whole macroporous layer can be easily separated by a mechanical force from the substrate or by an oxidation step followed by an HF-dip (Fig. 2.1b). Beside the released free-standing macroporous silicon membrane the remaining bulk silicon is of interest, too. As can be seen in Fig. 2.1c the surface forms sharp spikes arranged in a regular lattice given by the initial lattice geometry. Since silicon is a very hard material, this micro 'fakir pillow' could be used as a micrometer sized structuring tool, e.g. as a stamp for imprint lithography.

To a certain extent tubes and cylinders are the inversion of pores. The easiest way for tube preparation can be realized by partial oxidation of a straight pore sample and a subsequent KOH etching process. Depending on the macroporous silicon treatment prior to the oxidation, microtubes with closed pore bottom (like a test tube) or open pore bottom (like a straw) can be realized. A back side view of closed SiO_2 tubes partly released from the silicon is shown in Fig. 2.2a. In order to get a high etch contrast between silicon and silicon dioxide low concentrated KOH (2 wt%) at room temperature was used. The etch ratio between the silicon $\langle 100 \rangle$ direction and silicon dioxide exceeds a factor of 10000 : 1. This ensures the complete release of the hollow silicon dioxide tubes from the silicon, even for tubes with high aspect ratios and thin pore walls (Figs. 2.2b and c). The length of the tubes is given by the length of the etched pores. The inner and outer diameter as well as the wall thickness are dependent on each other and determined by the initial pore diameter and the thickness of the grown silicon dioxide layer. A macroporous silicon pore diameter of $1\text{ }\mu\text{m}$ and a grown silicon dioxide layer with 100 nm thickness would result in an outer tube diameter of $1.1\text{ }\mu\text{m}$ ¹.

¹The atomic volume of silicon is $20\text{ }\text{\AA}^3$ and the molecular volume of silicon dioxide is $45\text{ }\text{\AA}^3$. Therefore, 44.4 nm silicon are consumed to grow a 100 nm thick silicon dioxide layer.

2.2 Surface Treatment and Replication with Atomic Layer Deposition

If silicon is used as a porous material with the feature of a large surface-to-volume ratio, the surface termination is an important property for applications, e.g. catalytic processes or gas separation due to adsorption of molecules at the surface. Furthermore, macroporous silicon is often used as a template material, because of the variably tunable shapes that are possible with this material system. In order to extend the advantages of macroporous silicon to other materials the treatment of macroporous silicon with atomic layer deposition (ALD) is explored in this section.

ALD belongs to the gas phase chemical processes and is an improvement of the chemical vapor deposition (CVD) [60]. Usually, two different chemicals (herein after referred to as precursors) are used in an alternating sequence. In contrast to CVD the chemical reaction in the ALD process is self-limiting. Starting from a given surface termination the first precursor is exposed to the material. Because of the precursor design only one molecule layer can be bound to the surface. The second precursor modifies the surface bonds in a way suitable for a repeated exposure with the first precursor and the next cycle can start. Thus, the layer thickness on a target material can be precisely controlled by the number of cycles.

Due to the self-limiting reaction in the ALD process very conformal and precisely thickness-controlled films can be grown over large areas. Typical film thicknesses are in the range of a fraction of one nanometer up to several hundred nanometers. The range of materials that can be used in ALD depends on the possibility to synthesize adequate precursors. A review of ALD is given in Ref. [61] where the deposition of pure elements as well as compounds such as nitrides, sulfides, or metal oxides is reported.

Within the scope of this work three different metal oxides were successfully deposited on macroporous silicon samples: Zinc oxide (ZnO), hafnium dioxide (HfO₂), and titanium dioxide

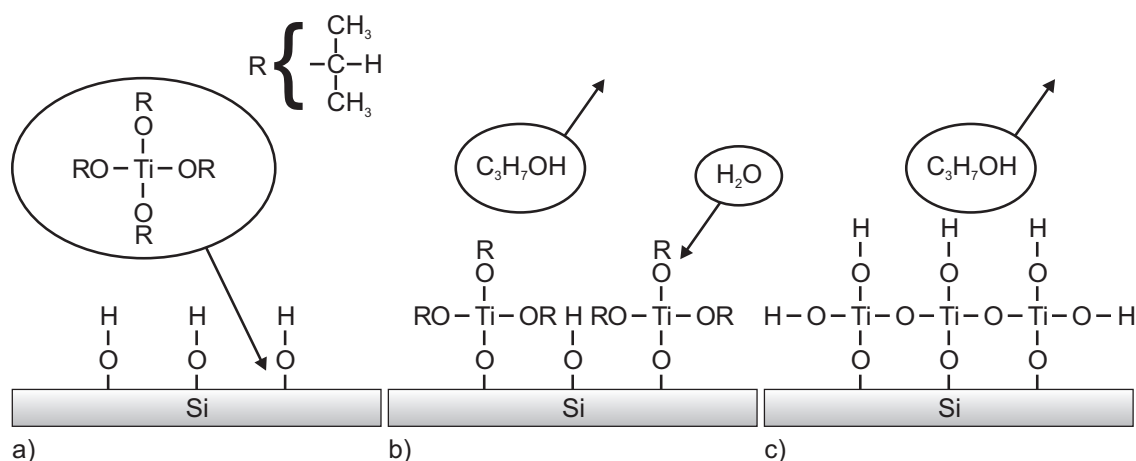


Figure 2.3: Scheme of the ALD process for the deposition of TiO₂ onto a silicon surface. a) The silicon surface is hydroxyl-terminated and exposed to titanium isopropoxide with R the rest group (C₃H₇). b) Under abstraction of isopropanol the titanium isopropoxide molecule bonds to the silicon surface. c) H₂O is the second precursor and hydrolyzes the remaining alcoholate. One ALD cycle is complete. The surface is covered by a layer of TiO₂ and the process can start again with the first precursor.

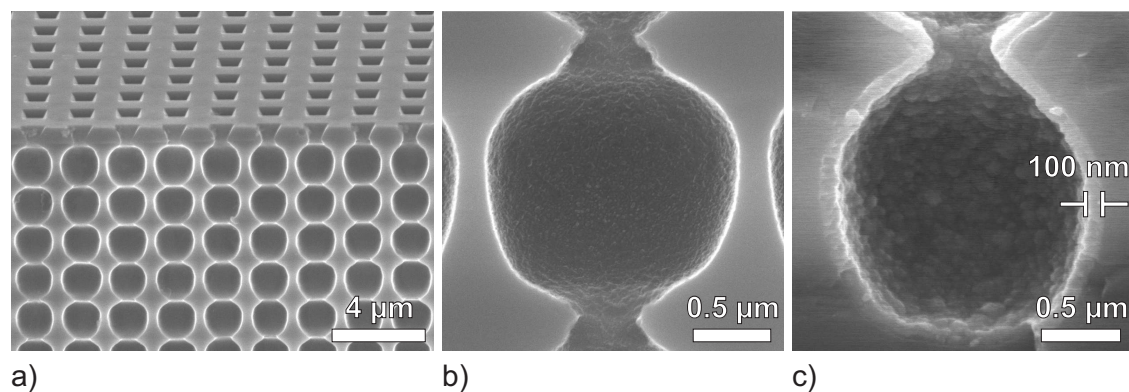


Figure 2.4: Cross section SEM micrographs of 3D modulated macroporous silicon. a) Bird's eye view of an etched sample with $2\text{ }\mu\text{m}$ interpore distance and 17 modulations ($30\text{ }\mu\text{m}$ depth). b) A single modulated pore with a minimum pore diameter of $0.4\text{ }\mu\text{m}$ and maximum pore diameter of $1.6\text{ }\mu\text{m}$. c) After deposition of 1000 cycles of TiO_2 the pore walls are covered with an approximately 100 nm thick layer of TiO_2 .

(TiO_2). ZnO is a semiconductor with a direct band gap of 3.4 eV used in laser diodes and light emitting diodes, or as transparent electrode material. HfO_2 is one of the materials that will be most likely used in the future to replace silicon oxide as gate insulator in field effect transistors. As a high- k dielectric material HfO_2 is better suited for that purpose since the ongoing down scale efforts require a decreased oxide layer thickness, too. Finally, TiO_2 was chosen due to its importance as a photocatalytic and biodegradable material [62, 63]. For the ALD process a commercial reactor (Savannah100, Cambridge NanoTech Inc.) was used. It consists of a sample chamber which is evacuated during the deposition process and several inlets for different precursors. The exposure time is controlled via magnetic valves.

As an example, the deposition of TiO_2 on a macroporous silicon template is looked at in more detail. Following the work of [64] titanium isopropoxide ($\text{Ti}(\text{OCH}(\text{CH}_3)_2)_4$) and H_2O were used as precursors. The titanium isopropoxide precursor replaces the hydroxyl group remaining on the surface of the macroporous silicon under abstraction of isopropanol ($\text{C}_3\text{H}_7\text{OH}$, Fig. 2.3a). Subsequently, the remaining alcoholate is hydrolyzed with H_2O (Fig. 2.3b). After complete hydrolysis, the surface is hydroxyl-terminated again, allowing for repeated reaction (Fig. 2.3c). Every precursor pulse was 90 s long and between every pulse the chamber was purged to remove excess material and reaction by-products. The reactor temperature was 150°C .

A 3D modulated macroporous silicon sample (Fig. 2.4a and b) is used for the procedure described above. After 1000 cycles a 100 nm thick layer of TiO_2 was deposited (Fig. 2.4c). In contrast to the deposition of films on flat surfaces, the reactants had to diffuse into the porous structure and therefore the exposure time had to be adapted. A sufficiently long exposure time ensures homogeneous growth over the whole pore depth due to homogeneous distribution across all accessible surfaces. Although on the surface the titanium dioxide agglomerates into a grain structure the thickness of the film is highly conformal within the pores. In particular, no difference in thickness could be measured for the deposited layer of the first and the last pore modulation. This means that the precursor exposure times were sufficient to ensure a uniform deposition of material along the pore wall and thus indicates a successful growth within the self-terminating ALD reaction regime.

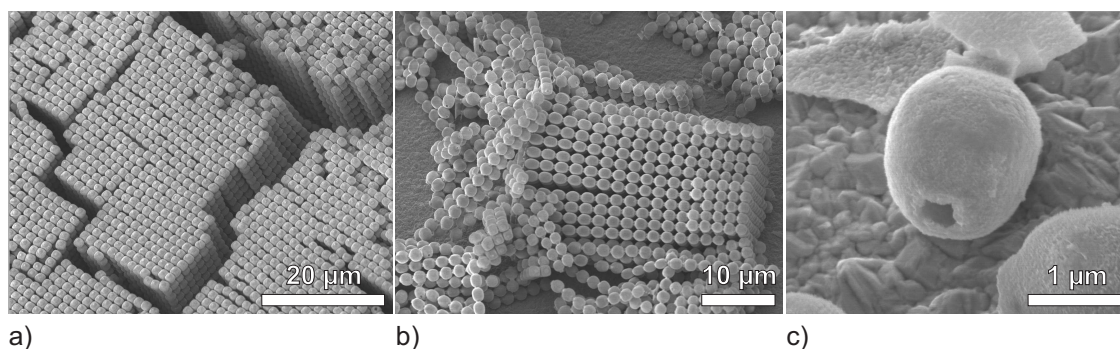


Figure 2.5: An array of chains of hollow TiO_2 micropearls is obtained after the silicon was removed. a) Bottom view. The closed and TiO_2 -covered pore bottoms are visible b) Side view. The pore modulation is replicated in modulated TiO_2 chains. c) One single sphere from such a chain can be separated by applying mechanical force, e.g. via ultrasonic exposure.

The reason for the grain structure is explained as follows: Presumably, the growth of a smooth layer is hindered due to an initial island growth caused by the surface roughness of the macroporous silicon. The surface roughness of the macroporous silicon and thus also the size of the grains can be significantly reduced, e.g. by a short oxidation of the silicon structure followed by a dip in 12.5 wt% N_4HF prior to the ALD. Additionally, at those temperatures (150°C) polycrystalline anatase films of TiO_2 form. Adjusting the temperature in the ALD reactor to higher or lower process temperatures would result in different crystal phases of TiO_2 or amorphous TiO_2 , respectively. For amorphous TiO_2 smoother layers are obtained.

While thin coatings are well suited to change the surface properties, thicker coatings can be used to replicate the entire macroporous silicon structure into a new material. In the presented case of TiO_2 the silicon host material can be removed in a KOH solution without affecting the TiO_2 . The obtained structures exhibit an exact copy of the modulated macroporous silicon pores (Fig. 2.5a and b). These chains of connected hollow titanium dioxide spheres are very uniform in size and shape. The volume of one single sphere (Fig. 2.5c) is two femtoliter and billions of equally shaped copies can be obtained on a whole wafer. Just to give an example such single spheres could be used as carriers for drug delivery with a clearly defined volume.

Beside the possibility to form micrometer to sub-micrometer sized microstructures and to replicate them with the ALD process presented above, it is also possible to achieve highly porous network structures. These can be of interest for enhanced catalytic reactions or cell culturing applications, especially in 3D [65]. For this purpose it is necessary to establish a connection between the pores prior to the ALD process. Using the same modulated template as presented in Fig. 2.4a a connection in the lateral direction was achieved using the isotropic etching procedure described in section 1.3.2. As a result, the pore is isotropically widened until neighboring pores get connected to each other (Fig. 2.6a). The subsequent treatment with the described ALD process and subsequent silicon dissolution in KOH results in highly porous network structures (Figs. 2.6b and c). The shape of the original silicon scaffold structure is perfectly reproduced in TiO_2 with only a few ten nanometers wall thickness. Likewise, the surface area was increased by a factor of two because now both sides of the TiO_2 wall can be used for exposure or as reactant area. The stability of this structure can be increased by depositing a thicker layer of TiO_2 and the handling

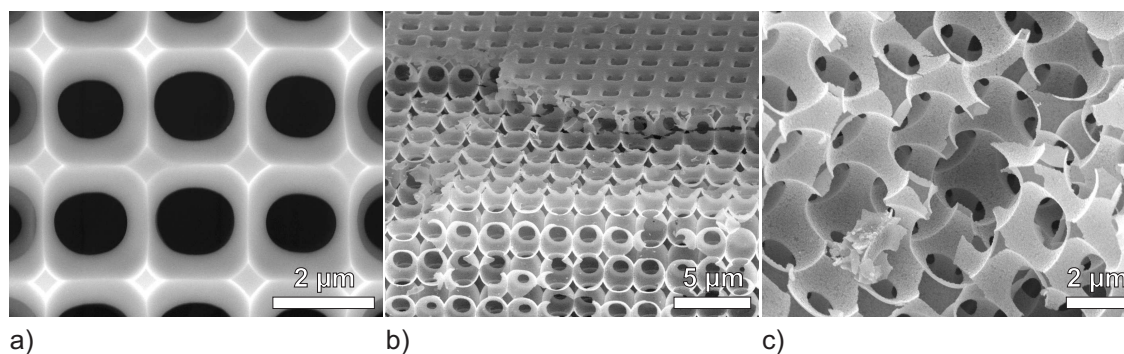


Figure 2.6: SEM micrographs of a porous network structure. a) Cross section of the silicon pores after the widening procedure. The gray parts are the remaining silicon with sharp edges (bright lines) and connected to each other. In the dark areas the silicon is completely removed and therefore an opening to the neighboring pore is established. After the replication of the silicon structure highly porous TiO_2 network structures are obtained: b) Bird's eye view where part of the top layer is removed. c) Closer look into the porous TiO_2 scaffold structure.

is more convenient if only part of the silicon is dissolved so that the porous scaffold structures is still connected to a solid base.

To summarize this chapter, the macroporous silicon material system offers a lot of freedom in the design of ordered porous templates with a well defined shape. Especially the fabrication of 3D modulated structures and the scalability of this process should be emphasized once again. Additionally, a new method based on ALD was introduced to extend the versatility of the pore morphologies into a number of other materials. The presented atomic layer deposition process offers several advantages for this purpose: First, because of its self-terminating deposition process it is capable to cover porous materials with high aspect ratios where material diffusion has to be taken into account and a homogeneous coating is required. Second, the ALD process is scalable as well and therefore this unique property of the macroporous silicon process is preserved. And third, by choosing proper precursors many materials can be used in the ALD going from nanometer thick surface coatings to a replication of the entire structure.

Chapter 3

Photonic Crystals

Macroporous silicon can be manufactured as a long-range ordered structure with a variety of different shapes. In addition, silicon is a dielectric material with a large dielectric constant of about twelve in the infrared region of light. These two points, the precise ordering and the large dielectric contrast to air favors the application of ordered macroporous silicon structures as photonic crystals. In this chapter the concept of photonic crystals will be introduced. It starts with a definition of the term photonic crystal and a short historical overview. The theory section will provide the necessary background for the theoretical description of photonic crystal properties and their interaction with electromagnetic waves.

3.1 Introduction

For the definition of the term photonic crystal an analogy to the known crystal lattices consisting of atoms is often used [66]. In general, a crystal is a periodic arrangement of a basic building block, the unit cell. In solid-state physics the unit cell of a crystal consists of atoms. In contrast, the unit cell of a photonic crystal is an arrangement of materials with different dielectric constants. This analogy can be also used to introduce the photonic band gap. In a solid-state crystal a periodic lattice potential $V(\vec{r})$ is formed by the atoms and affects the propagation of electrons. If this potential is strong enough an energy gap forms in which the propagation of electrons is forbidden. Such materials are known as semiconductors. In the case of photonic crystals the lattice potential is given by a periodic arrangement of dielectric material, i.e. by a periodic dielectric function $\epsilon(\vec{r})$. Once again – if the dielectric contrast is high enough – energy gaps form in which the propagation of photons is prohibited.

Photonic crystals are classified based on the dimension of their periodicity. A layer-by-layer structure of two different dielectric materials can be thought of as a one-dimensional photonic crystal. Accordingly, two- or three-dimensional photonic crystals are obtained if the material is periodically arranged in two and three dimensions, respectively (Fig. 3.1).¹

The development of photonic crystals started with two independent publications in 1987. Yablonovitch [68] suggested the possibility to inhibit the spontaneous emission of light. Driven by applications in the semiconductor industry that suppress electron-hole recombination he pro-

¹A somewhat stricter definition is given by Yablonovitch in [67], in which he restricts the term photonic crystal to be used only for materials with a ‘high index contrast and a 2D or 3D periodic structure’.

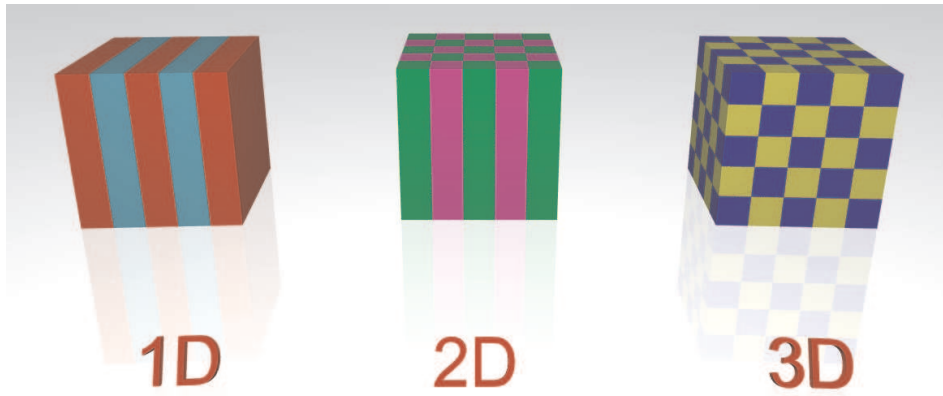


Figure 3.1: A photonic crystal represented schematically as a periodic arrangement of material with two different dielectric constants (symbolized by different colors) in one, two, and three dimensions.

posed a dielectric structure, periodically modulated in its refractive index in all spatial dimensions. Similar to the already known dielectric mirrors a periodicity of half the wavelength ($\lambda/2$) in any direction would lead to an electromagnetic band gap around the wavelength λ . Finally, if an electronic transition, e.g. from a laser, falls within the electromagnetic band gap, then any form of emission (spontaneous and stimulated) would be suppressed.

The second publication came from John [69]. His train of thought was in parallel with the strong localization of electrons in a disordered solid, the so-called Anderson localization [70]. He showed theoretically that in a disordered structure with a high dielectric contrast a strong localization of photons can occur.

In the following the stage was set for the first crystal structures to be proposed and fabricated with a complete photonic band gap in all directions of photon propagation. In 1990 Ho et al. proposed the diamond lattice to be most promising for a 3D crystal with a large band gap [72]. Based on their calculations they found also that there is no complete photonic band gap in structures with an fcc lattice, disproving experimental observations published shortly before by Yablonovitch et al. [73]. However, the group of Yablonovitch had already experience in the fabrication and measurement of modulated dielectric structures and so they published simultaneously the experimental verification of a photonic band gap in the diamond lattice [71]. In Fig. 3.2 the

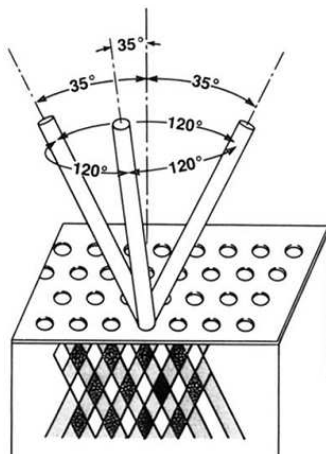


Figure 3.2: The Yablonovite. A block of material is covered with a mask of triangularly arranged holes. Through each hole three pores are drilled under an angle of 35.26° to the surface normal and spread out 120° on the azimuth (picture taken from Ref. [71]).

model of this first photonic band gap crystal is shown. It was fabricated by direct drilling of holes into a dielectric material and worked at frequencies in the microwave region.

3.2 Theory: Interaction of Light with Matter

Maxwell's equations, first formulated by James Clerk Maxwell in 1861, describe macroscopic phenomena such as the propagation of light in a photonic crystal. In SI units they are written as follows:

$$\nabla \cdot \vec{D}(\vec{r}, t) = \rho \quad (3.1)$$

$$\nabla \cdot \vec{B}(\vec{r}, t) = 0 \quad (3.2)$$

$$\nabla \times \vec{E}(\vec{r}, t) = -\frac{\partial}{\partial t} \vec{B}(\vec{r}, t) \quad (3.3)$$

$$\nabla \times \vec{H}(\vec{r}, t) = \frac{\partial}{\partial t} \vec{D}(\vec{r}, t) + \vec{j} \quad (3.4)$$

\vec{E} and \vec{H} represent the electric and magnetic field, respectively, of an electromagnetic wave. \vec{D} is the electric displacement field and \vec{B} the magnetic induction. The sources for the electric field are the free charges ρ (Eq. 3.1) while there is no source for the magnetic field (Eq. 3.2). Furthermore, changing magnetic fields contribute to electric fields (Eq. 3.3) and temporally varying electric fields as well as the current density \vec{j} aid to magnetic fields (Eq. 3.4).

For the present case of silicon as a linear and homogeneous dielectric material the relation between the vector fields \vec{E} and \vec{D} as well as \vec{H} and \vec{B} can be simplified (as long as the field strengths are small enough so that higher nonlinear terms can be neglected):

$$\vec{B}(\vec{r}, t) = \mu(\vec{r}) \mu_0 \vec{H}(\vec{r}, t) \quad (3.5)$$

$$\vec{D}(\vec{r}, t) = \epsilon(\vec{r}) \epsilon_0 \vec{E}(\vec{r}, t) \quad (3.6)$$

Thereby, $\mu(\vec{r})$ and $\epsilon(\vec{r})$ are the magnetic permeability and the dielectric permittivity of the material, respectively, whereas μ_0 and ϵ_0 are the according values of free space. It has to be mentioned that this is only true as long as the dielectric permittivity and the magnetic permeability are frequency independent. Silicon in the frequency range used in this work can be seen as a linear and homogeneous dielectric which justifies this assumption.

In the beginning the wave equation should be derived. For the interaction between electromagnetic field and silicon some simplifications can be made. The first assumption is the absence of free charges ρ and electric currents \vec{j} , i.e. $\rho \equiv 0$ and $\vec{j} \equiv 0$. Furthermore, in the case of a non-magnetic material like silicon the magnetic permeability $\mu(\vec{r})$ can be taken as one. The curl operator used on Eq. 3.4 with \vec{D} replaced by Eq. 3.6 gives

$$\nabla \times \left(\frac{1}{\epsilon(\vec{r})} \nabla \times \vec{H}(\vec{r}, t) \right) = \epsilon_0 \frac{\partial}{\partial t} \left(\nabla \times \vec{E}(\vec{r}, t) \right) \quad (3.7)$$

and the term $\nabla \times \vec{E}(\vec{r}, t)$ replaced by Eqs. 3.3 and 3.5 results in:

$$\nabla \times \left(\frac{1}{\varepsilon(\vec{r})} \nabla \times \vec{H}(\vec{r}, t) \right) = -\varepsilon_0 \mu_0 \frac{\partial^2}{\partial t^2} \vec{H}(\vec{r}, t) \quad (3.8)$$

For the electric and magnetic fields the ansatz of harmonic waves is chosen whereby the time dependency can be separated out:

$$\vec{H}(\vec{r}, t) = \vec{H}(\vec{r}) e^{-i\omega t} \quad (3.9)$$

$$\vec{E}(\vec{r}, t) = \vec{E}(\vec{r}) e^{-i\omega t} \quad (3.10)$$

The partial second derivative of the time in Eq. 3.8 gives an additional factor of $-\omega^2$ and the separation reduces Eq. 3.8 to be dependent on the spatial coordinates only:

$$\nabla \times \left(\frac{1}{\varepsilon(\vec{r})} \nabla \times \vec{H}(\vec{r}) \right) = \left(\frac{\omega}{c} \right)^2 \vec{H}(\vec{r}) \quad (3.11)$$

Thereby, the free space values ε_0 and μ_0 were replaced by the speed of light in vacuum c due to the relation $c = 1/\sqrt{\varepsilon_0 \mu_0}$.

The wave equation Eq. 3.11 is the so-called master equation (partial differential equation, also referred to as Helmholtz equation) that completely determines the magnetic field $\vec{H}(\vec{r})$. The description for the electric field $\vec{E}(\vec{r})$ can be derived from the magnetic field:

$$\vec{E}(\vec{r}) = \left(\frac{i}{\omega \varepsilon_0 \varepsilon(\vec{r})} \right) \nabla \times \vec{H}(\vec{r}) \quad (3.12)$$

3.3 Calculation of Photonic Band Structures

The Eigenvalue Problem

The differential equation Eq. 3.11 can be formulated as an eigenvalue problem with the hermitian operator Ξ :

$$\nabla \times \left(\frac{1}{\varepsilon(\vec{r})} \nabla \times \vec{H}(\vec{r}) \right) = \Xi \vec{H}(\vec{r}) = \left(\frac{\omega}{c} \right)^2 \vec{H}(\vec{r}) \quad (3.13)$$

Solving it for a given photonic crystal structure $\varepsilon(\vec{r})$ and a frequency ω will determine the allowable modes: The eigenvectors $\vec{H}(\vec{r})$ with their eigenvalues $(\omega/c)^2$. Since periodic dielectric structures are considered, the dielectric function $\varepsilon(\vec{r})$ is periodic in space, i.e. $\varepsilon(\vec{r}) = \varepsilon(\vec{r} + \vec{R})$ where \vec{R} is a lattice vector of the periodic photonic crystal lattice. Thus, Bloch's theorem can be applied. This means that the solution $\vec{H}(\vec{r})$ of Eq. 3.13 is periodic as well and can be expressed as:

$$\vec{H}(\vec{r}) = \vec{H}_{\vec{k}n}(\vec{r}) = \vec{u}_{\vec{k}n}(\vec{r}) e^{i\vec{k} \cdot \vec{r}} \quad (3.14)$$

where $\vec{H}(\vec{r})$ is characterized by a wave vector \vec{k} in the first Brillouin zone (BZ) and a band index n . The vectorial function $\vec{u}_{\vec{k}n}(\vec{r})$ is periodically in space:

$$\vec{u}_{\vec{k}n}(\vec{r} + \vec{R}) = \vec{u}_{\vec{k}n}(\vec{r}) \quad (3.15)$$

with \vec{R} a lattice vector in real space. Therefore, the magnetic field $\vec{H}(\vec{r})$ as well as the reciprocal of the dielectric function $1/\varepsilon(\vec{r})$ are periodic and can be expressed as Fourier series:

$$\frac{1}{\varepsilon(\vec{r})} = \sum_{\vec{G}} \kappa(\vec{G}) e^{i\vec{G}\cdot\vec{r}} \quad (3.16)$$

$$\vec{H}(\vec{r}) = \vec{H}_{\vec{k}\vec{n}}(\vec{r}) = \sum_{\vec{G}} \vec{H}_{\vec{k}\vec{n}}(\vec{G}) e^{i(\vec{k}+\vec{G})\cdot\vec{r}} \quad (3.17)$$

with \vec{G} a lattice vector of the reciprocal space. Substituting the corresponding terms in Eq. 3.13 with the last two Eqs. 3.16 and 3.17 gives an eigenvalue equation that is numerically solvable. The solutions are the eigen-angular frequencies $\omega_{\vec{k}\vec{n}}$ of $\vec{H}_{\vec{k}\vec{n}}(\vec{r})$ and therefore the dispersion relation of the eigenmodes – which is equal to the photonic band structure – is obtained [74].

The presented approach based on the Fourier expansion of the dielectric function and the magnetic field is called the plane wave expansion method. For a given wave vector \vec{k} all frequencies are found for which an electromagnetic wave can propagate through the photonic crystal. All calculations of the dispersion relation of photonic crystals discussed in this thesis were carried out with the software MIT photonic bands package that applies the plane wave expansion method [75]. In it the photonic crystal structure is defined by a unit cell in real space that is periodically repeated based on a defined lattice.

Scalability

No fundamental length scale can be found in the derivation of the theoretical description and numerical treatment of photonic crystal structures. The only input describing the dielectric structure comes from the dielectric function $\varepsilon(\vec{r})$ and its assumed periodicity. A photonic crystal structure that is rescaled by a factor s , i.e. $\vec{r}' = s\vec{r}$, is described by a dielectric function $\varepsilon'(\vec{r}) = \varepsilon(\vec{r}/s)$. With it, the master equation Eq. 3.11 is transformed to:

$$s\nabla' \times \left(\frac{1}{\varepsilon(\vec{r}'/s)} s\nabla' \times \vec{H}(\vec{r}'/s) \right) = \left(\frac{\omega}{c} \right)^2 \vec{H}(\vec{r}'/s) \quad (3.18)$$

with the curl operator $\nabla' = \nabla/s$. The dielectric function $\varepsilon(\vec{r}'/s)$ is identical to $\varepsilon'(\vec{r}')$. Dividing both sides with the scaling factor s^2 the master equation for the rescaled problem is derived:

$$\nabla' \times \left(\frac{1}{\varepsilon'(\vec{r}')} \nabla' \times \vec{H}(\vec{r}'/s) \right) = \left(\frac{\omega}{cs} \right)^2 \vec{H}(\vec{r}'/s) \quad (3.19)$$

This is an equivalent description of Eq. 3.11 with new modes $\vec{H}'(\vec{r}') = \vec{H}(\vec{r}'/s)$ and new frequencies $\omega' = \omega/s$. That means, if a photonic band structure is calculated for a certain photonic crystal structure, then the solutions for all crystal structures scaled by a factor s with respect to the calculated one are determined just by scaling the modes and frequencies by the same factor s . To give an example: A photonic crystal and a photonic crystal that is twice as large as the first one have the same dispersion relation. Only the frequency values of the twice as large structure are half the values of the other structure. The same arguments hold true for different dielectric constants: If two materials are used with a dielectric constant that differs by a factor s^2 , then the modes are the

same for both photonic crystal structures and only the frequency changes by a factor $1/s$.

Because of the scalability of the dispersion relation, the photonic band structures are given in dimensionless quantities with the lattice constant a of the photonic crystal structure in real space. The wave vectors \vec{k} are given in units of the size of the reciprocal lattice cell $2\pi/a$ and the frequencies are given in units of $2\pi c/a$.

3.4 The Photonic Band Gap

The development of photonic crystals has mainly been driven by their potential of possessing photonic band gaps. These gaps are frequency ranges for which no electromagnetic wave is permitted to propagate, i.e. no eigenmode exists. The photonic crystal can be considered as an ‘optical isolator’. Furthermore, it is possible to introduce defects in such photonic band gaps resulting in localized states.

3.4.1 Selected Designs with a Complete Photonic Band Gap in 3D

Various structures and designs are known to form complete photonic band gaps in all three dimensions. In contrast to the findings in [72], an fcc lattice was later on proven to exhibit a complete photonic band gap between the eighth and ninth band [76]. Beside the Yablonovite that was already presented in the introduction of this chapter (see Fig. 3.2), some other structures should be mentioned shortly. Further investigations on the diamond lattice yielded a design called layer-by-layer or woodpile structure (theory: [77], experiment: [78] (photonic band gap at microwave wavelengths) [79, 80] (photonic band gap at infrared wavelengths)). It consists of layers of rods where every layer is rotated by 90° with respect to the former layer. Every second layer has its rods aligned parallel but with an offset of half the lattice constant. Therefore, this structure repeats itself every four layers (Fig. 3.3a). With this design band gap widths of up to $28\%^2$ were predicted [77]. The inversion of this structure in germanium shows a band gap of 25% [81].

In a further development of the Yablonovite shown in Fig. 3.2 a new class of so-called slanted-pore photonic crystals has been proposed in Refs. [82] and [83]. Starting from a mask (i.e. a two-dimensional lattice), two to four pores per unit cell are drilled under certain angles to the surface. This design can have a complete photonic band gap of up to 25% for air rods in silicon. The advantage of these structures is a large and robust band gap which makes them less susceptible to fabrication tolerances. One of the design proposals was realized using the direct laser writing process introduced in section 1.4 (see Fig. 1.8c) [51]. However, the direct laser writing process is carried out in SU-8 the refractive index of which is about 1.6 and therefore the refractive index contrast is too low to open a complete photonic band gap.

To overcome this problem the written structures have to be replicated in a high refractive index material, for instance silicon. This is possible as demonstrated in [84]: A woodpile structure fabricated by direct laser writing in SU-8 is infiltrated with SiO_2 in a chemical vapor deposition (CVD) process. After the whole surface of the structure is covered, the SU-8 is removed with RIE and an inverted replica of the original structure is obtained. In a second CVD process the

²The width of the photonic band gap is given as the ratio of its width in normalized frequencies to the center frequency.

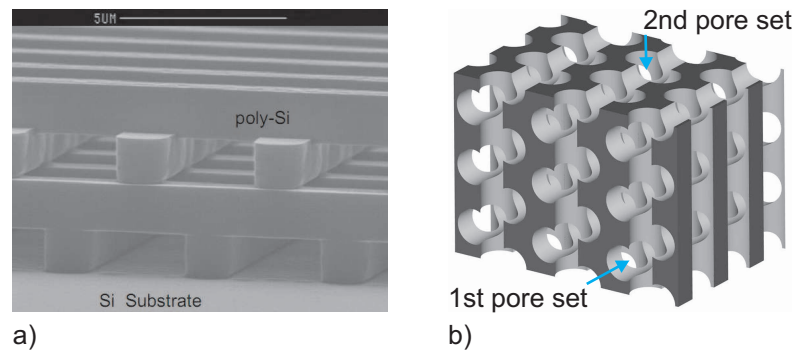


Figure 3.3: 3D photonic crystal designs with a complete photonic band gap. a) SEM cross sectional view of the woodpile structure fabricated in silicon. The rods have a width of $1.2\ \mu\text{m}$ and a spacing of $4.2\ \mu\text{m}$ (picture taken from Ref. [79]). b) The Hallite. First, a hexagonal pattern is electrochemically etched into silicon. A second set of pores is manufactured perpendicular to the first one, penetrating each other.

originated cavities were filled again with Si and thus a replica of the SU-8 structure is obtained. In principle, this approach can be applied to any structures obtained by direct laser writing or holographic laser lithography which opens up a variety of different designs that can be realized.

Further proposals closely related to slanted-pore photonic crystals are the Kielovite, the square spiral and the Hallite. The Kielovite (named after the German city Kiel) has been synthesized using macroporous silicon [85]. It utilizes the property of macroporous silicon pore growth that takes place preferentially in $\langle 100 \rangle$ and $\langle 113 \rangle$ direction. Therefore, on a $\{111\}$ surface three equivalent pores in $\langle 113 \rangle$ direction grow. In contrast to the Yablonovite the pores are tilted by 29.5° (determined by the angle between the crystal directions) to the surface normal instead of 35° . The width of the photonic band gap was shown to be 8% and can be increased up to 16% if the pores are diameter-modulated [86].

Square spirals with up to 24% width of the photonic band gap were predicted by Toader and John [87] and realized with direct laser writing by Seet et al. [88]. In contrast to the slanted pores, these square spirals have additional bends of 90° in the plane normal to their growth direction.

Finally, the Hallite is a photonic crystal structure that can be realized within the macroporous silicon process (Fig. 3.3b). It consists of two sets of hexagonal arranged straight pores that are orthogonally to each other. For the case of silicon with air pores a band gap of 25% is possible [89]. The first set of pores is etched with the macroporous silicon etching process. The second set perpendicular to the first one is manufactured with a focused ion beam so that they penetrate the first set of pores [90].

Another route to photonic crystal structures has been taken via the self-assembly of spherical objects (cf. section 1.4). However, the assembly of monodisperse dielectric spheres gives no complete photonic band gap. Only the inversion of this structure, that means low dielectric spheres in a high dielectric matrix, possesses a complete 3D photonic band gap of 5 – 15%, depending on the infiltration material [91]. Such crystals were fabricated with band gaps in the region of $1.5\ \mu\text{m}$ wavelength [92, 50].

The simple cubic lattice cannot be obtained via self-assembly methods. Nevertheless, also this structure can feature a complete photonic band gap. In Ref. [93] a scaffold-like structure and a structure with overlapping air spheres were investigated. The latter one was also proposed to

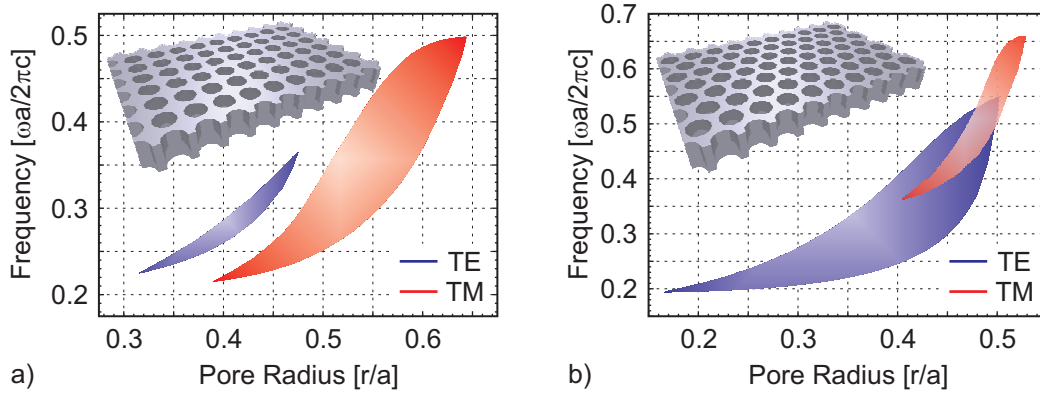


Figure 3.4: Size of the lowest photonic band gap in dependence on the pore diameter for square (a) and triangular (b) lattices of $\varepsilon = 12$. The pore radius and the frequency are given in units of the lattice constant a . The sizes were calculated with the MIT photonic bands package [75].

serve as 3D photonic crystal made of macroporous silicon [94]. Its sophisticated fabrication is the topic of section 3.4.4 below.

This listing is not complete and rather gives an idea of the versatility of pore geometries and fabrication routes leading to photonic band gap structures. Although models were shown with large complete photonic band gaps in 3D, from an experimental point of view also the efforts and costs for their fabrication have to be taken into account. In particular, the stability of the design has to be considered and to which degree irregularities reduce the photonic crystal properties, e.g. the width of the photonic band gap.

In conclusion, large band gaps can be obtained with serial fabrication techniques because also difficult design rules can be realized. However, the costs to scale-up these approaches are very high. Therefore, the self-assembly seems to be a solution despite smaller band gaps and less degree of freedom in the design of photonic band gap structures. In a recent publication a new route has been shown to obtain photonic crystals with a complete photonic band gap in the visible region (still not realized so far) via self-assembly [95]. Among other approaches, photonic crystals made of macroporous silicon are very promising. On the one hand they are compatible with complementary metal oxide semiconductor (CMOS) processes and easily scalable. On the other hand they offer sufficient freedom for the design of photonic crystals as can be seen in the case of the Hallite or the simple cubic geometry discussed in the following sections.

3.4.2 2D Photonic Crystals

Although a complete photonic band gap is mandatory for controlling the emission of a dipole, not every application requires a complete photonic band gap. In contrast to 3D photonic crystals 2D pore arrangements can only possess a photonic band gap in the in-plane direction. Nevertheless, 2D periodic structures including linear defects can be used to guide light as discussed in the next section.

In the case of 2D photonic crystals it can be distinguished between two polarization directions of the electromagnetic wave with respect to the pore geometry: While in the transverse electric (TE) mode the electric field oscillates perpendicular to the pores, in the transverse magnetic (TM) mode the electric field is parallel to the pore axis. Strictly speaking this is only true for 2D

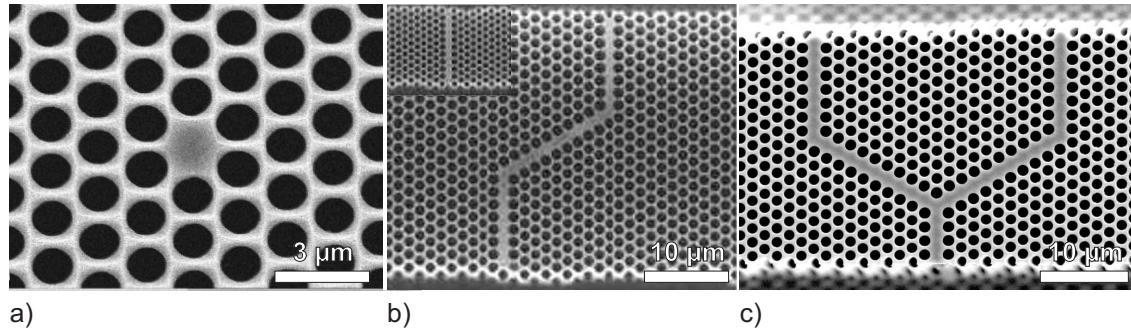


Figure 3.5: SEM pictures of defect structures realized in a 2D PC with a hexagonal lattice of lattice constant $a = 1.5 \mu\text{m}$. a) A single missing pore. b) A waveguide that can bend the light sharply around corners and even split one beam in two parts (c). [100, 101]

structures with infinite extension in the direction of the pores, i.e. the z -direction. Because only then there is no dependence on the z -direction and the two vectorial equations Eqs. 3.3 and 3.4 are decoupled.

In Ref. [96] the square, triangular and honeycomb lattices are considered for the case of GaAs with a dielectric constant of $\epsilon = 13$. For individual polarization directions in every lattice type photonic band gaps can be found. In contrast, the special case of a band gap for both polarization directions is only fulfilled for the triangular arrangement of pores in a dielectric matrix. However, for the square lattice consisting of dielectric rods a complete photonic band gap in 2D could be found for a dielectric constant larger than 12.3 [97].

In Fig. 3.4 for the square and the triangular lattice the frequency range of the lowest photonic band gap in dependence on the pore radius is shown. The calculations were performed with the MIT photonic bands package (cf. section 3.3) for a dielectric constant of $\epsilon = 12$, corresponding to silicon in the infrared region. In the case of the square lattice (Fig. 3.4a) the photonic band gaps for the TE (blue area) and TM (red area) polarization occur in separated frequency and pore radii ranges. In a hexagonal lattice there is an overlap of both ranges resulting in a 2D complete photonic band gap. The largest size of this complete photonic band gap can be obtained for a pore radius of $r = 0.48a$ (with a the in-plane lattice constant) and is limited by the TM mode to 18% around a mid-gap frequency of $\omega a/2\pi c = 0.485$.

3.4.3 Defects in Photonic Crystals

Suppressing the propagation of electromagnetic waves of certain frequencies is not the only application of the photonic band gap. Introducing defects in the photonic crystal structure disrupts the periodicity of the crystal and it is possible to create optical states within the photonic band gap [98]. By engineering the properties of these defect states, light coupling to these states is localized and can be manipulated [99].

Within the macroporous silicon material system defects can be realized with an accordingly designed mask: A single missing etch pit gives a point defect (Fig. 3.5a). An electromagnetic wave package is localized at the location of a point defect if it is in resonance with the eigenfrequency of such a defect state [102]. Because of the photonic band gap the wave package cannot escape through the surrounding pores since no corresponding Bloch mode exists in the photonic

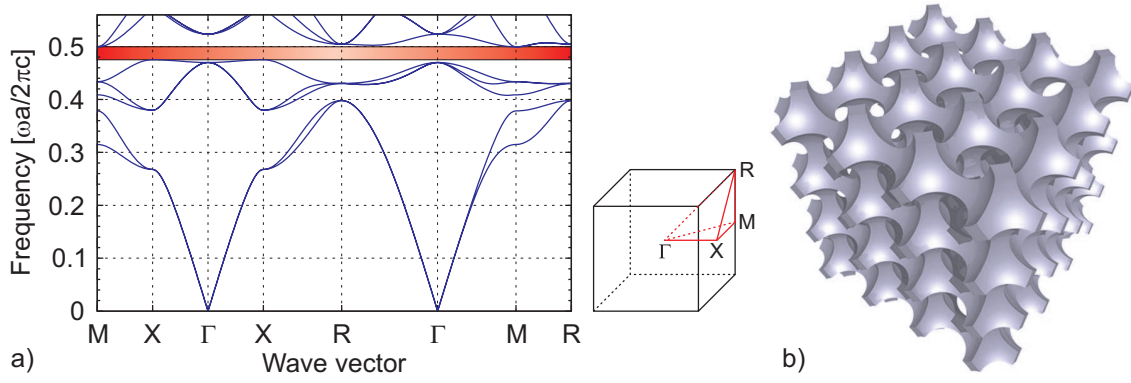


Figure 3.6: A photonic crystal structure with simple cubic geometry made of silicon ($\epsilon = 11.7$) with overlapping air spheres (diameter $r = 1.21a$). a) The photonic band structure reveals the complete photonic band gap marked by the red bar. It has a width of 4.8% with respect to the center frequency of $\omega a/2\pi c = 0.488$ between the fifth and the sixth band (normalized frequencies between $\omega a/2\pi c = 0.476$ and $\omega a/2\pi c = 0.500$). For the definition of the high symmetry points in the k -space the reciprocal unit cell is also represented. b) A visualized 3D model of the corresponding photonic crystal structure consisting of $3 \times 3 \times 3$ periods of the unit cell.

crystal. Consequently, the light is stored at the location of a defect within the photonic band gap. Combining several point defects to a line defect can thus guide the light sharply around corners (Fig. 3.5b) or split it into two separate beams (Fig. 3.5c).

Apart from guiding light on a defined path, defects within the photonic band gap are used to inhibit spontaneous emission [103]. In 2D photonic crystals an additional confinement of light in the third dimension is required, e.g. by total internal reflection. Thus, an optical cavity is established and the photonic band gap controls which modes are allowed or suppressed. With this approach of microcavities in photonic crystals it is possible to construct thresholdless lasers [104]. This concept was also extended into 3D photonic crystals. Ogawa et al. [105] produced a defect layer within a woodpile structure (cf. section 3.4.1) and introduced a light emitting material (GaInAsP) at this position. Lodahl et al. [106] used quantum dots embedded in inverted opal structures instead.

3.4.4 3D Simple Cubic Photonic Crystal

This section is dedicated to the design of a 3D photonic crystal structure in a simple cubic geometry. The theoretical treatment of this structure as well as an instruction how to realize the model with the help of the macroporous silicon etching process was published by Leonard in 2002 [94]. The unit cell of this photonic crystal structure consists of a block of silicon with an inscribed air sphere of a diameter 1.21 times the lattice constant a ($r = 0.605a$). This implies that neighboring spheres overlap each other (Fig. 3.6b). The size of the complete photonic band gap is 4.8% around the center frequency of $\omega a/2\pi c = 0.488$ as marked by the red bar in Fig. 3.6a. It has its minimum at the X point in the fifth band and the maximum at the M point in the sixth band.

For the experimental realization of this structure a strongly modulated pore shape is required with a periodicity of the modulation equal to the lattice constant. The cross section of a sample with $2\mu\text{m}$ lattice constant is shown in the first row of Fig. 3.7. Such a pore shape can be obtained by a modulation of the current and the voltage (Fig. 3.7e). Thereby, the most important part is

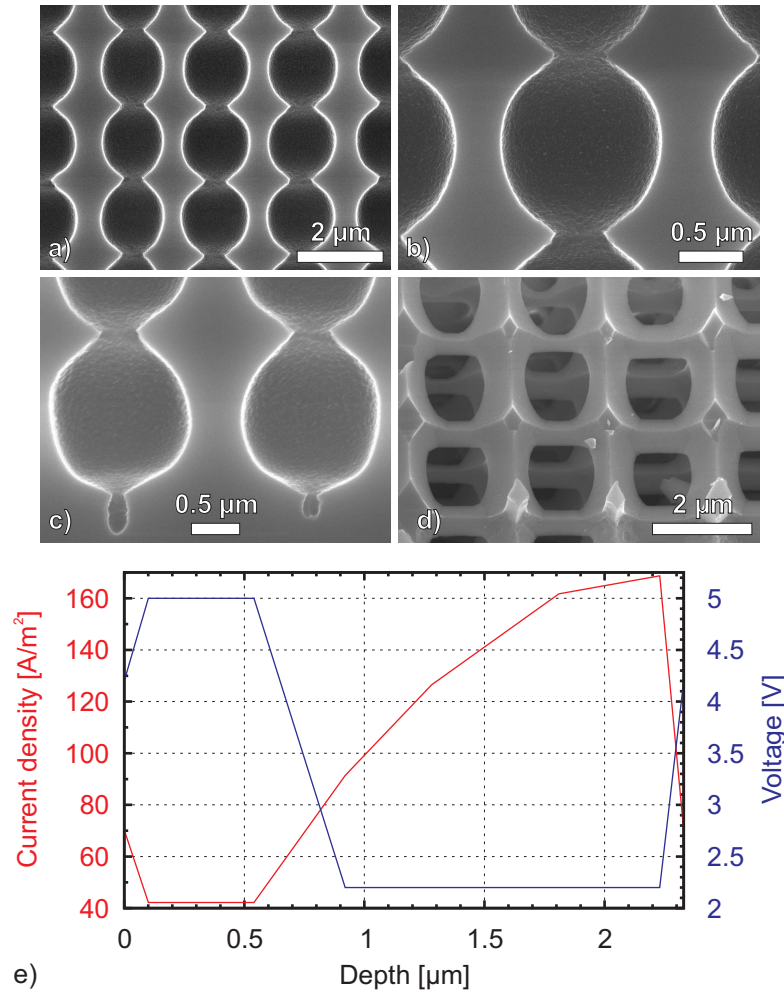


Figure 3.7: Fabrication of a 3D photonic crystal structure in simple cubic geometry within macroporous silicon. a) Cross sectional view of three-by-three modulations. b) One single modulated pore. c) In the beginning a new tiny pore is formed supported by charge carriers generated by electric breakdown. d) After isotropically etching the sample (four times two hours oxidation at 900°C and subsequent oxide removal in NH_4F) the pores get connected to neighboring pores as can be seen in this tilted view. e) The current-voltage diagram used for etching one modulation.

the formation of a tiny pore in the beginning of each modulation (Fig. 3.7c). During this stage a considerable amount of charge carriers is generated by electric breakdown due to the increased voltage and the small radius of curvature. A detailed description of the pore formation is given in Ref. [31].

In order to match the design rules given in the model of overlapping air spheres (Fig. 3.6b) the pores require to get connected to each other not only in the etching direction but also in the lateral dimension. For that purpose the isotropic etching procedure as described in section 1.3.2 was applied. Overall, four iterations of oxidizing the sample (two hours at 900°C) and subsequently removing the oxide in NH_4F (12.5 wt%) were carried out. In each step a silicon layer of about 80 nm thickness was removed isotropically from the entire surface. Thus, neighboring pores got connected to each other in the direction perpendicular to the etching direction (cf. section 2.2). But there is still a certain amount of silicon left so that the whole structure remains stable. The isotropically widened structure is shown in Fig. 3.7d. In this micrograph the sample was tilted

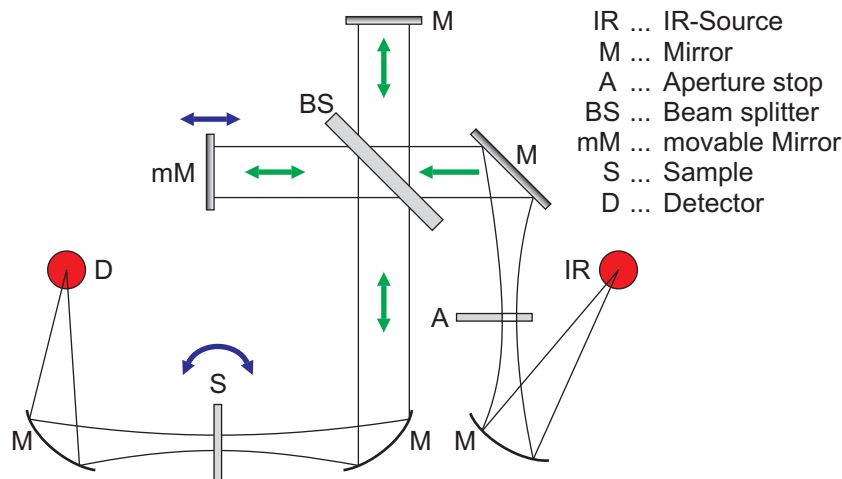


Figure 3.8: Scheme of the main components of an FT-IR spectrometer: An infrared light source (IR, silicon carbide), a Michelson interferometer consisting of a potassium bromide (KBr) beam splitter (BS), a fixed (M) and a position-controlled movable mirror (mM). The sample (S), measured in transmission, can be rotated via a motor-driven rotation stage and the intensity is detected with a mercury cadmium telluride (MCT) detector (D).

in such a way that the remaining silicon bars lying behind the first layer are visible, too. As reported by Matthias et al. [107], the quality of the fabrication process and the obtained structures could be improved up to the high demands necessary for photonic crystal applications. For a similar structure with a lattice constant of $a = 1.5 \mu\text{m}$ photonic stop bands were measured in the (100) direction at wavelengths of about $3 \mu\text{m}$ and $5 \mu\text{m}$, respectively.

3.5 Fourier Transform-Infrared Spectrometry

In the frame of this work a Fourier transform-infrared (FT-IR) spectrometer (Bruker IFS 66/S) was used to optically characterize the etched macroporous silicon samples in the mid-infrared region of the electromagnetic spectrum. Basically, FT-IR spectrometry is used to detect vibrational and rotational modes of molecules [108]. Thus, it is sensitive on chemical bonding and composition of solids, liquids, and gases.

In Fig. 3.8 the main components of an FT-IR spectrometer are shown. A silicon carbide filament (also called glow bar) is used as a light source. The light is coupled into a Michelson-interferometer with a position-controlled movable mirror. After passing the interferometer the beam hits the sample. For the detection of the transmitted intensity a mercury cadmium telluride (MCT) detector (cooled with liquid nitrogen) is used which is sensitive in the near- and mid-infrared region between $1 \mu\text{m}$ and $14 \mu\text{m}$ wavelength. Additionally, the sample chamber was expanded with a rotation stage that allows to manipulate the rotation of the sample with respect to the y-axis (the axis normal to the plane of beam propagation). In a modified version (Bruker Hyperion) this setup can also be used to measure the sample in reflection mode.

The measurement principle in an FT-IR spectrometer is based on the interference of two beams. During a measurement the position of the movable mirror in the interferometer is altered stepwise. For every position of the mirror the intensity measured by the detector is recorded. A

helium-neon laser working at a wavelength of $\lambda = 632.8\text{nm}$ is coupled into the interferometer as well and serves as a reference signal. Constructive interference of the two beams from the interferometer arms occurs if the difference in the optical path length is a multiple of the wavelength. Each arm of the interferometer is passed two times by the beam. Thus, between two interference maxima the mirror moved by half of the wavelength of the reference signal, i.e. by $\delta x = 316.4\text{nm}$. In this way, the mirror position is determined.

If the optical paths in the two arms of the interferometer are identical in length, every wavelength emitted by the IR-source interferes constructively at the place of the detector. When the movable mirror is deflected from this zero position the detected intensity for each wavelength follows a cosine function. The detector records the sum of the intensities from all cosine functions depending on the shift x of the movable mirror. An intensity spectrum $I(x)$ – the interferogram – is obtained:

$$I(x) = \frac{1}{\sqrt{2\pi}} \int_B I(\tilde{\nu}) \cos(2\pi\tilde{\nu}x) d\tilde{\nu} \quad (3.20)$$

Thereby, B is the bandwidth of the light source, x the shift of the mirror position with respect to the zero position, and $\tilde{\nu} = \frac{1}{\lambda}$ the wavenumber. The integral can be expanded from minus infinity to plus infinity if the finite bandwidth of the spectrum of the IR-source is put into a truncation function $D(\tilde{\nu})$ which is equal to one in the interval of the bandwidth and zero at all other points:

$$I(x) = \frac{1}{\sqrt{2\pi}} \int_{-\infty}^{\infty} I(\tilde{\nu}) D(\tilde{\nu}) \cos(2\pi\tilde{\nu}x) d\tilde{\nu} \quad (3.21)$$

Via a fast Fourier transform algorithm the interferogram $I(x)$ is transformed into $I(\tilde{\nu})$, the spectrum of the system in dependence on the wavenumber $\tilde{\nu}$:

$$I(\tilde{\nu}) = \frac{1}{\sqrt{2\pi}} \int_{-\infty}^{\infty} I(x) D(\tilde{\nu}) \cos(2\pi\tilde{\nu}x) dx \quad (3.22)$$

If this spectrum is divided by a background spectrum, e.g. a spectrum taken without a sample, the transmission of the sample is obtained.

3.6 Summary

The demands in an absolute unique ordering are very high if macroporous silicon is used as a photonic device. In this chapter the successful application of macroporous silicon as cavity, waveguide, and 3D photonic band gap material were presented. So far, however, the devices feature the discussed photonic properties at wavelengths clearly larger than $1.5\mu\text{m}$ – the figure of merit for telecommunication applications. As implied by the section about the scalability of photonic crystal structures (cf. section 3.3), this working wavelength can be realized if the lattice constant is scaled accordingly.

Chapter 4

Etching Macroporous Silicon in the Sub-Micrometer Range

Under applied aspects the properties of a photonic crystal structure should match a wavelength region used in the telecommunication industry. For the transport of data around the globe optical fibers are used. In order to bridge large distances the attenuation in the fibers has to be minimized. An optimal window is found around a wavelength of $1.55\text{ }\mu\text{m}$, the so-called ‘C band’ (C stands for conventional, $1530 - 1565\text{ nm}$). For larger wavelengths the infrared absorption increases the attenuation whereas in the smaller wavelength regime the Rayleigh scattering (attenuation is inversely proportional to the fourth power of the wavelength) is most pronounced.

Based on the 3D photonic crystal design shown in Fig. 3.6b an appropriate structure was etched in macroporous silicon as described in section 3.4.4. This structure with a lattice constant a of $1.5\text{ }\mu\text{m}$ shows stop bands in the region of $3\text{ }\mu\text{m}$ wavelength [107]. Changing the position of the photonic stop band from $3\text{ }\mu\text{m}$ to $1.5\text{ }\mu\text{m}$ for the same design means that the dimensions of the crystal structure have to be changed by the same factor. Or to be more precise: In order to relate the center frequency ($\omega a/2\pi c = 0.488$) of the photonic crystal with the telecommunication wavelength λ of $1.55\text{ }\mu\text{m}$ the lattice constant a has to be chosen to be $a = 0.488\lambda = 0.756\text{ }\mu\text{m}$. From the scalability of the Maxwell’s equations it results that the band structure calculation can be adapted to arbitrary lattice constants a as long as the value of ϵ remains unchanged for the frequency region under consideration (cf. section 3.3). The calculations in Fig. 3.6a were done for $\epsilon = 11.7$ which is equivalent to a refractive index of $n = 3.42$ corresponding to wavelengths larger than six micrometers. When approaching the electronic band gap at $\lambda = 1.1\text{ }\mu\text{m}$ the dielectric constant of silicon changes considerably. For the case of $1.55\text{ }\mu\text{m}$ wavelength the dielectric constant changes to $\epsilon = 12.1$ (according to a refractive index of $n = 3.48$). As can be seen in Fig. 4.1 the change in the dielectric constant has only a minor impact and therefore the assumptions above hold true. In conclusion, in order to make macroporous silicon competitive for photonic crystal device fabrication the lattice constant has to be reduced to lattice constants in the range of several hundred nanometers. The etching process for structures with a sub-micrometer lattice constant as well as the utilization of the obtained results as optical devices are discussed in this chapter.

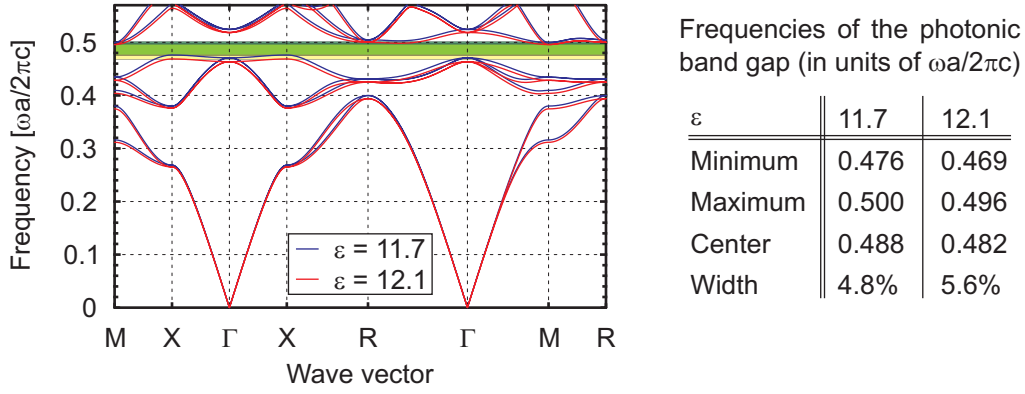


Figure 4.1: Comparative analysis of the photonic band structure for the design of overlapping air spheres (cf. section 3.4.4). While a dielectric constant of $\varepsilon = 11.7$ corresponds to a wavelength of several micrometers, the dielectric constant increases when approaching the electronic band gap. At a wavelength of $1.55 \mu\text{m}$ the dielectric constant has changed to $\varepsilon = 12.1$. In the table, gap position and size are compared to each other for the two different dielectric constants. The band gap shifts slightly towards lower frequencies for the higher dielectric constant. Because of the enhanced dielectric contrast the width of the band gap is enlarged.

4.1 Etching of Straight Pores

For the experiments presented in this chapter phosphorus doped n-type silicon wafers from Wacker Siltronic AG oriented in $\langle 100 \rangle$ direction were used. The resistivity of the material was nominally $0.1 \pm 0.013 \Omega\text{cm}$ corresponding to a doping density of $8 \cdot 10^{16} \text{cm}^{-3}$. The silicon was grown in a float zone process and the wafers measured $300 \pm 15 \mu\text{m}$ in thickness and 100 mm in diameter. Rectangular pieces of 20 to 25 mm side length were cleaved out of the wafer to fit into the etching cell (cf. Fig. 1.1). At the front side of the wafers a mask of KOH etch pits was defined with a lattice constant of $a = 700 \text{nm}$. The pores were arranged in a hexagonal symmetry.

The introduced simple cubic photonic crystal structure cannot be realized with a hexagonal pore arrangement. However, at this point the etching behavior in the sub-micrometer range is studied and therefore the lattice geometry is of minor interest. It could be even argued that a hexagonal lattice is more advantageous since it has a higher symmetry than a square lattice and therefore also the pore etching should be more homogeneous and stable.

The current-voltage characteristic measured between two points at the wafer back side showed a nonlinear behavior with a resistance in the range of several kilohms to megaohms. Hence, an ohmic back side contact had to be established prior to the etching process. Therefore, the following procedure was applied at the edge of each sample: First, two small areas of the back side were ground with fine abrasive paper. Then, a gallium-indium eutectic (Alfa Aesar, gallium-indium eutectic 99.99%, gallium : indium 75.5 : 24.5 wt%) was applied and ground into the silicon to provide a high conductivity contact. After this procedure the excess material was removed. In order to test the quality of this process the resistance between the two contacts was measured with a common circuit analyzer. Resistance values less than 20Ω were considered to be sufficient to use the prepared sample in the etching process. Since the HF-containing etching solution corrodes the gallium-indium contact it has to be made sure that the etching cell is clean and dry and that the contacts are only created at the edge of the sample outside the sealing rings (cf. Fig. 1.1).

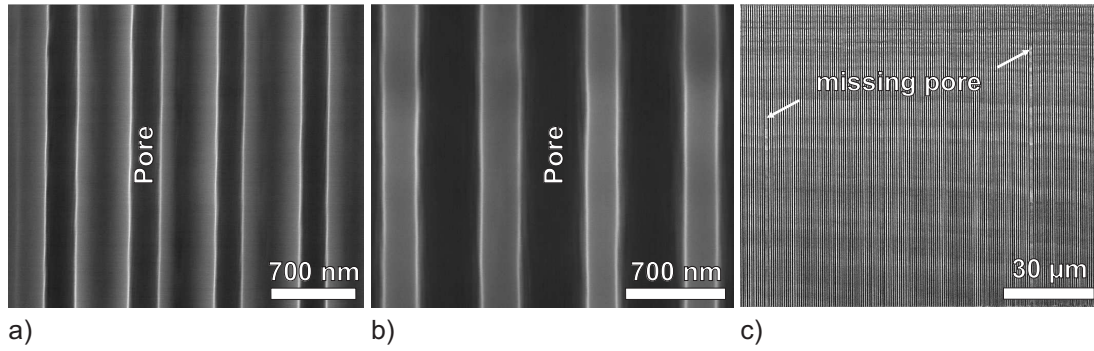


Figure 4.2: SEM micrographs of the cross section of macroporous silicon with a lattice constant of $a = 700\text{ nm}$ and a pore diameter of a) $2r = 240\text{ nm}$ and b) $2r = 480\text{ nm}$. The total pore depth is $50\text{ }\mu\text{m}$ for both samples. c) Homogeneous and stable pore growth could be obtained over $100\text{ }\mu\text{m}$ depth and a mean pore diameter of 280 nm ; even though a few pores did not propagate all the way through the $100\text{ }\mu\text{m}$.

At first, the etching of straight pores with different diameters and aspect ratios should be considered. In principal, the parameters obtained for the etching of pores at larger lattice constants can be transferred: The critical current density J_{PS} is dependent on HF concentration and temperature of the etching solution. Unless otherwise noted the HF concentration was 5 wt% and the temperature was kept constant at 10°C . The porosity p for a given ratio of the pore radius r to the lattice constant a is independent of the lattice constant (cf. Eq. 1.8, e.g. for $r = 0.25a$). Therefore, the etching current density J remains at the same value, too (cf. Eq. 1.7). The voltage was set to $V = 2\text{ V}$. As a surfactant, SDS (0.1 mM) was added to the etching solution.

With these preconditions straight pores of different porosities were etched. Stable pore growth over a depth of at least $50\text{ }\mu\text{m}$ could be achieved for pore diameters between 240 nm ($r/a = 0.17$) and 480 nm ($r/a = 0.34$) (Figs. 4.2a and b).¹ This corresponds to porosity values of 11% and 43%, respectively. Pores with diameters out of this range tended to stop growing or grew together. Analyzing the cross section pictures of several pores gave a standard deviation of 14% for the pore diameter.

Pores with a length of up to $200\text{ }\mu\text{m}$ were etched without a significant lack of pore uniformity. That is equivalent to two-thirds of the wafer thickness and to an aspect ratio of pore length to pore diameter of about $700:1$. In Fig. 4.2c a $100\text{ }\mu\text{m}$ deep etched sample is shown. The pore diameter is $280 \pm 30\text{ nm}$ corresponding to an aspect ratio of about $360:1$. Almost every pore is completely etched and they are all of the same length. In the cross section picture (Fig. 4.2c) two missing pores could be identified separated by approximately 90 pores in between. This means that 99.99% ($1 - 1/90^2$) of the pores have been etched. This value could be confirmed statistically by measuring at different positions of the sample. However, a few pores could be found that differ by thirty percent of the mean pore diameter, e.g. the smallest diameter was 190 nm and the largest was 370 nm . This indicates the existence of parameters that locally disturb the self-stabilizing pore etching process. The influence of several parameters was explored more in detail for modulated pore structures as presented in the next section.

¹In contrast to the discussion in the next sections, no microporous layer can be seen on the sample walls. The sample was stored under ambient atmosphere for a day and the microporous layer was oxidized. Prior to the SEM an HF-dip was performed to lower the influence of statics. So, also the microporous layer was removed.

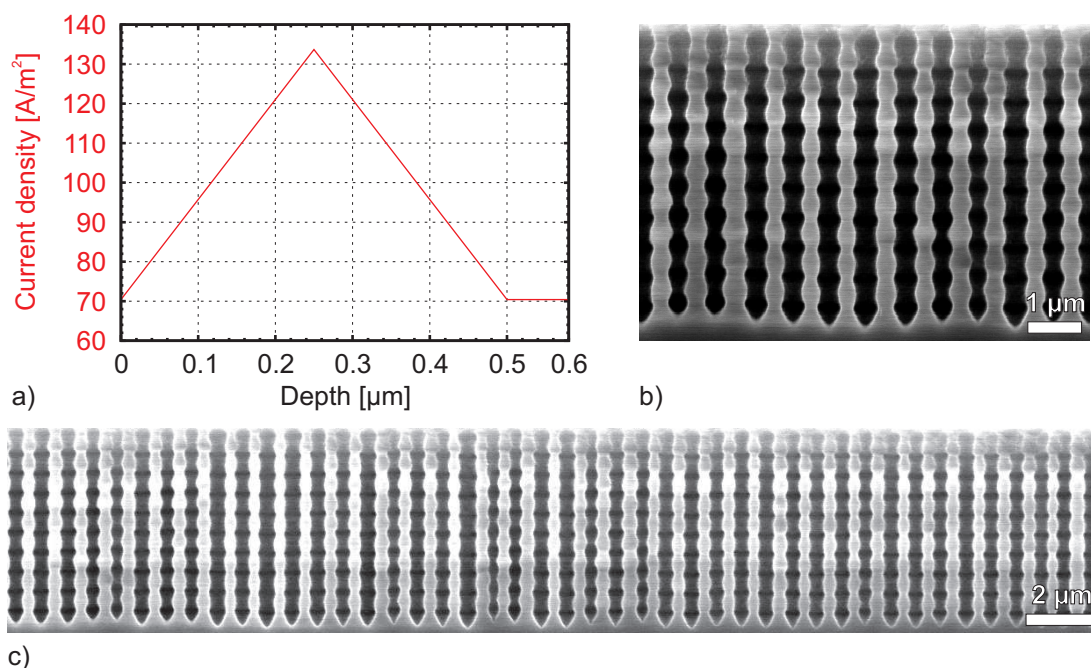


Figure 4.3: Modulation of the pore diameter of macroporous silicon with a lattice constant of 700 nm. a) The applied current density profile consisting of three sections: An increasing current density, a decreasing part and a part with constant current density. b) The cross section of a sample etched with ten repetitions of the modulation profile. Parameters: HF concentration: 4.8 wt%, surfactant: NCW, temperature: 6°C. c) Wide range view of the cross section reveals that all pores are grown, also on larger scale.

4.2 Etching of Modulated Pores

Diameter-modulated pores can be obtained by a modulation of the back side illumination intensity (cf. section 3.4.4). Additionally, the surfactant was changed from SDS to NCW (0.17 mM) since NCW was proven to be more suited for modulated pore growth. In Fig. 4.3a the etching current density is given for a single modulation. It consists of three sections: In the increasing part more charge carriers are provided and the pore is widened in diameter. The reverse is true for the second part: During the decrease of the etching current the pore shrinks in diameter since less charge carriers are available. In the following constant current part, time is given for the system to recover into a steady state. In Fig. 4.3b the result is shown for ten repetitions of this etching profile. The pores are sinusoidally shaped. Their form does not follow directly the applied profile. As already observed for larger lattice constants it is very smooth without sharp spikes [109]. The reason is the altered condition in the SCR. If the current is increased charge carriers are accumulated in the region of the pore tip. In order to consume these additional charge carriers the pore increases in diameter until an equilibrium is established again between provided charges and pore diameter. During this transition time, however, more charge carriers are present at the pore tip than can be consumed. Thus, the focusing effect of the SCR is lowered and therefore the passivation of the pore walls is diminished. The defect electrons do not only react at the tip of the pores but also in areas that were already etched before and the pore shape becomes smeared out.

Another important observation is, that the pores differ in diameter and length. This was also observed for the straight pores in the last section. Furthermore, these two parameters appear to be

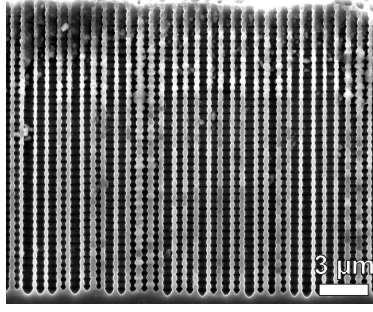


Figure 4.4: With the modulation profile shown in Fig. 4.3a 40 periods were etched. The disorder does not change and the correlation between mean pore diameter and pore length remains unaffected by the increased depth.

connected: Pores with a larger mean diameter are also a little bit longer than those with a smaller diameter. Nevertheless, all pores were etched and they show the same dependencies between diameter and length (Fig. 4.3c).

The found set of parameters was also suited for the growth of deeper pores. Instead of ten modulations the given profile was repeated for 40 times (Fig. 4.4). Still, there are no pores which stop growing or grow together. This emphasizes that the etching process takes place in a stable state within the applied parameters. Furthermore, the offset in length between thicker and thinner pores remains constant and therefore it is independent of the overall pore length. Thus, it can be concluded that this disorder is not caused by the etching process. Instead, an inherent property of the material itself must cause this effect, as discussed in the following section.

4.3 Influence of the Lithography

In the two previous sections the etching of straight and sinusoidally shaped pores was presented. Now, the observed behavior of the correlation between the pore diameter and its length will be discussed. Because this correlation is independent of the pore shape as well as the etched depth, the conclusion is drawn that this disorder effect cannot be prevented by changing the parameters in the etching process itself. Rather, this disorder must be induced by an inherent ordering parameter. Since the initial ordering is given by the KOH etch pits, this extrinsic parameter should be considered more in detail in this section.

Fig. 4.5 shows a comparison of two hexagonal lattices with a lattice constant of 700 nm and 4 μm, respectively. Thereby, the 4 μm lattice belongs to a charge of wafers that has been shown to yield perfectly aligned pores with equal diameters and lengths (cf. Fig. 1.4 on page 10). Although the hexagonal arrangement of the etch pits is clearly visible in both lattices, the 700 nm lattice exhibits a higher degree of disorder. The parameters used for the definition of disorder are the area of the etch pits (defined by their side lengths) and the distribution of the etch pits in the plane. SEM micrographs of the surface were taken for the analysis. To minimize the influence of aberrations only a quadratic region in the center of the SEM pictures was considered for the analysis. Via setting a threshold the pictures were transformed to binary images with one color value for the etch pit areas and the second one for the unetched area. The image analysis of the threshold picture gave a value for each etch pit area. Furthermore, the absolute position of the etch pit center was also determined. Statistical treatment of the obtained data gave the values presented in table 4.1.

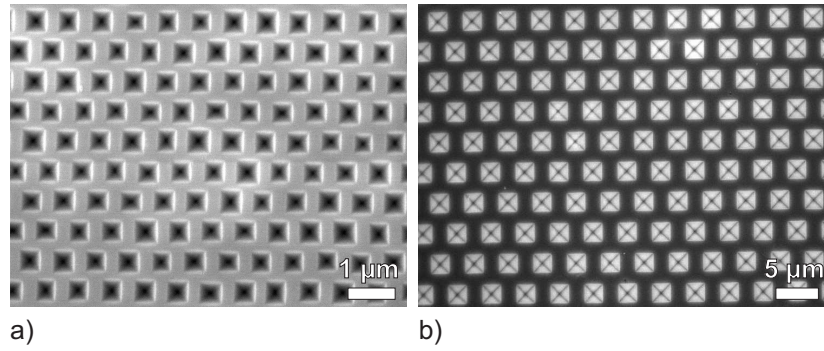


Figure 4.5: The lithographically defined hexagonal lattice for a lattice constant of a) 700 nm and b) 4 μm . The comparison between the two lattices shows that the 700 nm lattice suffers from a significantly higher disorder of the etch pits regarding their size and position.

Lattice constant	0.7 μm	4 μm
Edge length	$0.45 \pm 0.06 \mu\text{m} \hat{=} \pm 13\%$	$2.20 \pm 0.06 \mu\text{m} \hat{=} \pm 2.6\%$
Position	$\Delta x = \Delta y = 1.5\%$	$\Delta x = \Delta y = 1.5\%$

Table 4.1: Comparison between the hexagonal lattice with 700 nm lattice constant and the one with 4 μm . The statistical analysis revealed that the etch pit positions possess the same standard deviation while the deviation of the edge lengths in the 700 nm lattice are comparatively higher.

Because the etch pits are etched into the $\langle 100 \rangle$ oriented silicon by KOH it was assumed that the etch pits have a quadratic shape. Thus, a value and an error for the edge length of the etch pits can be derived from the analysis of the etch pit area. As can be seen in table 4.1 the absolute error of 60 nm for the edge lengths is the same for both lattices. This gives a comparatively higher standard deviation of 13% for the 700 nm lattice compared to the 4 μm lattice with a standard deviation of 2.6%.

The second parameter under consideration was the position of the etch pit. Therefore, the coordinates of the center of the areas were related to a perfectly aligned hexagonal lattice and the deviation was calculated. Remarkably, it is the same relative error of 1.5% for each lateral direction in both lattices. So it can be concluded that the reason for the observed disorder is due to the higher variation of the etch pit edge lengths in the 700 nm lattice.

In the following it should be argued in which way the initial etch pit conditions affect the pore diameters. As revealed by the considerations above, the etch pit diameter of the 700 nm lattice shows a deviation of 13%. After lithographically defining a mask the etch pits are anisotropically etched with KOH. The angle between the wafer surface and the formed $\{110\}$ faces is 54.7° and crystallographically defined. Thus, the visible etch pit diameter from the top view is directly related to the depth of the etch pit: An increased etch pit diameter is related to a deeper etch pit and vice versa. This can be seen in Fig. 4.6a. A cross section of a 700 nm sample is shown and differently sized etch pits can be distinguished. As a result, there is an offset Δz in depth between smaller and larger pores.

The surface conditions also affect the form of the SCR, as schematically shown in Fig. 4.6b. A

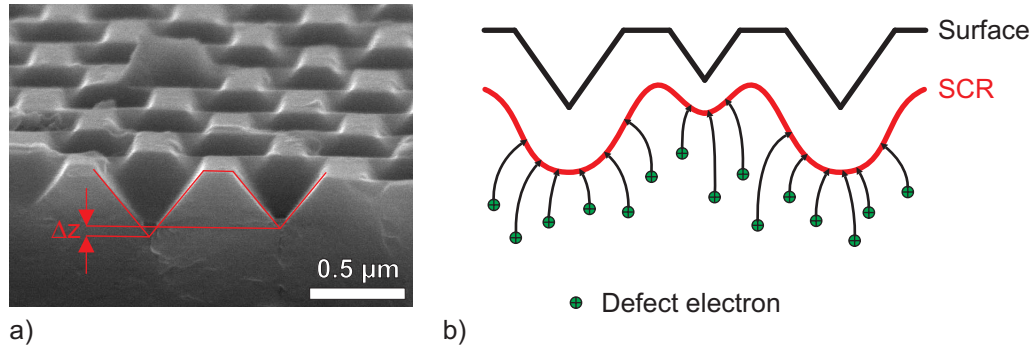


Figure 4.6: Dependency of the etch pit diameter on its depth. a) Bird's eye view SEM micrograph from the edge of a lithographically prepatterned wafer with 700 nm lattice constant. The two cut-through etch pits in the front are of different diameter and hence possess different depths. b) Schematic of the correlation between etch pit diameter and depth. The red line represents an equipotential line in the SCR. Its form is adapted to the altered size of the etch pits.

silicon surface with differently sized etch pits (black line) transfers this variation also to the form of the SCR, represented by an equipotential line (red line). In the vicinity of the large etch pit the SCR extends deeper into the silicon and thus more charge carriers are collected. The smaller etch pit is somewhat behind and collects less defect electrons. Fortunately, the adaption of the SCR ensures a stable pore growth despite the unequal etch pit sizes. The pores regulate their diameter in accordance with the amount of collected charge carriers. The etching speed is independent of their diameter and thus the initial offset remains constant.

Another effect related to this issue concerns the modulation profile. Since the pore etching starts in different depths, the diameter modulation reproduces also this offset. This can be seen by carefully checking Fig. 4.3b or Fig. 4.4: A pore with a very large diameter next to a very small pore forms its modulation maxima slightly deeper than the modulation maxima of the small pore. The reason for this phenomenon is apparent: If the porosity is changed during the etching then this changes the pore diameter at the pore tip. However, due to the etch pit induced variations of the etch front depth, the porosity change takes place in different depths.

The results presented in this section emphasize the importance of a perfectly prepatterned silicon surface. Although most of the pores are etched, an initial disorder in the etch pit lattice propagates into the pore length and diameter. It acts as a source for instabilities and renders the etching of precisely arranged and equally shaped pores impossible. Thereby, the standard deviation of 14% found for the pore diameters in section 4.1 is comparable to the obtained standard deviation of 13% for the etch pit edge lengths. This confirms the proposed interaction between etch pit and pore morphology. A detailed analysis, where differently sized etch pits were introduced intentionally can be found in Ref. [110].

4.4 Etching of Strongly Modulated Pores

In section 3.4.4 the realization of a 3D photonic crystal structure with macroporous silicon was shown. In addition to the current modulation a strong modulation of the voltage is the crucial factor to obtain a pore profile with sharp kinks (Figs. 3.7a and b). This design is necessary for the subsequent pore widening process. The modulated pores with a lattice constant of 700 nm

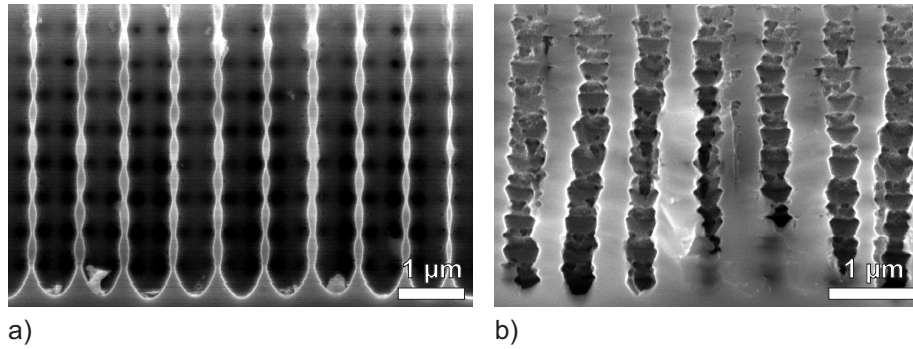


Figure 4.7: Cross section SEM micrographs of modulated macroporous silicon with a lattice constant of $a = 700\text{nm}$. a) After oxidation and treatment in NH_4F a highly porous slightly modulated pore structure is obtained. In the background the modulated pore walls of the next row can be seen. b) Modulated pores etched with a current density and voltage profile directly transferred from two micrometer lattice constant with lengths scaled by factor $0.7/2$. The result is a disordered pore growth with corroded pore walls.

presented so far offer a smooth sinusoidal shape only and are not suitable for the isotropic pore widening process. In Fig. 4.7a a smoothly modulated pore structure, e.g. as presented in Fig. 4.3b, was oxidized for two hours at 900°C and after that the oxide layer was removed in NH_4F . Still, a slight modulation is visible. The black areas in the regions of the thin pore walls denote that a breakthrough towards neighboring pores was established. Thus, the hexagonal pore arrangement is clearly visible. The modulation intensity of the pore diameter, however, is too weak for 3D photonic crystal applications.

The modulation profile shown in Fig. 3.7e produced a well-shaped pore profile for a lattice constant of $2\mu\text{m}$. As discussed in section 4.1 for straight pores, the current densities can be transferred to arbitrary lattice constants. For a fixed J_{PS} the porosity is preserved independently from the lattice constant. This holds also true for a modulated porosity. Only the length scale of the modulation has to be adapted to the new lattice constant. In this particular case the lengths of the profile in Fig. 3.7e were scaled by a factor 0.35 to go from a lattice constant of $a = 2\mu\text{m}$ to $a = 700\text{nm}$. The result (Fig. 4.7b) is clearly different from the expected one: Although sharp kinks are visible the pores tend to leave their preferred growth direction and the walls appear to be corroded.

For a systematic study of how the different parameters influence the pore etching process an asymmetric profile was applied (Fig. 4.8a). In contrast to the profile for sinusoidally modulated pores (Fig. 4.3a), the increasing current density part is now longer with respect to the decreasing one. Furthermore, a strong voltage modulation was applied with a maximum voltage of three volts during the low current density part. Although the higher voltage should increase the focusing effect of the charge carriers to the pore tip, the resulting pores still show a sinusoidal shape (Fig. 4.8b).

In former works it has been observed that the choice of the surfactant has a strong influence on the obtained pore shape [111, 109, 26, 27]. While straight pores are preferentially etched with SDS (anionic surfactant), for the modulated ones NCW (nonionic surfactant) is used (cf. section 1.2). Nevertheless, the modulated pore etching was also carried out with SDS instead of NCW. In Figs. 4.8c and d the resulting pore shape is shown for a sample etched with an identical

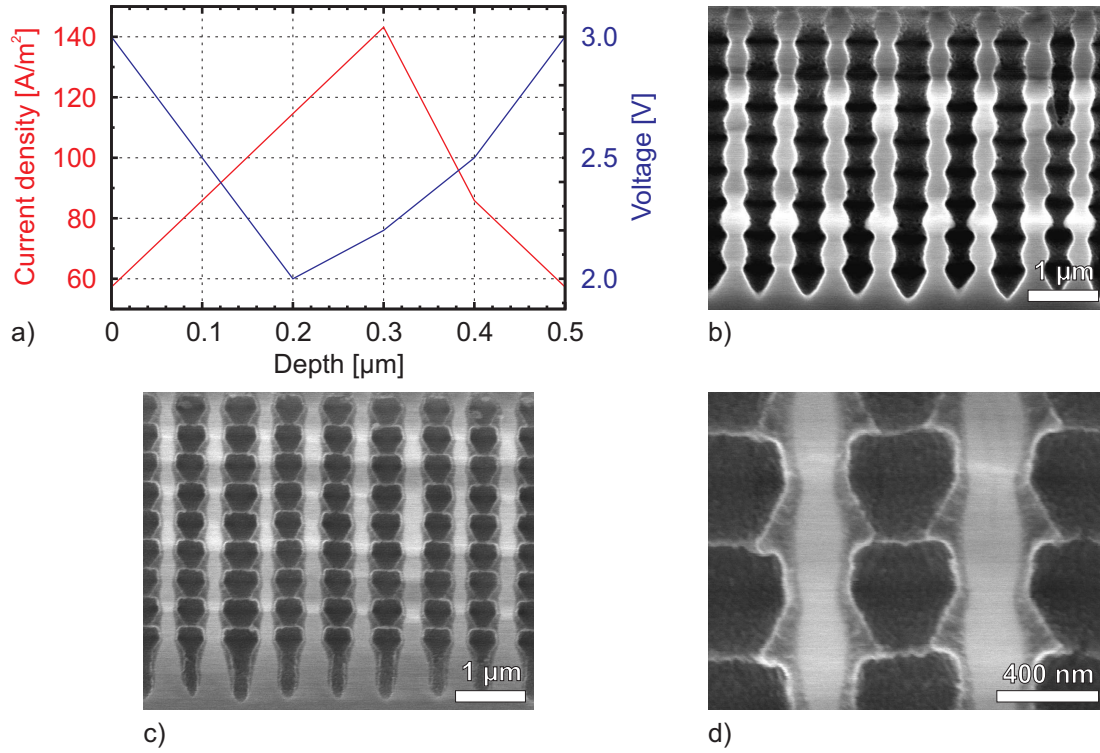


Figure 4.8: For etching pores with sharp kinks, beside the current density also the applied voltage has to be modulated. a) The current density and voltage profile for a single pore modulation. b) SEM cross section view of the resulting pores when NCW is used as surfactant. c) The same modulation profile etched with SDS as surfactant instead of NCW exhibits a clearly different pore shape. d) Magnified version of the pore modulation. Three different areas can be distinguished: A bright area (bulk silicon), covered by a dark-gray film of varying thickness (microporous silicon), and the pore presented by the dark area in the middle and at the border.

modulation profile.² Fig. 4.8d shows a magnified version of the SDS-etched pores. The bright areas represent the remaining silicon. It is slightly modulated in its thickness comparable to the NCW-etched sample in Fig. 4.8b. In addition, a layer is found covering the whole silicon pore wall. It is of lower contrast and develops a sponge-like structure. Furthermore, it shows no dependence on crystal orientation. Therefore, this layer could be identified to be microporous silicon. This could also be proved by luminescence measurements. The contour of this layer forms a drop-shaped pore with a maximum diameter of 430 nm and a minimum diameter of 200 nm. While this kind of surface could be interesting for surface chemistry because of the large surface-to-volume ratio of the microporous layer, it is not suitable for photonic applications. The effective dielectric constant of microporous silicon is considerably lower and therefore only a low dielectric contrast to the air-filled pore is established. The refractive index n_{ps} of a microporous silicon layer can be roughly approximated to:

$$n_{ps} = (n_{si} - 1)(1 - p) + 1 \quad (4.1)$$

For a porosity p of 70% the microporous silicon layer has a refractive index of 1.7 in contrast to

²Only the situation at the pore bottom is different: While in the case of NCW (Fig. 4.8b) the etching was stopped directly after the last modulation, for SDS a section of constant current density and voltage was added.

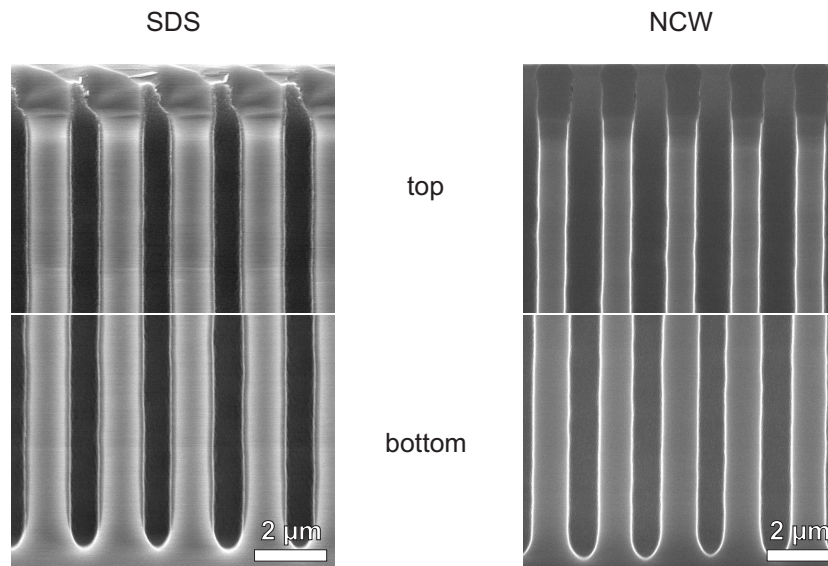


Figure 4.9: Comparison between straight pores etched in SDS and NCW. The samples are 180 μm (SDS) and 200 μm (NCW) deep. For each sample a micrograph was taken from the top and the bottom with a constant magnification of 10 000. In the case of SDS (left sample) no difference in pore diameter is observed between the top part and the bottom part. By contrast, a significant deviation from a constant pore diameter can be seen for NCW.

bulk silicon with $n_{\text{Si}} = 3.4$ [112].

Pores in n-type silicon are etched in an HF containing etchant for current densities below J_{PS} under anodic bias. In the case of meso- and macroporous silicon the etched pore walls are passivated due to the SCR. The formation of microporous silicon, however, is not explained via a SCR but due to a quantum confinement effect [15]. If particle movement is restricted in one or more dimensions due to a potential wall, the energy of the particle increases. This is the definition of quantum confinement. In microporous silicon, the remaining walls have thicknesses of only a few nanometers. As a result, the band gap energy increases compared to bulk silicon and an additional energy barrier for the holes is established. If the energy of this barrier exceeds the bias-dependent energy of the holes, the walls get depleted. They are passivated and the etching stops [24]. The size scale which marks the transition between unrestricted charge carrier movement and the presence of quantum confinement effects is the Bohr radius of an exciton. In crystalline bulk silicon the Bohr radius of an exciton is about five nanometer [16].

With this short explanation of microporous silicon formation the question of the difference between the two surfactants can be answered. For comparison, two samples with straight pores of 200 μm depth were grown: One with SDS added and the other with NCW (Fig. 4.9). For SDS (left image) the typical microporous layer is visible on the pore walls. It has a constant thickness. Such a layer is not visible in the case of NCW (right image). Comparing the pore diameter between the beginning of the pores (top) and their end (bottom) reveals that the pore diameter is constant (0.75 μm) in the case of SDS but changes from 1.16 μm in the beginning to 0.98 μm at the end in the case of NCW. The reason for that is a post-etching of the pore walls due to dark currents. For SDS, these dark currents are significantly lower [26]. A microporous layer forms and passivates the pore walls. No further etching takes place. In an NCW containing etchant the formation of a

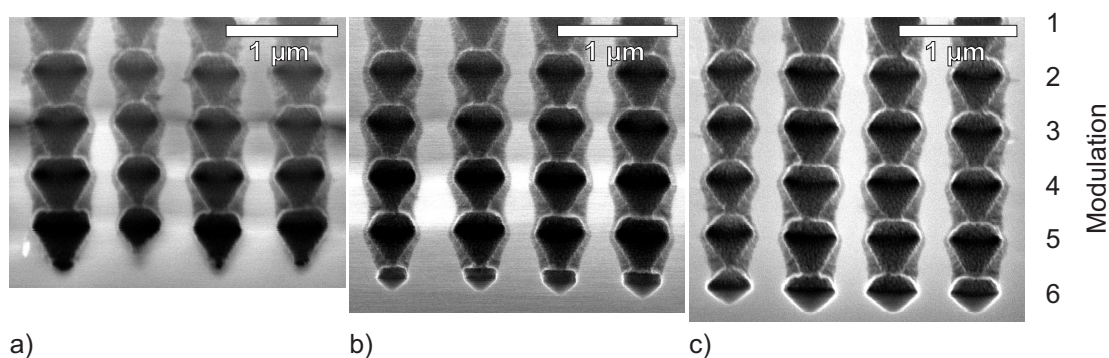


Figure 4.10: Three cross section SEM micrographs of three different samples with the same modulation profile applied. After five modulations the pore formation process was stopped. a) Situation in the beginning of a new modulation period (minimum current, maximum voltage). b) Increasing current density and minimum voltage. c) Situation when the maximum current density is reached.

microporous layer seems to be hindered or, rather, the microporous layer is dissolved immediately after the formation.

The following two assumptions could explain this phenomenon. Firstly, the higher dark currents in NCW lead to a higher porosity of the microporous layer. Secondly, the resulting smaller pore walls are completely oxidized and removed in the HF containing etchant. This happens just before the microporous layer is thick enough to passivate the pore walls. In the case of SDS the pore wall thicknesses of the micropores are higher due to a lower dark current density. The layer can increase in thickness before it is completely dissolved. Charge carriers cannot (or only at a strongly decreased rate) pass this layer. The dissolution of the microporous layer is stopped or at least the dissolution rate is significantly lowered so that no post-etching induced pore widening could be identified from the SEM micrographs.

This crude explanation was not further checked since a detailed investigation of the surfactant and its electrochemistry was not realized in the frame of this work. However, it could be learned that the microporous layer visible in the SDS containing etchant can be seen as an intermediate step to the etching in NCW. The microporous layer shows the intended shape with sharp kinks.

In Fig. 4.10 the modulation of the last pore in an SDS containing etchant is analyzed more in detail. Three samples were etched with the modulation profile given in Fig. 4.8a. The first five modulations were etched completely. Afterwards, the process was stopped at three different points during the sixth modulation. The first picture (Fig. 4.10a) represents the condition in the beginning of the pore formation. The voltage is at maximum while the current density is at minimum (depth of 0 μm in Fig. 4.8a). A small channel with only a few ten nanometers in diameter forms, assisted by the high voltage that produces additional charge carriers due to breakdown. The pore walls of the last complete modulation are still free from a thick microporous layer.

A second picture (Fig. 4.10b) was taken at a depth of 0.2 μm . The current density is increasing to enlarge the diameter of the new pore. The voltage has diminished to its normal value to avoid instabilities due to further generation of breakdown charge carriers. In contrast to the first picture, the fifth modulation is now completely covered with a microporous layer like the preceding modulations.

The third picture (Fig. 4.10c) represents the situation at maximum current density (depth of

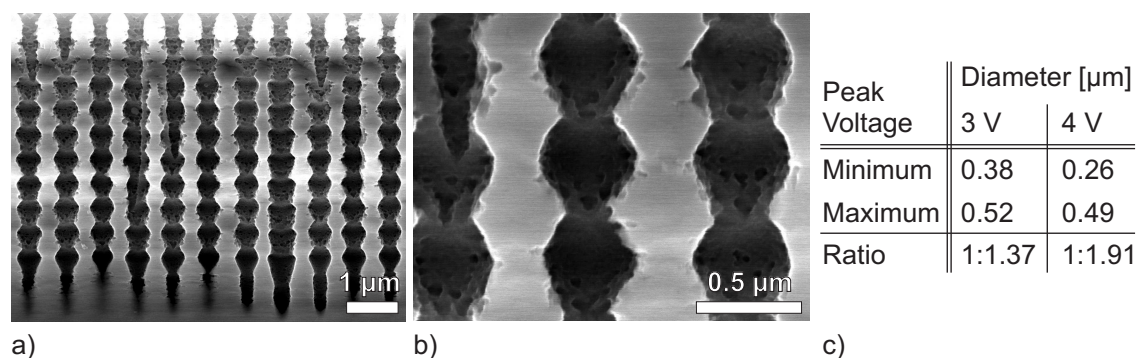


Figure 4.11: SEM cross section of modulated macropores etched with an increased voltage. The pore shape has a higher modulation amplitude but the pores are corroded due to the increased voltage. a) Overview. b) Detailed view. c) In this table the modulation amplitude of the sample etched with an increased voltage of 4 V maximum is compared with the result in Fig. 4.8b for 3 V maximum voltage.

0.3 μm). The pore diameter has reached its maximum. The length, however, will be adjusted during the last steps of the pore modulation while the current density is decreased and the voltage is raised to form a new pore at the bottom. The thickness of the microporous layer of the last complete modulation has slightly increased once again.

While up to the last but one modulation the pore walls are already covered with a microporous layer, the last modulation does not show this feature. This can be seen also in Figs. 4.8c and 4.9 at the bottom of the pores. Since the local current density at the pore tip is always J_{PS} , the pore bottom is electropolished and no microporous layer can be found. But immediately after the formation of a new pore the preceding modulation is affected and a microporous layer is formed. In contrast to the straight pore formation in SDS (Fig. 4.9), the thickness of the microporous layer changes with the modulation. This indicates an additional charge carrier transport beside that of dark currents through the pore walls. In other words, the passivation of the pore wall is not working properly. Charge carriers that are meant to be focused to the pore tip can pass this region and dissolve already etched areas. This effect is most pronounced during the beginning of a new pore formation process. Hence, the pore wall passivation can be accomplished with a higher voltage at this point.

Therefore, the applied voltage was raised from three to four volts in the beginning. The minimum voltage of two volts remained unchanged (cf. Fig. 4.8a). Because the voltage decreases linearly from four to two volts, the voltage is higher during the first 0.2 μm of the new pore formation. As predicted by the considerations above the thickness of the microporous layer could be diminished. The obtained pore shape – already etched in NCW containing etching solution – is shown in Fig. 4.11. In comparison to Fig. 4.8b the ratio of minimum to maximum pore diameter is increased from 1.4 to 1.9 (cf. Fig. 4.11c). The pore walls, however, appear to be corroded (Fig. 4.11b). A further increase in the applied voltage amplified this phenomenon.

An increased voltage means an increase in the electrical field strength, too. In the case of the small pores with only a few ten nanometers radius of curvature, the local electric field strength is significantly increased. Therefore, the threshold for generating charge carriers by tunneling is lowered. During the time of increased voltage the chance of initiating a local current burst is

enhanced. This is visible in the diminishing diameter part of a modulation: Small side pores are etched and corrode the pore walls.

To summarize this section, the etching of strongly diameter-modulated pores in highly doped n-type silicon works close to physical limits. On the one hand an increased voltage is necessary to etch a tiny pore in the beginning that can be widened afterwards. On the other hand the high doping density limits the increase of voltage due to the generation of charge carriers by tunneling. However, the doping density itself defines the width of the SCR and is thus not freely adjustable. The open question is, whether a change in the doping density can significantly improve the etching conditions or not. Therefore, the next section is dealing with the space charge region and their dependency on doping density and pore geometry.

4.5 Space Charge Region and Breakdown

In Eq. 1.1 the width of the SCR is dependent on voltage and doping density. But the derivation of this equation is only true for a planar silicon-electrolyte interface. The presented case of small pores with a radius of curvature of only some ten nanometers is quite different from that. Due to the hemispherical-like bent pore tip the electric field strength is locally increased and can exceed the limit of electric breakdown. In silicon with a doping density of $N_D = 8 \cdot 10^{16} \text{ cm}^{-3}$ considered in this chapter, this limit is reached at a breakdown electric field strength $E_{bd} = 5.7 \cdot 10^5 \text{ V/cm}$. Based on Ref. [113] it can be calculated using the following approximation:

$$E_{bd} = \frac{4 \cdot 10^5}{1 - 1/3 \cdot \lg(N_D/1 \cdot 10^{16})} \quad (4.2)$$

where the doping density N_D is taken in units of cm^{-3} and E_{bd} in V/cm . The assumption of a planar interface is not a valid approximation for small radii of curvature anymore. Therefore, this section will discuss the relation between the applied voltage, the doping density, the influence of the pore tip geometry, and the resulting SCR.

The differential form of Gauss' law in electrostatics for a linear medium is

$$\vec{\nabla} \cdot \vec{E}(\vec{r}) = \frac{\rho(\vec{r})}{\epsilon \epsilon_0} \quad (4.3)$$

with $\rho(\vec{r})$ the free electric charge density, $\epsilon = 11.9$ the dielectric constant of silicon and ϵ_0 that of free space. The electric field $\vec{E}(\vec{r})$ can be derived from the scalar electric potential field $\varphi(\vec{r})$:

$$\vec{E}(\vec{r}) = -\nabla \varphi(\vec{r}) \quad (4.4)$$

Thus, Eq. 4.3 can be expressed as

$$\Delta \varphi(\vec{r}) = -\frac{\rho(\vec{r})}{\epsilon \epsilon_0} \quad (4.5)$$

which is the Poisson equation with Δ being the Laplace operator.

It is assumed that all dopants in the SCR are ionized. This is the so-called depletion approximation and can be justified by the potential drop over the SCR (cf. section 1.2). That gives $\rho(\vec{r}) = -eN_D$ for $0 \leq r \leq W_{SCR}$ with e the elementary charge and N_D the doping density. The

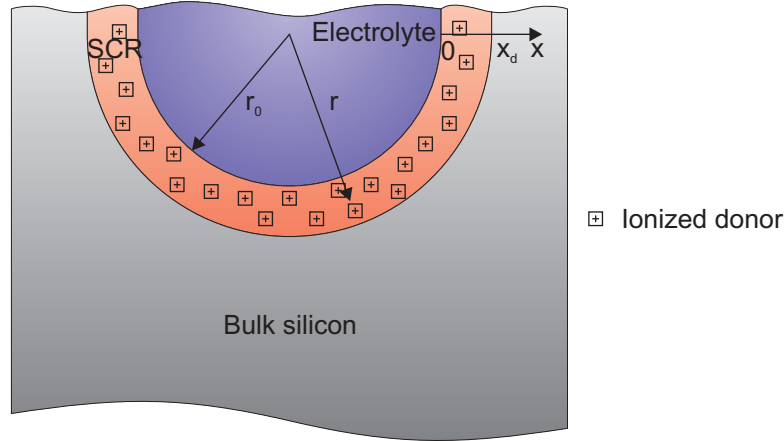


Figure 4.12: Schematic cross section of the silicon-electrolyte interface in spherical geometry. The SCR ranges from the interface ($r = r_0$) until a depth of $r = r_0 + x_d$ with r_0 the radius of curvature.

first integration of Eq. 4.5 gives the electric field. In the case of a planar silicon-electrolyte interface ($\vec{r} = r$) it has its maximum at the interface ($r = 0$) and is linearly decreasing towards zero at $r = W_{\text{SCR}}$.

Integrating Eq. 4.5 for a second time gives the potential $\phi(r)$ which is proportional to r^2 . The bias applied between electrolyte and silicon drops over the SCR and thus the width of the SCR is determined (cf. Eq. 1.1).

To reproduce the conditions at the pore tip more precisely, Eq. 4.5 has to be solved for spherical geometry³:

$$\Delta \phi(r) = \frac{1}{r^2} \frac{d}{dr} \left[r^2 \frac{d}{dr} \phi(r) \right] = \frac{eN_D}{\epsilon \epsilon_0} \quad (4.6)$$

The boundary conditions for the integration can be seen in Fig. 4.12: The SCR ranges from $r = r_0$ to $r = r_0 + x_d$ and the electric field and the applied voltage drop from maximum at $r = r_0$ to zero at $r = r_0 + x_d$, i.e. $E(r_0 + x_d) = 0$ and $V(r_0 + x_d) = 0$ [114]. Integration from $r = r_0 + x_d$ to $r = r_0 + x$ of Eq. 4.6 gives the electric field in the SCR:

$$E(r) = \frac{eN_D}{3\epsilon \epsilon_0} \left[\frac{(r_0 + x_d)^3}{r^2} - r \right] = -\frac{d}{dr} \phi(r) \quad (4.7)$$

The relation between potential drop and width of the SCR is obtained by the second integration over the same interval:

$$V(r) = \frac{eN_D}{6\epsilon \epsilon_0} \left[-3(r_0 + x_d)^2 + \frac{2(r_0 + x_d)^3}{r} + r^2 \right] \quad (4.8)$$

As written in section 1.2 the effective voltage consists of the built-in potential of the contact, the applied voltage and the thermal voltage (kT/e). It is assumed that the voltage drop takes

³The full Laplace operator in spherical coordinates: $\Delta = \frac{1}{r^2} \frac{\partial}{\partial r} r^2 \frac{\partial}{\partial r} + \frac{1}{r^2 \sin \theta} \frac{\partial}{\partial \theta} \sin \theta \frac{\partial}{\partial \theta} + \frac{1}{r^2 \sin^2 \theta} \frac{\partial^2}{\partial \varphi^2}$.

place only over the SCR, i.e. for $r_0 \leq r \leq r_0 + x_d$. Therefore, Eq. 4.8 simplifies to:

$$\frac{6\epsilon\epsilon_0 V}{eN_D} = \frac{2}{r_0} x_d^3 + 3x_d^2 \quad (4.9)$$

This cubic function can be solved with the formula of Cardano [115]. For the limit of a planar interface (i.e. $r_0 \rightarrow \infty$) Eq. 4.9 transforms to Eq. 1.1.

In table 4.2 certain values are listed that can be calculated with the presented equations. In the first column the values for silicon with a resistivity of $1 \Omega \text{ cm}$ are given. This material is known to produce modulated shapes with strong kinks (cf. section 3.4.4) and has been optimized during a former doctoral thesis [26]. Analyzing the growth of strongly modulated pores revealed that a tiny pore with a radius r_0 of about 100 nm is formed in the beginning and widened afterwards to obtain the desired shape. This ratio $r_0/a = 0.05$ is taken as the basis for the calculations in table 4.2. In the second column the material with a lattice constant of 700 nm is presented. The corresponding radius of curvature with the same ratio $r_0/a = 0.05$ is then $r_0 = 35 \text{ nm}$. During the formation of the small pore the applied voltage was $V = 5 \text{ V}$ for $a = 2 \mu\text{m}$ and $V = 4 \text{ V}$ for $a = 700 \text{ nm}$. The width of the flat SCR $W_{\text{SCR}}^{\text{flat}}$ is calculated with Eq. 1.1. For the calculations, the voltage was corrected by the built-in potential of the silicon-electrolyte interface (0.5 V).

Under the assumption of a flat interface the critical field strength of electric breakdown E_{bd} corresponds to a breakdown voltage of $V_{\text{bd}}^{\text{flat}}$, dependent only on the doping density N_D . $V_{\text{bd}}^{\text{flat}}$ can be calculated from Eq. 4.7 with $r = r_0$ and $r_0 \rightarrow \infty$

$$E = \frac{eN_D}{\epsilon\epsilon_0} x_d \quad (4.10)$$

whereas $E = E_{\text{bd}}$ and x_d is replaced by the width of the SCR of a planar junction (Eq. 1.1):

$$V_{\text{bd}}^{\text{flat}} = \frac{E_{\text{bd}}^2 \epsilon\epsilon_0}{2eN_D} \quad (4.11)$$

The derivations presented above for a spherical junction introduce an additional dependence on the radius of curvature r_0 . For a spherically curved interface a significantly smaller width of the SCR $W_{\text{SCR}}^{\text{sphere}}$ is obtained. Therefore, the electric field strength increases and the breakdown conditions are reached at a considerably lower breakdown voltage $V_{\text{bd}}^{\text{sphere}}$.

In the case of the material with $2 \mu\text{m}$ lattice constant the formation of a small pore takes place at a voltage close to the breakdown voltage $V_{\text{bd}}^{\text{sphere}} = 5.29 \text{ V}$ of a spherical junction. This unstable regime close to the breakdown voltage lasts only for a short time (cf. section 3.4.4 and Fig. 3.7). With increasing pore diameter and decreasing voltage a stable pore growth is ensured again.

A pore with the same radius of curvature of $r_0 = 100 \text{ nm}$ etched in the 700 nm material would give a $V_{\text{bd}}^{\text{sphere}}$ of 3.98 V. The reason for the lower breakdown voltage is the higher doping density. However, this radius is too large for the purpose of strongly modulated pore shapes and has to be scaled-down to $r_0 = 35 \text{ nm}$ in the 700 nm material as mentioned above. Thus, the breakdown voltage is further reduced to $V_{\text{bd}}^{\text{sphere}} = 2.05 \text{ V}$ due to the changed geometry (cf. second column in table 4.2).

The width of the SCR is the important number which characterizes the field conditions during the formation of the pores. Especially the initial small pore in the beginning of a new modulation

	optimized material	material under consideration	$W_{\text{SCR}}^{\text{sphere}}/a = 0.258$ at $V = 4 \text{ V}$	$W_{\text{SCR}}^{\text{sphere}}/a = 0.258$ at $V \triangleq V_{\text{bd}}^{\text{sphere}}$
$a \text{ [nm]}$	2000	700	700	700
$N_{\text{D}} \text{ [cm}^{-3}\text{]}$	$5 \cdot 10^{15}$	$8 \cdot 10^{16}$	$3.2 \cdot 10^{16}$	$2 \cdot 10^{16}$
$\rho \text{ [}\Omega \text{ cm]}$	1	0.1	0.2	0.3
$E_{\text{bd}} \text{ [V/cm]}$	$3.6 \cdot 10^5$	$5.7 \cdot 10^5$	$4.8 \cdot 10^5$	$4.5 \cdot 10^5$
$V \text{ [V]}$	5	4	4	2.7
$W_{\text{SCR}}^{\text{flat}} \text{ [nm]}$	1088	240	380	380
$V_{\text{bd}}^{\text{flat}} \text{ [V]}$	86.9	13.5	23.9	32.5
$r_0 \text{ [nm]}$	100	35	35	35
r_0/a	0.05	0.05	0.05	0.05
$W_{\text{SCR}}^{\text{sphere}} \text{ [nm]}$	516	129	181	181
$W_{\text{SCR}}^{\text{sphere}}/a$	0.258	0.184	0.258	0.258
$V_{\text{bd}}^{\text{sphere}} \text{ [V]}$	5.29	2.05	2.14	2.20

Table 4.2: Table of factors that determine the electric conditions in the vicinity of the pore tip. The values for the discussed 700 nm lattice (second column) are compared to a material with 2 μm lattice constant (first column) which is known to possess perfectly-shaped pore modulations. In the last two columns values are calculated for an assumed material which has the same ratio $W_{\text{SCR}}^{\text{sphere}}/a$ like the 2 μm material with the same ratio r_0/a . The doping density N_{D} and the resistivity ρ are taken from Ref. [24]. For an applied voltage V the width of the SCR $W_{\text{SCR}}^{\text{flat}}$ is calculated with Eq. 1.1. The breakdown voltage $V_{\text{bd}}^{\text{flat}}$ for a planar interface is derived from Eq. 4.11. $W_{\text{SCR}}^{\text{sphere}}$ is the result of Eq. 4.9 and $V_{\text{bd}}^{\text{sphere}}$ the result of Eq. 4.8 for an x_{d} given by Eq. 4.7 for $E(r) = E_{\text{bd}}$.

is the crucial point for a strongly modulated pore shape. In the optimized material of 2 μm lattice constant the width of the spherical curved SCR is 0.258 in units of the lattice constant while it is only 0.184 for the 700 nm lattice. This means that in the latter case the expansion of the SCR into the material is reduced. For the given doping density $N_{\text{D}} = 8 \cdot 10^{16} \text{ cm}^{-3}$ a voltage of $V = 9.3 \text{ V}$ would be necessary to enlarge the SCR accordingly.

According to Eq. 4.9 the width of the SCR is dependent on the applied voltage and the doping density for a fixed radius of curvature. In the following it is assumed that a width of the SCR equal to the conditions in the 2 μm material would be an optimum for the pore growth. Therefore, in the last two columns of table 4.2 two different scenarios for the same ratio $W_{\text{SCR}}^{\text{sphere}}/a = 0.258$ as in the 2 μm lattice are discussed.

In the third column the voltage is set to $V = 4 \text{ V}$. Thus, the required doping density for the case

$W_{\text{SCR}}^{\text{sphere}}/a = 0.258$ is then calculated to $N_{\text{D}} = 3.2 \cdot 10^{16} \text{ cm}^{-3}$. Despite the reduced doping density the breakdown voltage $V_{\text{bd}}^{\text{sphere}}$ is still lower than the applied voltage. Thus it can be concluded that no smooth pore walls can be etched although the ratio $W_{\text{SCR}}^{\text{sphere}}/a$ equals that of the $2 \mu\text{m}$ sample. This confirms also that the major impact is due to the pore geometry and an appropriate adaption of the doping density of the material has only a minor influence on the breakdown voltage.

In the fourth column the doping density is determined for which the applied voltage V equals the breakdown voltage $V_{\text{bd}}^{\text{sphere}}$. The result is that the maximum voltage that can be applied still allowing stable pore growth is 2.7 V. The corresponding doping density necessary to fit the relation $W_{\text{SCR}}^{\text{sphere}}/a = 0.258$ is $N_{\text{D}} = 2 \cdot 10^{16} \text{ cm}^{-3}$. It should be mentioned once again, that the external applied voltage is reduced by the built-in potential of 0.5 V and thus the voltage applied to the interface has the same value as $V_{\text{bd}}^{\text{sphere}}$. This calculation determined an optimum value for the given problem. Namely, the problem was given as determined by the required form of the SCR $W_{\text{SCR}}^{\text{sphere}}/a = 0.258$ based on the findings for the $2 \mu\text{m}$ lattice. Then the doping density of the material was calculated under the condition, that the applied voltage V is maximized. Thereby, the maximum was defined by the breakdown voltage $V_{\text{bd}}^{\text{sphere}}$.

Although a further decrease of the doping density would raise the limit for electric breakdown, this is not a solution for the problem. In contrast to the pore tips, the walls resemble a cylindrical interface and thus its SCR width is between $W_{\text{SCR}}^{\text{flat}}$ and $W_{\text{SCR}}^{\text{sphere}}$. A lower doping density means an increased width of the SCR. If the overlap of the SCRs from adjacent pores is too large, the adaption to the pore tips is getting poor. Thus, single pores are prevented from being etched and the stable pore formation regime is left.

In conclusion of this section, the electric field conditions in the SCR are complex and have to be considered carefully. The available material with a doping density $N_{\text{D}} = 8 \cdot 10^{16} \text{ cm}^{-3}$ and a lattice constant of $a = 700 \text{ nm}$ can be used for the growth of straight and slightly diameter-modulated pores. For a strong modulation as necessary for the 3D photonic crystal structure presented in section 3.4.4 the application of the material is limited by a low breakdown threshold. The small pore that initializes the growth of a new modulation relies on a certain amount of charge carriers generated by breakdown processes [31]. But still, a sufficiently high voltage is required to adapt the SCR to the small pore tips. While this can be satisfied in the case of the material with a lattice constant of $2 \mu\text{m}$, for the higher doped 700 nm material the limit is exceeded due to the lower breakdown threshold. Furthermore it could be shown, that an adaption of the doping density can only slightly improve the conditions. The main impact comes from the geometry of the curved pore tip. Nevertheless, an adaption of the doping density to a value of $N_{\text{D}} = 2 \cdot 10^{16} \text{ cm}^{-3}$ would be an optimum for a lattice constant of 700 nm . This is a reduction of the doping density by a factor of four. This could improve the range of etchable pore diameters. Also the shape of strongly modulated pores should appear smoother since the amount of charge carriers generated by breakdown processes is reduced.

4.6 Photonic Stop Band at 1.5 μm Wavelength

With the hexagonal pore arrangement and the obtained shape of modulated structures presented so far a photonic crystal with a complete 3D photonic band gap cannot be realized (cf. section 3.4.4). However, the fabrication of structures that possess photonic stop bands in the mod-

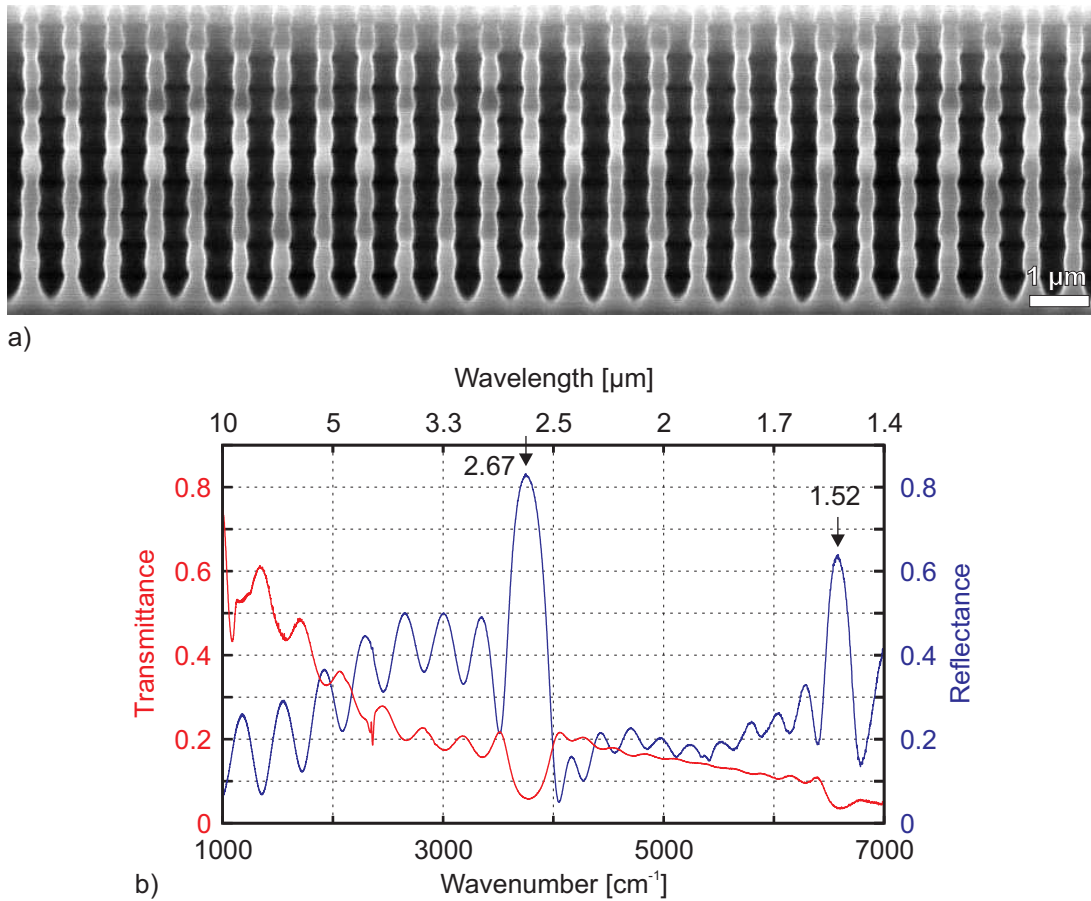


Figure 4.13: A photonic stop band at 1.5 μm wavelength. a) The cross section of the characterized sample with ten modulations (only nine are visible). b) The FT-IR spectrum measured in the direction of the etched pores. Two stop bands can be distinguished at 1.5 μm and 2.7 μm , respectively.

ulation direction is possible. To show this property, a sample with ten modulations was grown (Fig. 4.13a). Thereby, the modulation length was tuned to form a stop band around 1.5 μm wavelength (Fig. 4.13b). A second peak indicating another stop band is located around 2.7 μm . Additionally, also minor peaks between the stop band positions occur, especially when measured in reflection. These are Fabry-Perot resonances due to multiple reflections at the different interfaces of the photonic crystal and the remaining bulk silicon. A detailed discussion of these Fabry-Perot resonances is given in Ref. [111].

4.7 Summary

This chapter discussed the possibility to shrink the lattice constant of macroporous silicon to a range applicable for optical applications in the 1.55 μm wavelength region and the limitations involved in creating 3D structures. Straight pores could be etched with large aspect ratios and thus the realization of 2D photonic crystals is feasible. The observed disorder in pore diameter and length was proven to be caused by the lithographically defined mask. To circumvent this problem, the lithography has to be improved in its accuracy. The deviation of the etch pit positions and their diameter should vary within only a few ten nanometers which is feasible with today's masking

processes.

The etching of diameter-modulated structures was also presented. A homogeneous pore growth with a ratio of minimum to maximum diameter of 1 : 2 was realized. Furthermore, optical characterization of the samples emphasized the utilization of the obtained structures for photonic crystal applications.

In comparison to former works the structures with 700 nm lattice constant cannot yet compete with the lower doped material. There, diameter modulation ratios of 1 : 4 and even more are possible, as shown for instance in chapter 2 and section 3.4.4. Especially the strong modulation of the pore diameter is a limiting fact in the design of structures so far. Therefore, this chapter dealt intensively with the SCR model and the electric field conditions at the pore tip. The phenomenological observations were corroborated by calculations and a recommendation for a properly doped material was given. An optimized material with proper doping density and uniform mask will result in a higher homogeneity of the macroporous samples.

Nevertheless, physical limitations in the etching process become more and more dominant at this sub-micrometer size scale. Thus, a couple of other parameters have to be considered carefully as well. For instance, the composition of the etchant and especially the influence of type and concentration of the surfactant need further investigations. For reliable results the obvious limitations due to lithography and doping should be solved first.

Chapter 5

Photonic Crystals Beyond the Photonic Band Gap

The photonic band gap is an important feature of a photonic crystal. As shown in section 3.4 it can be used to design waveguides or to confine light and suppress spontaneous emission. However, a photonic band gap is not the only property of a photonic crystal. Based on its dispersion relation a couple of effects were proposed, suitable to affect the propagation of light. Therefore, it is necessary to calculate the complete dispersion relation and not only a path between points of high symmetry. In the beginning of this chapter the derivation and analysis of such an extended photonic band structure is shown for the example of a 2D photonic crystal. This formalism is then used to analyze a 3D modulated macroporous silicon sample. For such a sample the pore shape is derived from an as-etched sample and used for the band structure calculation. From the analysis of the dispersion relation the refraction behavior of the crystal will be discussed. Thereby, special emphasis is given to the fact that negative refraction is possible with the presented 3D macroporous silicon structure.

5.1 Introduction

The dispersion relation of a photon in free space is given by

$$\omega = ck \tag{5.1}$$

which relates the angular frequency $\omega = 2\pi\nu$ of the photon with its wave vector $k = 2\pi/\lambda$. The slope of this linear dependence is the speed of light c . In the presence of a periodic dielectric structure the dispersion relation is modified due to the light-matter interaction.

For the characterization of a photonic crystal in terms of a photonic band gap the dispersion relation is calculated along a path between high symmetry points in reciprocal space. This was done for instance in Fig. 3.6. There, the eigenvalue problem (cf. section 3.3) was solved for a 3D simple cubic crystal along a path of high symmetry points. The most pronounced changes in the dispersion relation are expected to happen in the vicinity of the edge of the BZ [116]. Therefore, this procedure is sufficient for the exact determination of size and position of photonic band gaps. In the case of dispersion-related refraction phenomena in photonic crystals, however,

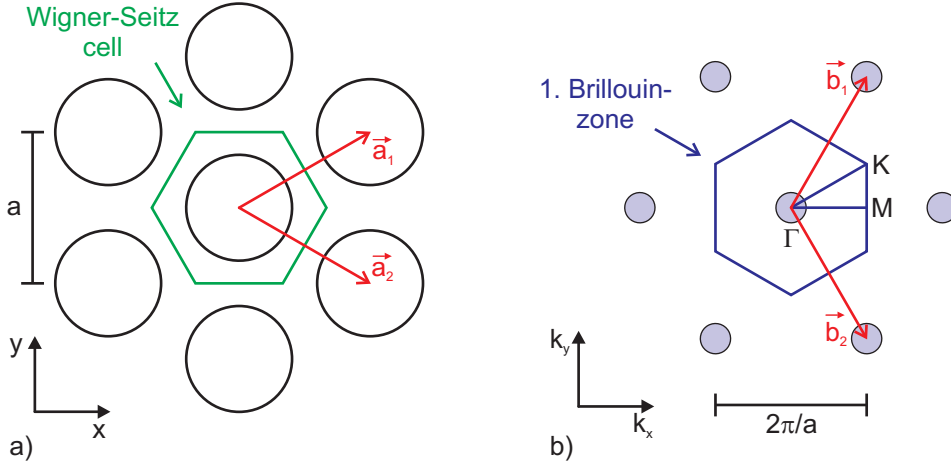


Figure 5.1: a) Depiction of the hexagonal lattice with lattice constant a , pore radius $r = 0.35a$, basis vectors \vec{a}_1 and \vec{a}_2 , and the Wigner-Seitz cell. b) For the reciprocal lattice with its basis vectors \vec{b}_1 and \vec{b}_2 and the lattice constant $2\pi/a$ the first Brillouin zone is inscribed and also the high-symmetry points $\Gamma = (0,0)$, $M = (0.5,0.5)$, and $K = (2/3, 1/3)$ in units of the reciprocal basis vectors.

this depiction is incomplete. For the study of beam propagation inside a photonic crystal the knowledge of the shape of the entire dispersion surface is necessary.

5.1.1 The Complete Dispersion Relation of a 2D Hexagonal Lattice

In the following the procedure is presented which is used to derive the dispersion surfaces of a given photonic crystal structure. For the sake of clarity a 2D hexagonal arrangement of air cylinders in a silicon matrix ($\epsilon = 11.7$) is taken as a model system.

The hexagonal lattice with a lattice constant a in real space (Fig. 5.1a) is described by the basis vectors \vec{a}_1 and \vec{a}_2 :

$$\vec{a}_1 = a \left(\frac{\sqrt{3}}{2}, \frac{1}{2} \right), \quad \vec{a}_2 = a \left(\frac{\sqrt{3}}{2}, -\frac{1}{2} \right)$$

For the calculation of the reciprocal lattice vectors a third unit vector $\vec{a}_3 = (0,0,1)$ perpendicular to \vec{a}_1 and \vec{a}_2 was chosen and therefore the volume results from $V = \vec{a}_1 \cdot (\vec{a}_2 \times \vec{a}_3) = -\frac{\sqrt{3}}{2}a^3$. The normalized reciprocal lattice vectors \vec{b}_1 and \vec{b}_2 then correspond to:

$$\vec{b}_1 = \frac{2\pi}{a} \left(\frac{1}{2}, \frac{\sqrt{3}}{2} \right), \quad \vec{b}_2 = \frac{2\pi}{a} \left(\frac{1}{2}, -\frac{\sqrt{3}}{2} \right)$$

In Fig. 5.1 a comparison between real space and reciprocal space is shown.

For the calculation of the complete dispersion relation the eigenvalue problem Eq. 3.13 has to be solved for the entire first BZ. Exploiting the symmetry of a hexagon only one twelfth of the area has to be calculated, e.g. a triangle circumscribed by the path along $\Gamma - M - K - \Gamma$. The obtained values are mirrored with $\Gamma - M$ as the mirror line and after that the whole segment is rotated by 60° angles until the cell is completely described. For the mirror translation and the rotation the matrices T_M and T_R were used, respectively:

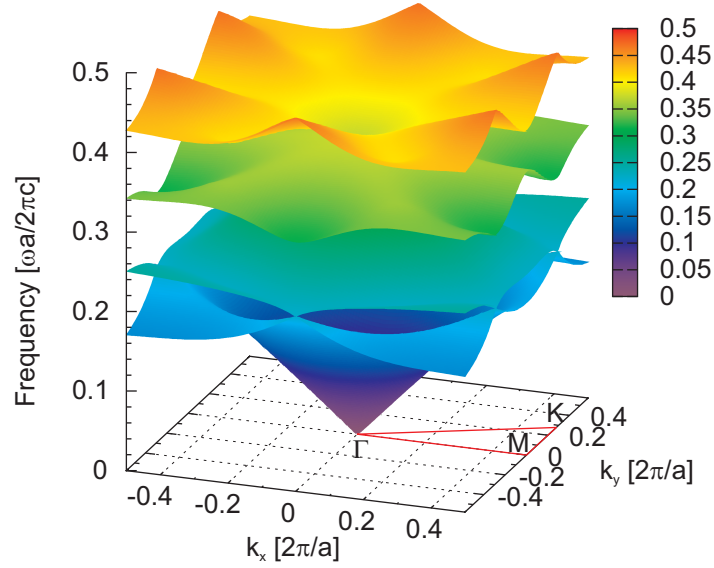


Figure 5.2: Depiction of the first four bands of the complete dispersion relation for the TM modes of a hexagonal lattice ($r = 0.35a$, $\varepsilon = 11.7$). Every band is represented by a closed dispersion surface. The frequency is color-coded and visible in the vertical dimension. Additionally, the points of high symmetry are projected onto the k_x - k_y plane. These are in units of k_x and k_y $\Gamma = (0,0)$, $M = (0.5, 0)$, and $K = (0.5, \frac{1}{2\sqrt{3}})$.

$$T_M = \begin{pmatrix} -1 & 0 \\ 0 & 1 \end{pmatrix}, \quad T_R = \begin{pmatrix} \frac{1}{2} & -\frac{\sqrt{3}}{2} \\ \frac{\sqrt{3}}{2} & \frac{1}{2} \end{pmatrix}$$

The usage of symmetry operations is important since it can diminish the computational time considerably.

About 2^{16} reciprocal lattice points (herein after called k -points) with equal distance to each other were taken for the description of the whole reciprocal lattice cell. For the visualization of these data three axes are required: two for the components of the wave vector $\vec{k} = (k_x, k_y)$ and one for the frequency. A mesh was calculated using the obtained k -points as supporting points (Fig. 5.2). The frequency is coded by the height of the mesh and additionally a color-coding was applied ranging from purple for low frequencies to red for high frequencies. For comparison, in Fig. 5.3 the photonic band structure for the same lattice is shown as a line plot along a path between the high symmetry points. The path is also plotted in Fig. 5.2 as a projection on the k_x - k_y plane.

5.1.2 Determination of Beam Propagation

With the help of such a dispersion surface plot the propagation direction inside the photonic crystal can be determined. An electromagnetic wave in free space has a frequency and a propagation direction. Thus it can be characterized by a wave vector \vec{k}_{free} . The dispersion surface of such a wave is given by its isotropic dispersion relation Eq. 5.1. It is represented by a sphere with radius \vec{k}_{free} . When hitting a material interface with a certain refractive index n the wave is refracted in accordance with the law of refraction. Thereby, two magnitudes are conserved: The wave vector component parallel to the interface k_{\parallel} and the energy.

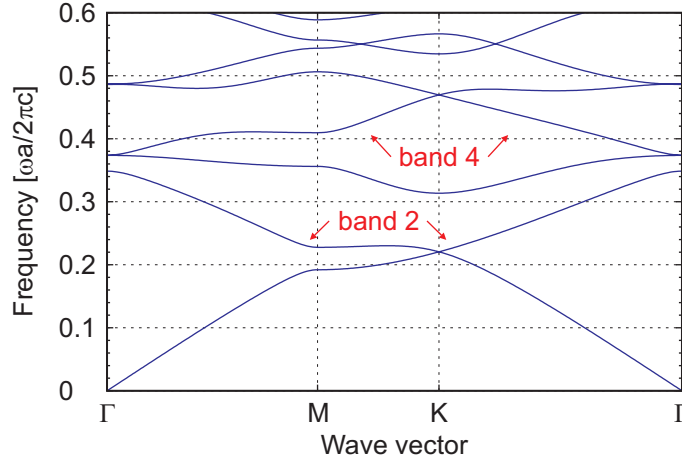


Figure 5.3: The photonic band structure depicted as a line plot along a path between the high symmetry points in the hexagonal lattice. Only the TM modes are shown. The pores have a diameter of $r = 0.35a$ in a silicon matrix with $\epsilon = 11.7$. For this pore radius no complete photonic band gap in 2D can be found (cf. Fig. 3.4 on page 32).

In the case of a photonic crystal, beam propagation inside the crystal is only possible if the wave from free space can couple to a Bloch wave in the photonic crystal. The Bloch waves are the solutions of the eigenvalue problem and are represented by a wave vector \vec{k}_{pc} inside the photonic crystal.

For the purpose of clarity, the second and the fourth band are depicted separately in Fig. 5.4 from the 3D plot above. The bands are looked at from the top. As a guide for the eye, additional contour lines were inserted into this surface plot. Along such a contour the height and thus the frequency is constant. It is called equi-frequency contour (EFC). The higher EFCs in the second band offer a circular shape while with decreasing frequency the form is altered to a more hexagonal shape. In the fourth band the bending is reversed. High frequencies are found around the K point and the EFCs change to a star-like shape with hexagonal symmetry.

In the scheme below the EFC plots the construction of the beam propagation inside the photonic crystal is shown for a frequency of $\omega a/2\pi c = 0.285$ and $\omega a/2\pi c = 0.410$, respectively. The incident wave is characterized by \vec{k}_{free} under an angle of 40° and 30° , respectively. The corresponding EFC is a red circle with radius \vec{k}_{free} . In free space, group velocity \vec{v}_g^{free} and phase velocity \vec{v}_{ph}^{free} are identical:

$$\vec{v}_g = \nabla_{\vec{k}} \omega(\vec{k}) \equiv \vec{v}_{ph} = \frac{\omega}{|\vec{k}|} \frac{\vec{k}}{|\vec{k}|} \quad (5.2)$$

The propagation direction is normal to the EFC and points in direction of increasing frequencies. Group velocity \vec{v}_g^{free} and wave vector \vec{k}_{free} are parallel to each other.

The energy conservation demands that the wave from free space can only couple to the corresponding photonic crystal EFC with the same frequency, denoted by the blue contours. Furthermore, the parallel component of the wave vector, $k_{||}$, has to be preserved. In this case the interface is along the $\Gamma - M$ direction and the perpendicular solid line denotes the magnitude of the parallel component $k_{||}$. The intersection of the construction line with the photonic crystal EFC marks the solution of the refraction problem. At this point the corresponding wave in the photonic crystal is excited, labeled with the wave vector \vec{k}_{pc} . Beam propagation inside the photonic crystal

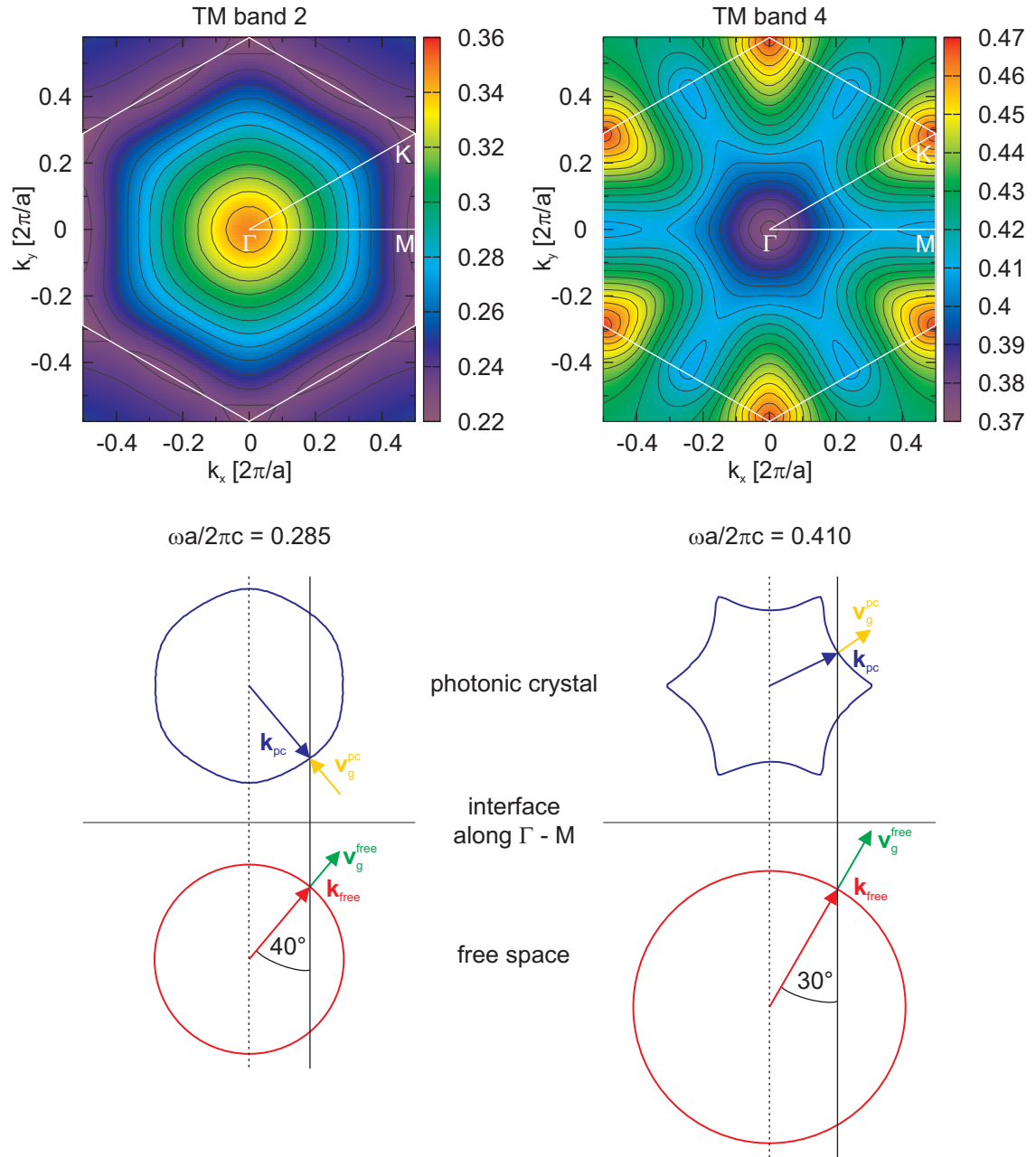


Figure 5.4: Color-coded 2D band structure plots of the second and fourth TM band with additional equi-frequency contours for certain values. In the second band the contour with the smallest diameter belongs to a frequency of $\omega a/2\pi c = 0.34$ and decreases with a decrement of 0.01 until $\omega a/2\pi c = 0.23$. The situation is inverted in the fourth band: The lowest frequency contour is found in the center ($\omega a/2\pi c = 0.375$) and the increment is 0.005 until the high frequency contour in the red area with $\omega a/2\pi c = 0.465$ at the K point. From these EFC plots the beam propagation inside the photonic crystal can be derived as shown in the scheme below the EFC plots. The incident wave from free space is defined by the wave vector \vec{k}_{free} and the group velocity \vec{v}_g^{free} . Under conservation of energy and parallel momentum the wave excites a Bloch wave inside the photonic crystal characterized by \vec{k}_{pc} and \vec{v}_g^{pc} .

is determined by the group velocity \vec{v}_g^{pc} which is again directed perpendicular to the EFC towards increasing frequencies.

From a geometrical point of view in all these considerations a second solution exists. Namely, there is a second intersection point of the construction line normal to the interface and the photonic crystal EFC. A solution at this point would give a wave traveling away from the interface in the direction of the incident beam. But such a wave has no physical meaning since it would imply an energy flow back to the source [117].

In this and also in the following EFC plots the group velocity vectors are not scaled accordingly. The accurate length of \vec{v}_g^{free} is equal to one in this dimensionless description. This would be a rather long arrow not suitable for presentation. The magnitude of the group velocities in the photonic crystal can be derived numerically as the differential coefficient of angular frequency and wave vector.

5.1.3 Selected Effects Related to the Dispersion Relation of Photonic Crystals

With this construction guide at hand for the beam propagation inside a photonic crystal, some effects related to the dispersion relation and discussed in literature should be mentioned shortly.

Superprism The superprism effect was one of the first effects observed in photonic crystals that is not relying on the existence of a photonic band gap [118]. The term ‘superprism’ was introduced in a paper of Kosaka et al. in 1998 [119]. It is defined as a large deflection of the refracted beam by only a slight change of the incidence angle. They measured a change in the propagation direction of up to 90° for a change of incidence angle of only 12° . Band structure calculations revealed, that a large anisotropy of the dispersion surfaces is responsible for this effect. Furthermore it was shown, that this effect is not only dependent on the incidence angle but also on slight changes in the incidence wavelength.

A comparable situation can be identified in the EFC plot in Fig. 5.4 for the frequency of $\omega a/2\pi c = 0.410$. If the incidence angle is diminished then the solid construction line moves to the left. Only slight changes in the incidence angle of \vec{k}_{free} are necessary to significantly change the direction of \vec{v}_g^{pc} due to the curvature of the EFC.

Self-Collimation In a nonlinear medium the diameter of a propagating pulse of high intensity can be reduced. This effect is called self-focusing and is dependent on an intensity-induced change of the refractive index. In photonic crystals a similar effect was observed [120]. However, in photonic crystals it is a linear effect not dependent on the intensity but on the curvature of the dispersion surfaces. In an area of the photonic band structure where the curvature of a dispersion surface is constant, the light which impinges under different angles propagates parallel inside the photonic crystal. An example for an EFC curved in such a manner can be found in the second band EFC plot in Fig. 5.4. The EFCs close to the boarder of the first BZ possess flat sections around the $\Gamma - M$ direction. Thus, beam propagation inside the photonic crystal does not change in its direction when changing the incidence angle. For slightly higher frequencies the EFCs become convex-shaped and so the beam is collimated.

Negative Refraction The refraction of light is described by the law of refraction published in the beginning of the 17th century by Snell. When light passes between two media with different refractive indices n_1 and n_2 , it changes its direction according to the equation

$$n_1 \sin \theta_1 = n_2 \sin \theta_2 \quad (5.3)$$

with θ_1 and θ_2 being the angles of incidence and refracted propagation, respectively. Assuming that one of the media has a negative index of refraction ($n < 0$), the light is refracted to the opposite direction of the surface normal compared to the case of positive refraction.

The field of negative refraction is strongly correlated with a material system called negative-index material (NIM) that has a negative index of refraction. Following the work of Veselago in 1968 [121], artificially created materials characterized by simultaneously negative permittivity ϵ and permeability μ would exhibit a negative index of refraction. With this negative index of refraction in NIMs, phase and group velocity vectors point to opposite directions leading to intriguing effects.

More than 30 years later Pendry proposed a flat lens that has no diffraction limit and is made of a NIM. The first experimental evidence of negative refraction in such a negative index material was shown in Ref. [122]. Later on, the sub-diffraction resolved imaging was proved, e.g. Refs. [123, 124, 125, 126] as well as the capability to render objects invisible [127, 128]. Another approach to negative index materials is based on purely dielectric materials with an anisotropy in the dielectric constant, e.g. Refs. [129, 130]. The disadvantage of NIMs is, however, a high absorption loss since they are operated at frequencies close to a resonant behavior for the electric as well as the magnetic fields [131].

Negative refraction in photonic crystals has already been realized prior to the publications in the field of NIMs. In the publication about the superprism effect by Kosaka et al. in 1998 the term negative refraction was already used [119]. While the phenomenological effect of negative refraction is the same – namely the refraction of the beam to the same side of the surface normal – the underlying physics is quite different. NIMs are treated within the effective medium approach. This means that the features used for the construction of NIMs are much smaller than the wavelength region of operation. In photonic crystals, the wavelength is comparable to the magnitude of the periodicity of the photonic crystal. The origin of negative refraction is the anisotropic shape of the EFC. A situation of negative refraction is represented in the EFC plot in Fig. 5.4 for the second band (left hand side): The group velocity vectors \vec{v}_g^{free} and \vec{v}_g^{pc} point to opposite sides of the surface normal. Thus, the refracted beam propagates on the same side of the surface normal with respect to the incident beam. For comparison, the depicted situation for the fourth band on the right hand side shows a positive refracted beam.

The situation discussed in band two of Fig. 5.4 represents a special case. For this particular frequency the EFC of free space and that of the photonic crystal are nearly equally shaped. However, in contrast to the free space EFC the corresponding photonic crystal EFC has an inward pointing group velocity vector. Thus, for all incident wave vectors \vec{k}_{free} the beam is refracted as if the photonic crystal would be a homogeneous medium with a refractive index equal to minus one.

In addition to the EFC plot used for the derivation of the beam propagation another method can

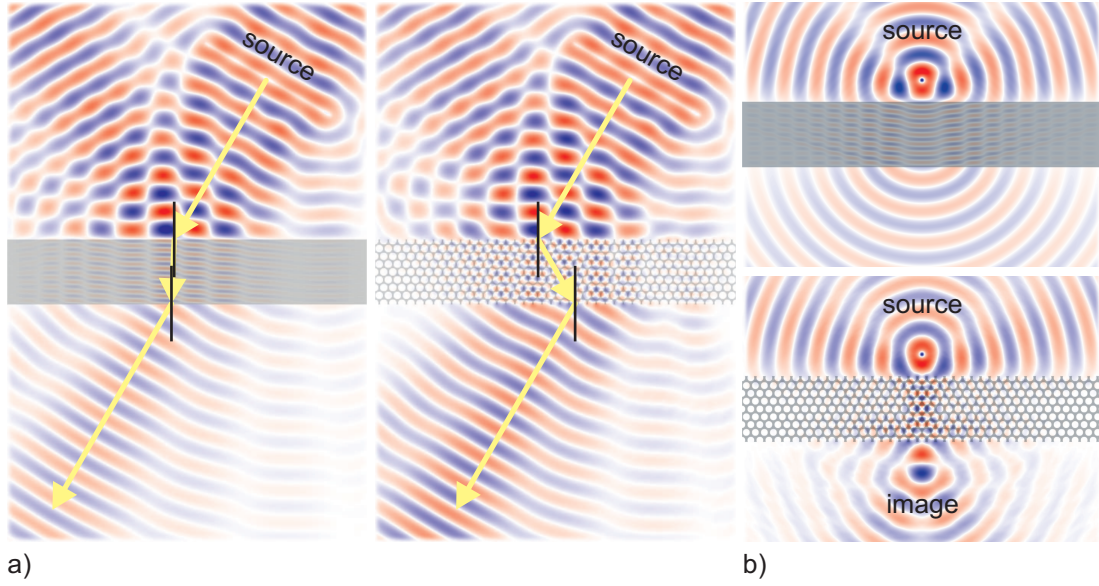


Figure 5.5: FDTD simulation in free space of the z-component of the electric field with a frequency of $\omega a/2\pi c = 0.285$. The field is represented by colors from blue for negative values, white for zero, and red for positive values of the electric field. The underlying gray area denotes a block of silicon ($\epsilon = 11.7$) and a 2D hexagonal photonic crystal structure, respectively. The field propagation from a finitely extended line source (a) and a point source (b) of the same frequency are compared between bulk silicon and photonic crystal. a) Negative refraction results in a beam refraction to the same side of the surface normal. b) Due to the negative refraction the photonic crystal can act as a lens with one focus point inside the crystal and a second just after the crystal.

be applied, too. Since the propagation of an electromagnetic wave obeys the Maxwell equations, it can be simulated for a given arrangement of dielectric material. A finite-difference time-domain (FDTD) algorithm was used to simulate the evolution of the electromagnetic fields in space and time [132]. The results are compared for a block of silicon and a photonic crystal made of silicon with a hexagonal pore arrangement as described above. In Fig. 5.5a the beam propagation from a finitely extended line source in the upper right corner is compared for these two silicon structures. In both cases the light is refracted firstly at the interface between free space to structure and secondly at the interface structure to free space. The dielectric constant of silicon is $\epsilon_{\text{si}} = 11.7$ and thus the beam is refracted according to Snell's law with a refractive index of $n_{\text{si}} = 3.42$. In the case of the photonic crystal the beam is refracted as if the material would have a refractive index of $n_{\text{pc}} = -1$. The beam is refracted negatively and propagates on the same side of the surface normal. For a second simulation the line source was replaced by a point source with a distance to the surface of the structure of 0.32 times the height of the structure. Due to the negative refraction in the photonic crystal the point source is imaged at the opposite side of the photonic crystal. Thus, the hexagonal pore array works as a flat lens [133, 134].

So far, the treatment of photonic crystal structures has been motivated by a short survey of selected effects related to the anisotropic nature of photonic crystal EFCs. They were explained on an ideal model system of a 2D hexagonal lattice of air cylinders in silicon. In contrast to self-collimation and superprism effect the negative refraction is a fundamental effect not relying on a change of the incident wave vector. In the following, the refraction properties of a 3D

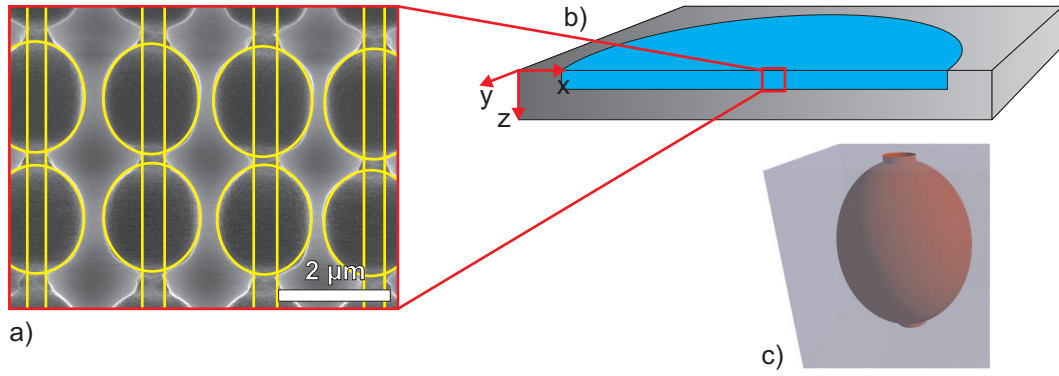


Figure 5.6: a) For the derivation of a model structure the cross section micrograph is analyzed. The pore geometry is described with ellipsoids and cylinders, whose parameters are derived from the yellow contours. b) In x- and y-direction the photonic crystal is defined by its mask while the z-direction is determined by the modulation. c) The unit cell can be described as simple tetragonal. It consists of a block of silicon with an ellipsoid and a cylinder inscribed.

macroporous silicon structure and in particular the negative refraction will be discussed more in detail. A review about refraction properties of photonic crystals in general can be found in Ref. [116].

5.2 ‘Real’ 3D Photonic Crystal Structure

Most approaches towards refraction properties of photonic crystals in literature are either purely theoretically or the experimental realizations try to mimic theoretical models as good as possible. In this work an alternative path is taken. Based on the analysis of etched 3D macroporous silicon samples, a model is derived that describes the pore morphology. With this model the dispersion relation is calculated and discussed. Thus, the refraction properties of an as-etched photonic crystal can be determined.

5.2.1 Derivation of the Model Structure

The origin of the following considerations is a strongly diameter-modulated macroporous silicon sample with a lattice constant of $a = 2\mu\text{m}$ (Fig. 5.6a). The definition of the coordinates is given in Fig. 5.6b: The x- and y-direction define the sample in the lateral direction, i.e. they are the lattice vector directions of the square lattice. Perpendicular to the plane defined by x and y is the etching direction of the pores, denoted as the z-direction.

Due to the quadratic lattice the lattice constant in x- and y-direction is identical: $a_x = a_y$. In the z-direction the lattice constant is defined by the length a_z of one modulation. In general, this quantity can be different from the lattice constants defined by the etch pits: $a_x = a_y \neq a_z$. Similar arguments hold true for the description of the pore morphology. While the shape is identical in x- and y-direction, it is stretched or compressed in z-direction.

For the calculation of the dispersion relation of such a structure the distribution of the dielectric constant has to be determined. In the present case the etched volume is described via an ellipsoid and a cylinder. The ellipsoid has the same diameter in x- and y-direction ($d_x = d_y$) and

is therefore rotational symmetric. An additional cylinder with radius r_{cyl} is introduced to make sure that the pores are connected to each other in the z-direction. This is necessary because a description of the pore shape by an ellipsoid only may lead to a different structure. For example, the ellipsoids with a diameter d_z in the z-direction touch each other but do not open a connection of a certain diameter between the modulations. To summarize this paragraph, the problem can be described as a simple tetragonal unit cell made of silicon with a rotationally symmetric ellipsoid and a cylinder of air inscribed (Fig. 5.6c). Thus, a model system for the derivation of the ε -distribution is obtained and can be used for the calculation of the corresponding dispersion relation.

5.2.2 Results of the Calculation

With the procedure described above an etched sample was characterized and its dispersion relation was calculated. From the analysis of the sample cross section the following values were obtained and used for the calculation: $a_x = a_y = 2\mu\text{m}$, $a_z = 2.1\mu\text{m}$, $d_x = d_y = 1.57\mu\text{m}$, $d_z = 1.75\mu\text{m}$, and $r_{\text{cyl}} = 0.18\mu\text{m}$. Exploiting the symmetries, the problem was reduced to one eighth of the simple tetragonal unit cell. The reciprocal lattice cell is also of simple tetragonal geometry with the lengths $k_x = k_y \neq k_z$ (Fig. 5.7a). In contrast to the depiction of a 2D dispersion relation, a 3D dispersion relation would need four dimensions: Three for the wave vector and one for the frequency. Without a loss of generality the analysis in the following is restricted to a plane in the reciprocal space defined by k_x and k_z with a fixed value of $k_y = 0$. With this restriction the analysis of the 3D crystal can be done similar to the presented case of a 2D lattice which allows for a clear presentation of the results.

In Fig. 5.7a the photonic band structure is presented as a line plot between points of high symmetry within the plane under consideration. In the $\Gamma - A$ direction band one and two and band three and four are degenerated. Around the L point and in the $\Gamma - X$ direction these bands split up. In Fig. 5.7b the EFCs of the fourth band are plotted. A rectangular geometry is clearly visible. In the z-direction the lattice constant is larger by a factor of 1.05 than the lattice constant in x- and y-direction. Because of this the reciprocal lattice vector component k_z is shortened by the same factor compared to k_x and k_y which can be verified by calculating the reciprocal lattice vectors. Thus, the side lengths of the plot also reproduce this ratio. To avoid confusion it should be highlighted that the size scale is determined only by the lattice constant $a_x = a_y = 2\mu\text{m}$ and not by a_z .

As emphasized in the introductory section of this chapter, the negative refraction is a fundamental effect. Thus, the following discussion of this phenomenon is well suited to analyze the beam propagation and the underlying physics from a theoretical point of view. Furthermore, the results of this discussion provide the base for the experimental determination of the refractive properties of the structure under consideration.

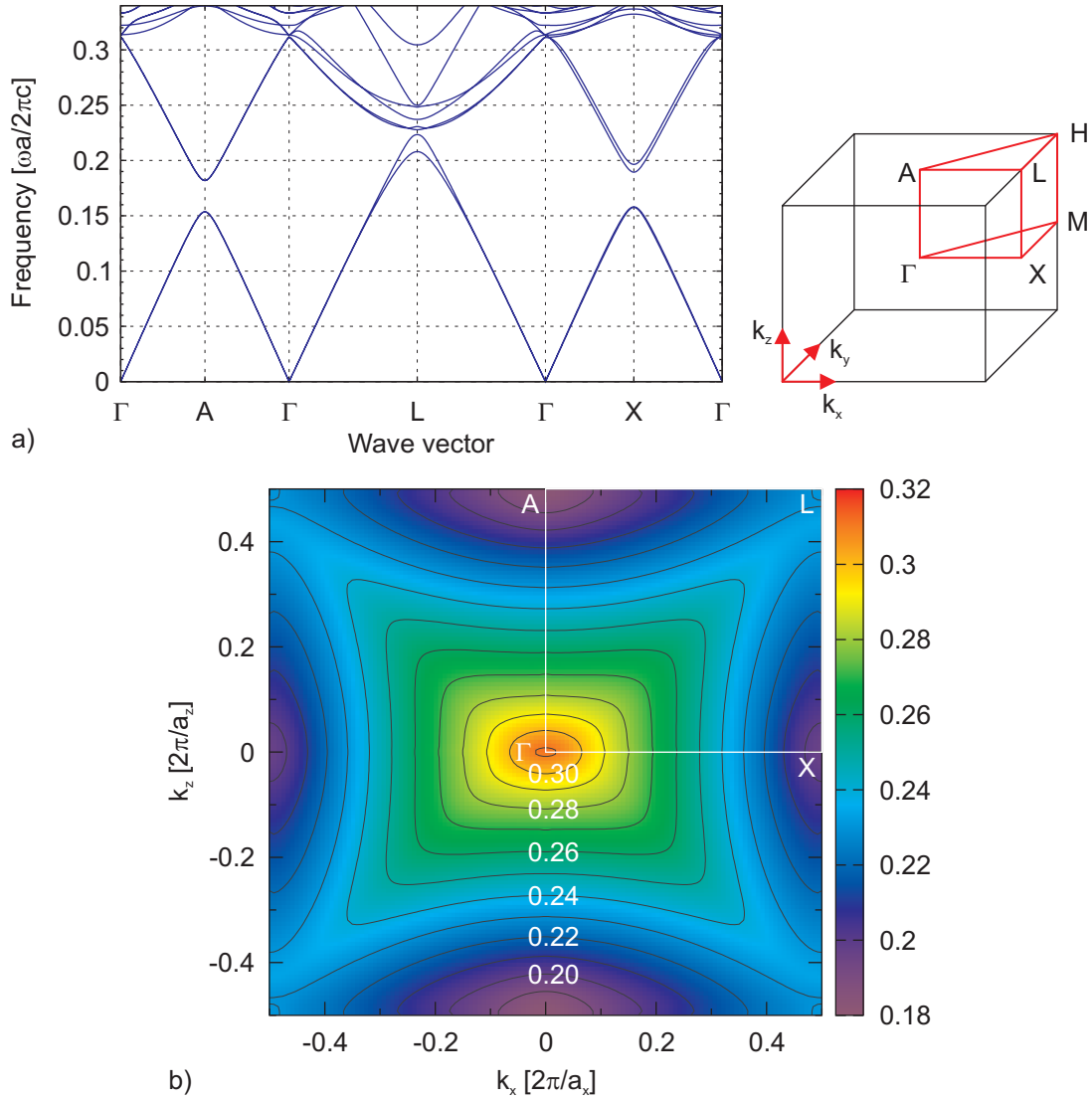


Figure 5.7: Results of the photonic band structure calculations restricted to the k_x - k_z plane at $k_y = 0$. The dielectric constant of silicon used for the calculation is $\epsilon_{si} = 11.7$ which corresponds to wavelengths in the mid-infrared region of the electromagnetic spectrum. The dielectric constant of the background equals one. a) Depiction of a line plot between points of high symmetry within the considered plane. Additionally, the reciprocal lattice is shown which is also of simple tetragonal symmetry with $k_x = k_y \neq k_z$. b) As an example, the dispersion relation of the fourth band is plotted including the EFCs and the symmetry points Γ , X, L, and A.

5.3 Discussion

Exemplarily, the fourth band is discussed more in detail.¹ Due to the restriction to the k_x - k_z plane at $k_y = 0$ the EFC plots can be interpreted in the same way as presented in the introduction of this chapter. In Fig. 5.8 two different situations are compared to each other. The incident wave can be thought of coming from the bottom in this representation. It hits the photonic crystal surface which is along the $\Gamma - X$ direction. On the left hand side the wave incidents under a fixed angle of 30° measured from the surface normal. The beam propagation for two different frequencies is shown. For the frequency $\omega a/2\pi c = 0.26$ the beam is refracted under an angle of 3° . In a material with isotropic dispersion this value would correspond to a refractive index of $n = 9.55$. For higher frequencies the EFCs of the fourth band are getting smaller in diameter. Furthermore, their shape is all-convex. Waves coupling to these EFCs are refracted negatively. In this particular case for a frequency of $\omega a/2\pi c = 0.28$ the refraction angle is -63° and would correspond to a refractive index of $n = -0.56$.

It has to be stressed that in the case of a photonic crystal it is distinguished between a group and phase refractive index [117]. The values of the refractive indices given here represent an effective refractive index of the photonic crystal as the beam would possess in accordance with the law of refraction (Eq. 5.3). However, these effective indices determine only the direction of the group velocity \vec{v}_g^{pc} . The magnitude of the group velocity, however, cannot be defined with this effective index since this would give velocities larger than the speed of light [135].

On the right hand side in Fig. 5.8 the incidence angle is changed instead of the frequency. For small incidence angles the incident beam at $\omega a/2\pi c = 0.27$ encounters a nearly flat EFC. Thus, the beam is refracted in direction of the surface normal. For larger incidence angles the refraction is caused by the strongly convex-shaped part of the EFC. The beam is refracted negatively again with an effective refractive index of $n = -0.94$.

Both scenarios in Fig. 5.8 show – dependent on the parameters of the incident wave – a change from positive to negative refraction. In the fixed angle case an increase of 7.7% for the frequency yields a change in the refraction angle of 65° . For the superprism effect as mentioned in the introductory section 5.1.3 a large beam deflection should be based on a small change in the incidence angle. This behavior can be found preferentially in areas where the EFC is strongly curved. For instance, the fixed frequency case for an incidence angle of 40° in Fig. 5.8 shows such a behavior. Slight variations around this 40° angle result in a significant deflection of the refracted beam. A change by only 6° from 40° to 46° in the incidence angle changes the refracted beam angle from -43° to the theoretical maximum of -90° . In the opposite direction – namely at an incidence angle of 34° – the refracted beam propagates under an angle of -17° . Hence, a change of the incidence angle by only 12° results in a change of the beam propagation direction in the photonic crystal of 73° . Thus, a high sensitivity of the propagating beam with respect to the incidence angle is obtained.

In contrast, the self-collimation within the analyzed 3D photonic crystal can be realized in sections with a flat EFC. Especially the frequency of $\omega a/2\pi c = 0.27$ offers this potential. For incidence angles of $\pm 23^\circ$ around the surface normal the refracted beams inside the photonic crystal would propagate parallel to each other. As can be seen on the left hand side in Fig. 5.8 for

¹The bands one to three and five to seven are depicted in a separate figure at the end of this chapter.

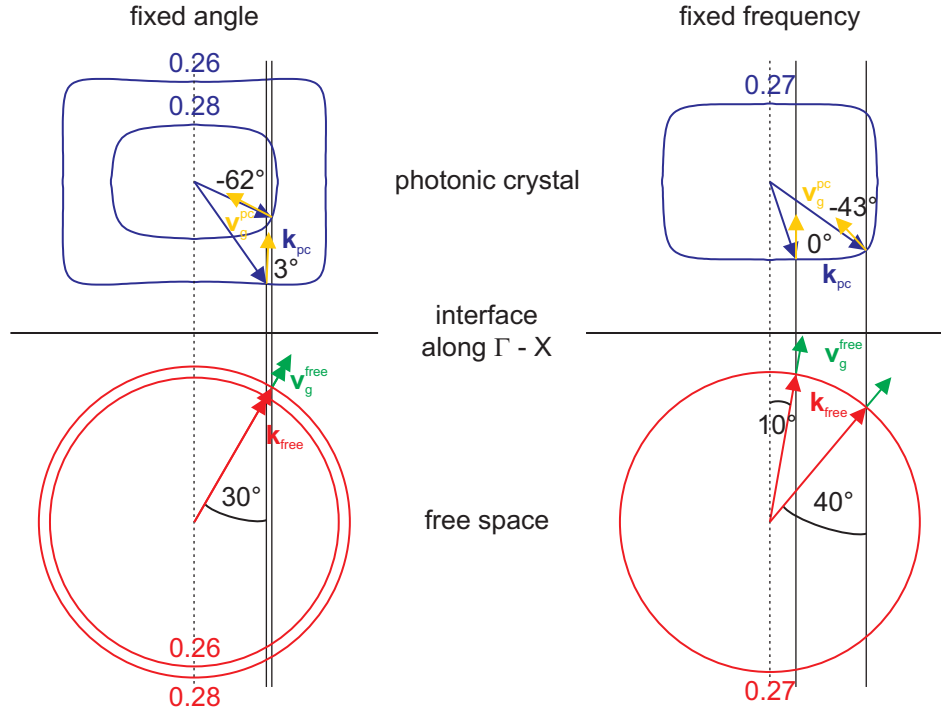


Figure 5.8: Construction of the beam propagation inside the photonic crystal for selected wave vectors \vec{k}_{free} (red arrows) within the fourth band (cf. Fig. 5.7). The group velocity is given by the green arrows. In the photonic crystal the wave vectors are marked by blue arrows and the beam propagation direction by dark yellow arrows. On the left hand side the construction for two different frequencies ($\omega a/2\pi c = 0.26$ and $\omega a/2\pi c = 0.28$) for an incidence angle of 30° is shown. While for the lower frequency the beam is refracted positively under an angle of 3° , for the higher frequency the beam is refracted negatively by -62° . On the right hand side the incidence angle is varied for a fixed frequency of $\omega a/2\pi c = 0.27$. For 10° incidence angle the refracted beam propagates nearly perpendicular to the interface while for 40° incidence angle negative refraction occurs under an angle of -43° .

higher frequencies a focusing would take place due to the convex-shaped EFCs whereas to lower frequencies the EFCs become concave-shaped. A practical application of this effect would be a frequency-dependent dispersion compensator.

Another consequence for the beam propagation is shown in Fig. 5.8 as well. For higher frequencies and larger incidence angles, respectively, the construction of the beam propagation as described above gives no intersection point of the EFC with the construction line. The reason for this is that the conservation of the parallel component of the wave vector is not fulfilled anymore. For instance, in the case of $\omega a/2\pi c = 0.27$ no intersection of the black construction line with the corresponding EFC can be found for angles larger than 46° . This means that the incident wave cannot couple to the crystal and total reflection occurs.

Wave Vectors, Velocities, and Handedness In general, a wave package has three different velocities: Phase velocity \vec{v}_{ph} , group velocity \vec{v}_{g} , and energy velocity \vec{v}_{e} . The group velocity describes the propagation velocity of a wave package while the energy velocity describes the propagation of the electromagnetic energy of the wave which is described by the Poynting vector \vec{S} . In the case of an infinite photonic crystal it has been shown that group and energy velocity are

equal to each other [74].

The direction of the phase velocity \vec{v}_{ph}^{pc} inside a photonic crystal is given by the wave vector \vec{k}_{pc} of the Bloch wave. In an isotropic lossless material with a dielectric constant independent of the frequency, group and phase velocity are equal (cf. equation 5.2). Thus, also the Poynting vector and the wave vector are parallel to each other and form a right-handed system. In a photonic crystal group and phase velocity are not necessarily parallel to each other. Thereby, the handedness is defined by the scalar product of phase and group velocity which is equivalent to the scalar product of wave vector and Poynting vector [135]. In the refraction cases presented above (Fig. 5.8) this scalar product is always less than zero. Hence, a left-handed system is formed which means that the electromagnetic fields \vec{E} and \vec{H} and the wave vector \vec{k}_{pc} form a left-handed triplet. Remarkably, the considerations above revealed that the left-handedness does not necessarily imply negative refraction. Despite the left-handedness positive beam refraction is possible, too.

The analysis of the directions of group and phase velocity and Poynting vector and wave vector, respectively, is essential for theoretical discussions. Since the seminal paper by Pendry (Ref. [136]) a lot of discussion regarding the negative refraction started. In the case of a NIM negative values of ϵ and μ for the same frequencies define a left-handed system. It was proven that this implies a negative index of refraction for these frequencies [137]. But things are different in the case of a photonic crystal. As shown above, a left-handed photonic crystal is not purely negatively refracting. Contrarily, also right-handed photonic crystals were shown to be able to refract light negatively [133]. The difference is that the above presented left-handedness in a photonic crystal has its origin in the dispersion relation. In contrast to the NIMs the material itself has neither a negative ϵ nor μ . Therefore, left-handedness in photonic crystals can – but does not have to – lead to negative refraction of the propagating beam. In Ref. [138] all possible refraction and handedness cases are discussed in a 2D square lattice photonic crystal.

Another conclusion from the left-handedness can be drawn: The phase of the wave moves in a direction opposite to the group velocity and therefore the energy of the wave. This implies that the peak of a wave package has to appear at the back side of a left-handed material before the wave enters the material at the front side. Such a backward wave gave rise to many discussions whether negative refraction is possible at all and whether the principle of causality is preserved (e.g. Refs. [139, 140] and the according comments and replies). In Ref. [141] the wave evolution at the interface between free space and negative refracting photonic crystal was analyzed with FDTD simulations. It was shown that the wave is trapped at the interface for a certain time until it propagates eventually in the negative direction in the photonic crystal.

Sub-wavelength Imaging Another term that is often associated with negative refraction and therefore should be noted here shortly is imaging without resolution restrictions. This feature was first proposed in Ref. [136]. With a conventional lens imaging is limited by diffraction and thus dependent on the wavelength. A material with dielectric and magnetic constant identical to minus one – namely a NIM – can circumvent this limitation. This effect is based on the amplification of the exponentially decaying evanescent waves from an object close to the flat surface of a slab of a NIM. Together with the propagating waves they can be used to form an identical image of the object behind the NIM.

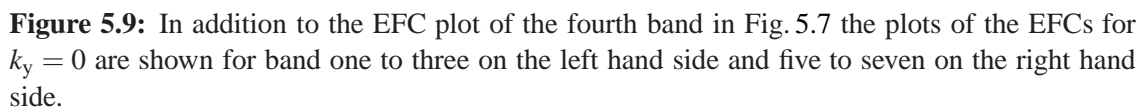
In contrast, photonic crystals cannot be described by an effective medium approach as it is the

case for the NIMs. Rather, they are characterized by their dispersion relation. In a very detailed analysis Luo et al. [142] could show that the necessary amplification of evanescent waves can be achieved in photonic crystals, too. However, the demands on structural perfection and low material absorption are very high.

However, in the present case the negative refraction will be used to characterize the manufactured macroporous silicon samples in terms of their refraction behavior.

5.4 Summary

Beyond the photonic band gap other effects related to the dispersion relation of a photonic crystal exist. To demonstrate this the complete photonic band structure was calculated and analyzed for a 3D macroporous silicon sample. In contrast to many theoretical publications the method presented here is based on the shape of an as-etched structure and thus a more realistic scenario is created. The analysis of the wave propagation revealed the possibility to use the photonic crystal to refract light negatively. The dependence of this effect on the incidence parameters wavelength and angle was analyzed in more detail. Thereby, especially the influence of the third dimension, i.e. the modulated pore diameter in the etching direction was considered as represented by the wave vector component k_z . The restriction to a plane in the reciprocal lattice with $k_y = 0$ has been done for the sake of clarity and to reflect the experimental conditions discussed in the next chapter. However, the presented discussion and arguments are of general meaning and can be applied to other k -values and dispersion-related effects as well.



Chapter 6

Experimental Characterization of the Refraction Properties

In this chapter the theoretical findings of the preceding chapter shall be experimentally tested and confirmed. It was shown that the 3D macroporous silicon sample under consideration features some interesting effects like self-collimation and the superprism effect. Both effects were shown to rely on a negative beam refraction in the investigated frequency range. The experimental verification of this phenomenon will reflect the discussed dependencies of the beam refraction on the parameters wavelength and incidence angle. Thus, the refraction properties of the photonic crystal are experimentally characterized and will be discussed and compared to theory.

6.1 Introduction

Similar to the realization of the first photonic band gap crystals (cf. section 3.4) the first experimental proof of negative refraction in photonic crystals was achieved in the microwave region of the electromagnetic spectrum. Alumina rods arranged in a square symmetry were used to show the beam shift induced by the negative refraction [143] and the imaging properties of a flat lens [144]. The concept was scaled towards the telecommunication wavelength of $1.55\text{ }\mu\text{m}$ where negative refraction was shown in a 2D hexagonal photonic crystal made of a III-V material [145]. Furthermore, the self-collimation and superprism phenomena were shown experimentally [146, 119].

For the experimental proof of the refraction properties of a photonic crystal device the electromagnetic wave in front of and after the photonic crystal has to be characterized. In the microwave region this task is comparatively easier due to the scaling of the structures. There, the self-collimated beam profile could be even measured inside a 3D crystal structure by mapping it with an antenna [147]. For 2D crystals the light refracted out of the plane can be used to map the beam propagation [148]. Additionally to the field amplitude also the phase information has been measured and thus the shape of the EFCs was determined [149].

For a 3D photonic crystals made of macroporous silicon as discussed here these methods are not suitable. The fields cannot be measured with a probe in the near-field region because in a 3D crystal wave propagation takes place deep inside the structure. The antenna approach is also not practicable since the considered 3D crystal is not accessible from all sides and furthermore it

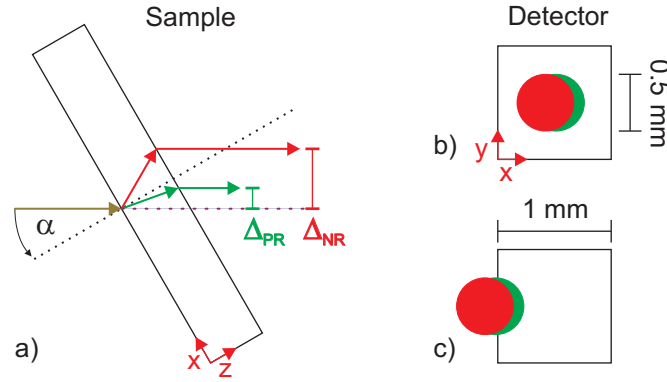


Figure 6.1: Measurement idea of the experimental setup. a) Due to the dispersion properties of the photonic crystal a beam shift is induced in transmission. The incidence angle α is positively defined. For illustration, the beam propagation for two different frequencies is shown. The green beam experiences positive refraction, the red one negative refraction. The corresponding beam shifts are Δ_{PR} and Δ_{NR} , respectively. Line of vision is the rotation axis (y-direction). b) Reference measurement with the beam aligned to the center of the detector area. The detector has an edge length of one millimeter while the beam spot is approximately half a millimeter in diameter. c) In a second measurement the beam is aligned to the detector edge and thus its intensity is sensitive to the beam shift. The line of vision in b) and c) is in direction of the beam (z-direction).

would require a probe of only a few ten to hundred nanometers for the field mapping inside the structure. Therefore, a different approach is taken here. As it was analyzed in the last chapter the beam refraction inside the crystal is dependent on the frequency and the angle of the incident beam. After crossing the photonic crystal layer the beam is refracted again and propagates parallel to the incident beam. This behavior can be seen in the simulated beam propagation in Fig. 5.5 on page 66 and also in Fig. 6.1a. Thereby, the refraction inside the photonic crystal is stored in the beam shift between incident and outgoing beam. The measurement of this beam shift is necessary to characterize the refraction properties. Therefore, the demands on an experimental setup are an angular- and frequency-resolved measurement of the beam shift caused by the photonic crystal.

6.2 Experimental Setup

The FT-IR spectrometer described in section 3.5 is used for the optical characterization of the photonic crystal. The sample is mounted on a rotation stage with the x-y plane perpendicular to the beam while the z-direction is equal to the beam direction. The y-direction of the sample is the rotation axis. Therefore, the incidence angle can be varied within the x-z plane by rotating the sample which is in accordance with the analytical treatment in the last chapter.

The additionally required frequency dependence in the measurement is an inherent property of the FT-IR. A broad range of frequencies in the infrared is transmitted simultaneously through the sample. However, the detection is not position sensitive. Therefore, the beam shift induced by the photonic crystal is translated in an intensity change at the place of the detector. This is schematically described in Fig. 6.1: In a) the beam shift for two different frequencies under an incidence angle of α is shown. The positively refracted green beam has a comparatively

lower shift than the negatively refracted red beam. b) At the detector the intensity of the spot is measured. Due to the beam shift the spot moves – dependent on the frequency – over the detector area. Since the detector area is twice as large in diameter as the beam spot, the whole spot intensity is measured, even if the beam is shifted. In c) the measurement is repeated but with an intentionally ‘misaligned’ beam. In fact, the last mirror prior to the detector is adjusted in a way that the unshifted beam (normal incidence) is aligned to the detector edge. This could be verified by an intensity measurement: At half intensity only half of the beam spot area is detected. An important point to consider here is that the beam is only moved in the x-direction. In contrast to the measurement in b) the change of the beam position is now correlated with an intensity change. The second measurement in c) divided by the spectrum obtained from the measurement in b) then gives an intensity ratio and therefore a measure of the beam shift.

During the measurements the sample chamber was flushed with gaseous nitrogen. An additional idle time of 30 minutes was introduced after the chamber was opened to establish a nitrogen atmosphere and remove absorbing species like hydrogen. In this way a stable background is defined which is important if different frequency spectra should be compared to each other.

The reproducibility of the angle adjustment of the motorized rotation stage was also checked. Therefore, a spectrum was taken at a certain angle. A second spectrum was taken after the stage was rotated to a different angle and back to the original angle. By comparison of the two measured spectra an error of less than one percent for the setting of the angle was obtained. Thus, a stable setup for comparing the frequency and angle of different spectra to each other is achieved suitable for the measurements presented in the following section.

6.3 Results and Discussions

The sample which was considered theoretically in the preceding chapter consisted of a photonic crystal layer with a thickness of $23\ \mu\text{m}$ according to eleven modulations in the z-direction. After the sample was fabricated the bulk silicon from the back side was thinned. A layer of $192\ \mu\text{m}$ in thickness remained for reasons of stability. The diameter of this circular back side-etched area is eleven millimeter and defines the lateral extension of the photonic crystal in the x-y plane. Due to the remaining silicon an additional beam shift caused by the silicon is induced. For a given incidence angle, however, this beam shift is constant and independent of the frequency as will be proven later on in this section.

All measurements consist of 128 scans with a spectral resolution of $2\ \text{cm}^{-1}$. The aperture stop (cf. Fig 3.5) set the beam waist to $0.5\ \text{mm}$. At first, the spectrum taken for normal incidence is discussed (Fig. 6.2). The most conspicuous thing is the stop band located between $750\ \text{cm}^{-1}$ and $980\ \text{cm}^{-1}$. Thereby, the lower limit coincides with the band gap of the MCT detector which can be seen in the gray background signal. Hence, its position has a high measurement uncertainty and is not further considered. The upper limit corresponds to a wavelength of $10.2\ \mu\text{m}$. The position of this stop band is compared to the calculated band structure in Fig. 5.7a. The measurement normal to the surface is equal to the $\Gamma - A$ direction. From the calculation a stop band can be seen between the normalized frequencies $\omega a/2\pi c = 0.15$ and $\omega a/2\pi c = 0.18$. The experimentally observed upper limit of the stop band corresponds to a normalized frequency of $\omega a/2\pi c = 0.2$. Thereby, the wavenumber $\tilde{\nu}$ is related to the normalized frequency $\omega a/2\pi c$ via the lattice constant a which

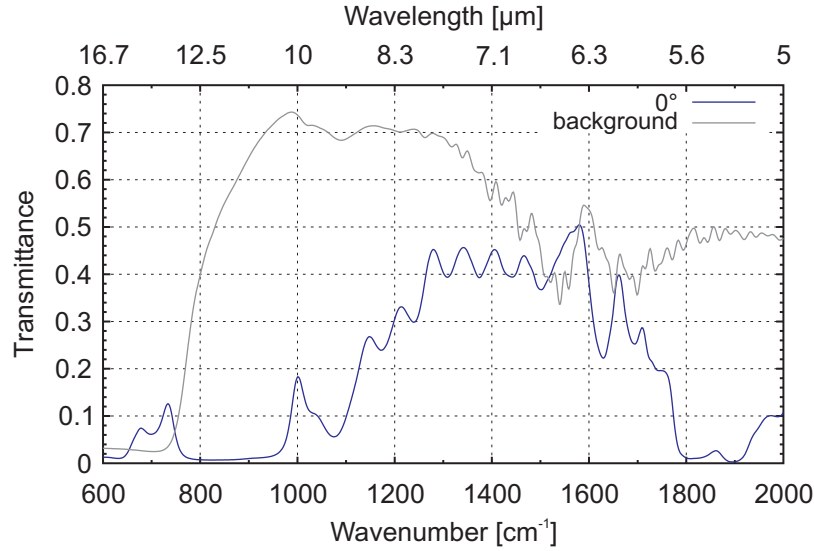


Figure 6.2: FT-IR spectrum of the sample under consideration measured under normal incidence, i.e. in z-direction. Additionally, the background spectrum is shown which reveals that wavenumbers below 800 cm^{-1} cannot be taken into account due to the band gap of the detector.

is $2 \mu\text{m}$ for the discussed sample:

$$\tilde{\nu}a = \omega a / 2\pi c \quad (6.1)$$

Thus, a shift towards higher frequencies can be expected from the experimental data in comparison with the theoretical predictions. The origin of such a systematic error is discussed later on in this section.

The theoretically discussed fourth band lies within a frequency range between $\omega a / 2\pi c = 0.18$ and $\omega a / 2\pi c = 0.32$. This corresponds to wavenumbers of 900 cm^{-1} and 1600 cm^{-1} , respectively. The transmission for the higher wavenumbers within this band oscillates around 40% which means that a considerably large part is transmitted within this range of frequencies. Hence it can be concluded, that the coupling – at least for these wave vectors – is strong and the homogeneity of the photonic crystal is sufficient to not loose the largest amount of transmitted intensity in scattering processes. Subsequent to the frequencies corresponding to the fourth band a decrease in transmittance can be seen in the spectrum. The analysis of the beam propagation in this frequency range would involve many bands and several refracted beams would occur for a single frequency.

Below, measurements are analyzed for the two cases considered theoretically in the last chapter, namely the fixed angle and the fixed frequency scenario. The range of applicable angles in the fixed frequency case is restricted to $\pm 60^\circ$ for mainly two reasons: First, the measurement method is limited to an overall beam shift of $\pm 250 \mu\text{m}$ coming from the relation between the diameter of the beam spot and the detector size (cf. Fig. 6.1). Second, for incidence angles larger than 60° an increased transmittance was detected coming from the outer parts of the beam that potentially bypassed the sample.

Constant Angle In Fig. 6.3 the intensity ratio over the wavenumber is plotted for an incidence angle of 30° and -30° . For an unshifted beam an intensity ratio of 0.5 would be expected because

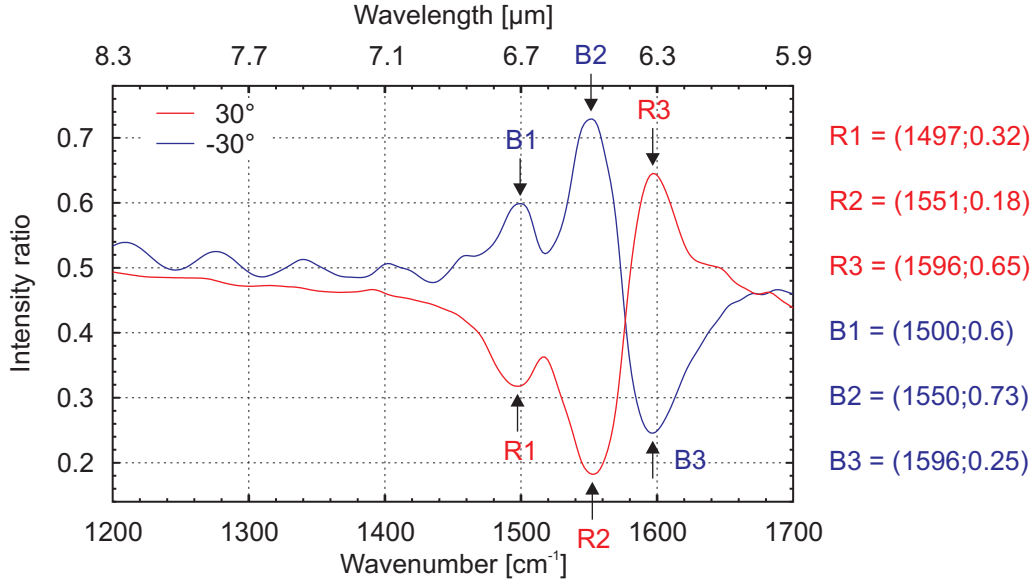


Figure 6.3: The intensity ratio between half spot and full spot alignment for a fixed detector alignment and an incidence angle of 30° (red curve) and -30° (blue curve). The peaks are named and the according coordinates are given beside the plot.

the beam detected at the detector edge has half the intensity of the reference beam. The red curve for the 30° angle shows a decrease in the intensity ratio towards the two minimum peaks R1 and R2. The corresponding detector alignment and the definition of the incidence angle α used for this measurement are given in Fig. 6.1a and c, respectively. From that it can be expected that for positively defined incidence angles the beam is shifted out of the detector field (i.e. in this case over the left edge of the detector) if the effective refractive index is negative or positive with a value larger than one. In this way the intensity ratio is decreased which is reproduced by the measurement. A reference measurement was taken for the opposite angle of -30° (blue curve) without changing the alignment between beam spot and detector. As expected, the curve shows a reversed shape which means that the beam is shifted towards the center of the detector area leading to the maxima B1 and B2. In both curves the shifting behavior is reversed after the second peak, which gives the peaks R3 and B3.

Qualitatively, the shape of the curve can be described in accordance with the beam construction plot in Fig. 5.8 on page 71 and the EFC plot in Fig. 5.7 on page 69. For lower frequencies the EFCs are concave-shaped and the effective refractive index n_{eff} is close to one. For higher frequencies, e.g. the discussed frequency of $\omega a/2\pi c = 0.26$, the beam is still refracted positively but nearly perpendicular to the surface. Thus, n_{eff} increases towards higher frequencies and the beam starts to shift out of the detector field. For even higher frequencies n_{eff} goes to infinity and changes its sign. Negative refraction occurs and leads to a large beam shift until the conservation of k_{\parallel} is not fulfilled anymore. The maximum beam shift corresponds to the second peak R2 (B2) in the spectrum shown in Fig. 6.3. From the theoretical considerations of the fourth band no coupling is possible for wavenumbers larger than the position of the peak R2 (B2). Contrarily, the experiment shows an increase (red curve) in the intensity ratio which means that light is transmitted and shifted back to the middle of the detector field (peak R3) or vice versa for the blue curve (peak B3). For the explanation of this behavior the coupling to higher bands has to be considered

as well. From the plot of the bands one to seven in Fig. 5.9 it can be seen that there is a certain frequency overlap of the fourth band with other bands. Analyzing the beam propagation direction for frequencies larger than $\omega a/2\pi c = 0.28$ revealed, that the seventh band causes beam refraction in an opposite direction as the fourth band. However, for a complete discussion of the origin of the peaks R3 and B3, even higher bands have to be considered and since several bands could contribute to the refraction also the couple efficiencies have to be determined. In here, the analysis should be restricted to lower bands which are more favorable for dispersion-related photonic crystal applications.

From the derivation of the beam propagation in the fourth band only one peak is expected in the measurement. Instead, two peaks R1 and R2 (and B1 and B2, respectively) are observed which both reflect the beam refraction behavior as derived from the theory. The first peak is located at $\tilde{\nu} = 1500 \text{ cm}^{-1}$ ($\omega a/2\pi c = 0.3$) and the second one at $\tilde{\nu} = 1550 \text{ cm}^{-1}$ ($\omega a/2\pi c = 0.31$). The line plot of the band structure in Fig. 5.7 reveals that in $\Gamma - A$ direction band three and four are degenerated while they are slightly separated in $\Gamma - X$ direction. This can be seen in the EFC plots of these bands as well (Figs. 5.8 and 5.9): They are looking nearly the same in their shape but the diameter of the EFCs in $\Gamma - X$ direction of the third band are smaller compared to the fourth band. Due to their similar shape the beam propagation behavior resembles that shown in Fig. 5.8. The only difference is that due to their reduced size in the $\Gamma - X$ direction the same beam propagation behavior takes place at slightly lower frequencies. The experimentally observed difference of 50 cm^{-1} between the two peaks fits very well with an offset of $\omega a/2\pi c = 0.01$ determined from the geometrical construction. However, the absolute position of the peaks is shifted by a value of 0.02 to 0.03 towards higher frequencies in the experiment compared to the theory in agreement with the observed shift of the band gap position. Since it is not shown explicitly it should be mentioned that coupling to other bands is not possible for this frequency range and incidence angle. Although the fifth to seventh band has a large frequency overlap with the third and fourth band, no coupling to these bands is possible. In these star-like shaped bands the conservation of the momentum cannot be fulfilled for an angle of 30° since there is no intersection of the construction line with the corresponding EFC of the photonic crystal.

So far, the measurement was only qualitatively discussed. However, from the measurement of the intensity ratio a value for the beam shift can be approximated. The measured intensity ratio is equal to the fraction of the circular beam area that is detected when the beam is aligned to the detector edge. A measured intensity ratio of 0.5 corresponds to a semicircle. This is the case when the beam is not refracted, i.e. $n_{\text{eff}} = 1$. For all other intensity ratios the distance of the circle center from the detector edge can be calculated. As depicted in Fig. 6.4a the detected beam fraction A_{det} is a segment of a circle (the beam spot) with radius r . Together with the area of an isosceles triangle A_{tri} it is equal to an arc of the circle A_{arc} :

$$A_{\text{arc}} = A_{\text{det}} + A_{\text{tri}} = \frac{\alpha}{360^\circ} \pi r^2 \quad (6.2)$$

The area of the triangle is

$$A_{\text{tri}} = \Delta x \cdot \sqrt{r^2 - (\Delta x)^2} = \frac{r^2}{2} \sin \alpha \quad (6.3)$$

With Eqs. 6.2 and 6.3 the angle α can be calculated which belongs to a measured intensity ratio

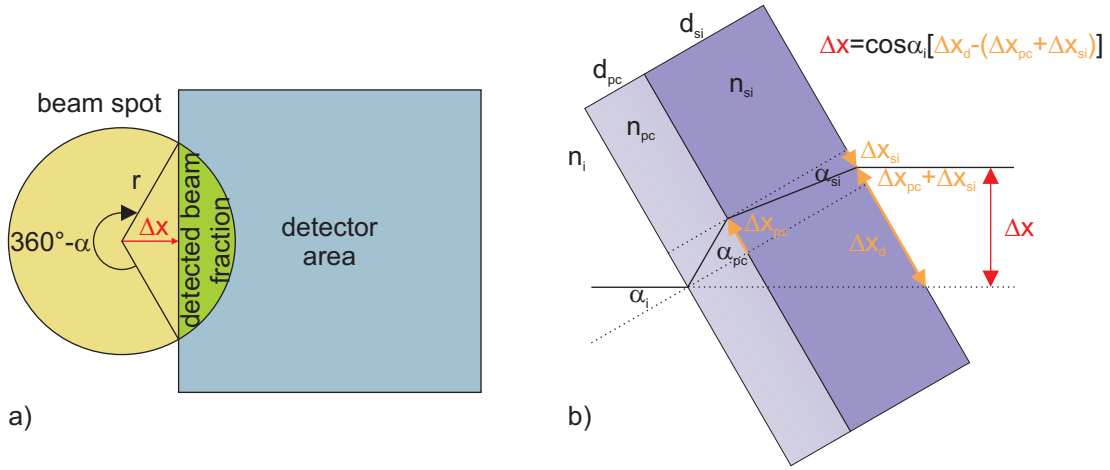


Figure 6.4: Schematics of the beam shift calculation. a) The measured intensity ratio equals a segment of a circle. From that the lateral beam shift Δx can be calculated. b) The sample consists of a photonic crystal layer with thickness d_{pc} and a bulk silicon part with thickness d_{si} . From the beam shift Δx with respect to an unrefracted beam the refraction angle α_{pc} can be derived.

A_{det} . Finally, the beam shift Δx is derived:

$$\Delta x = r \cdot \cos(\alpha/2) \quad (6.4)$$

The peaks R2 and B2 in Fig. 6.3 occur at the same wavenumber but with different heights. Thus it can be concluded that the beam alignment to the detector edge was not perfect since otherwise both peaks were centered around an intensity ratio of 0.5. Hence, the center position is set to $0.5 \cdot (0.18 + 0.73) = 0.455$ which gives a corrected intensity ratio of 0.225 and 0.775 for R2 and B2, respectively. From the formulae above an angle of $\alpha = 127^\circ$ and $\alpha = 233^\circ$ is obtained, respectively, and thus the beam shift is $\Delta x = 112 \mu\text{m}$ in the according direction.

As mentioned in the beginning of this section the measured sample consisted of the photonic crystal layer and an additional bulk silicon part for stabilization. Both layers contribute to the beam shift but the fraction induced by the bulk silicon can be subtracted and hence the beam shift induced by the photonic crystal layer only is obtained (Fig. 6.4b): At every interface the beam obeys the law of refraction (cf. Eq. 5.3). Hence, the incident beam from free space ($n_i = 1$) under an angle α_i to the surface normal is refracted under an angle α_{pc} inside the photonic crystal with an effective refractive index n_{pc} . After crossing the photonic crystal layer of thickness d_{pc} the beam displacement on the surface is

$$\Delta x_{pc} = \tan \alpha_{pc} \cdot d_{pc} \quad (6.5)$$

Thereby, the displacement is negative for negative refractive indices and vice versa. The refraction at the interface between photonic crystal and bulk silicon is only dependent on the incidence angle α_i and independent of the photonic crystal layer: $\sin \alpha_i = n_{pc} \sin \alpha_{pc} = n_{si} \sin \alpha_{si}$. After passing the bulk silicon with thickness d_{si} with a refractive index of $n_{si} = 3.42$ an additional displacement is introduced which is always positive:

$$\Delta x_{si} = \tan \alpha_{si} \cdot d_{si} \quad (6.6)$$

The overall displacement between an unrefracted beam and the refracted one is given by the difference of the displacement Δx_d and $\Delta x_{pc} + \Delta x_{si}$ whereas $\Delta x_d = \tan \alpha_i \cdot (d_{pc} + d_{si})$. Finally, the beam shift Δx is obtained by multiplying the overall displacement with the cosine of the incidence angle α_i :

$$\Delta x = \cos \alpha_i \cdot [\Delta x_d - (\Delta x_{pc} + \Delta x_{si})] \quad (6.7)$$

From these considerations the beam shift induced by the additional bulk silicon layer can be calculated to $72 \mu\text{m}$. The difference of $40 \mu\text{m}$ to the experimentally observed $112 \mu\text{m}$ is caused by the photonic crystal layer. The corresponding effective refractive index is then determined to $n_{pc} = -0.61$ or a refractive angle of $\alpha_{pc} = -55^\circ$ which clearly demonstrates the negative refraction capabilities of the designed photonic crystal. For an infinite small beam diameter and an ideal photonic crystal the beam would be refracted at a -90° angle in maximum which would lead to an infinite beam shift due to an effective refractive index of $n_{pc} = -0.5$. For the discussed incidence angle and sample geometry the maximum refraction angle of the photonic crystal that is still detectable is limited by the beam spot size to $\alpha_{pc} = \pm 83^\circ$. This can be enhanced with the setup if the thickness of the bulk silicon is further reduced.

As mentioned above, a positive refractive index larger than one also leads to a beam shift in the same direction like the negative refraction. However, its maximum in this direction is limited to a shift of $\sin \alpha_i \cdot d_{pc}$ for an effective refractive index that goes to infinity. It is half the thickness of the photonic crystal layer for an incidence angle of 30° , i.e. $11.5 \mu\text{m}$ in the case presented here. For this positive refraction behavior, however, the beam is left-handed as discussed in the preceding chapter. Hence, not only the negative refraction property of the 3D photonic crystal was measured with this setup but also the positive refraction of a beam which forms a left-handed system was shown.

Constant Frequency The second scenario that has been discussed in the preceding theory chapter is the constant frequency case (cf. Fig. 5.8 on page 71). Therefore, measurements are evaluated that have been taken for angles between 0° and 60° with 10° step width and only the intensity ratio for a single wavenumber is discussed. In Fig. 6.5 the results are presented for a wavenumber of $\tilde{\nu} = 1500 \text{cm}^{-1}$. Red crosses mark positive incidence angles while blue crosses mark negative ones. For small angles nearly no change in the intensity ratio is visible. This means that the beam shift induced by the bulk silicon for different incidence angles is fully compensated by an opposite shift induced by the photonic crystal layer. For instance, a variation of the incidence angle between -10° and 10° gives nearly the same intensity ratio for every angle in this range. The beam propagation is insensitive to deviations in the incidence angle around 0° and therefore the photonic crystal layer works as a refraction compensator for the bulk silicon layer.

For larger angles a large beam shift occurs due to the strong curvature of the EFC for these incidence angles. The intensity ratio decreases for the positive angles because the beam is shifted out of the detector area. The increase in the measured intensity ratio for incidence angles larger than 40° is explainable with coupling to higher bands. The discussion is similar to that for the constant angle scenario with the difference that higher band coupling becomes possible due to larger incidence angles at the same wavelength. Also this behavior is in accordance with the theoretical analysis.

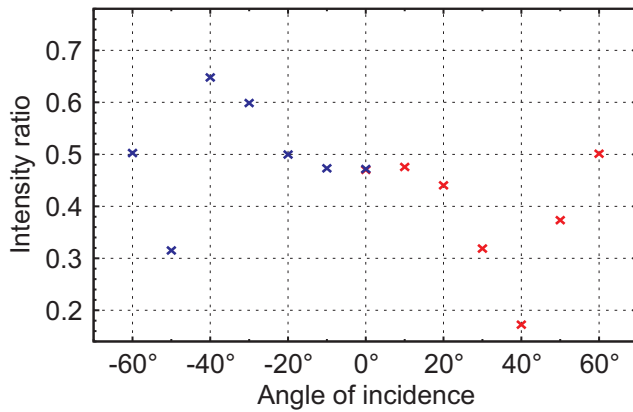


Figure 6.5: The intensity ratio measured for different incidence angles at a fixed wavenumber of $\tilde{\nu} = 1500 \text{ cm}^{-1}$. Positive angles are marked with a red cross while negative angles are marked with a blue cross.

Another point that can be verified with this measurement is the deviation of the detector alignment from its optimum value. For normal incidence an intensity ratio of 0.5 would be expected for a beam spot that is aligned with its center exactly to the detector edge. Instead, the measured one is 0.47. The deviation of 0.03 in the intensity ratio is equivalent to a displacement of $11 \mu\text{m}$ or about 4% in relative units for the beam center with respect to the detector edge. It has to be stressed that the measurement error is considerably lower than 4% for the beam shifts and angles determined in the constant angle scenario above. The reason for this is that the measurements were carried out for positive and additionally also for negative incidence angles and thus the error in the alignment could be corrected. In the former section a corrected value of 0.455 was obtained which is very close to the value of 0.47 derived from the measurement in Fig. 6.5.

With the same detector alignment the beam shift was measured for negative incidence angles as well. They are plotted with blue crosses in Fig. 6.5. The expected behavior of reversed intensity ratio is obtained for angles smaller than an absolute value of 40° . A significant difference, however, occurs for an angle of -50° . With respect to the deflection at 50° , for the -50° angle an intensity ratio above the corrected half spot intensity ratio of 0.47 would be expected. Instead, the measured intensity ratio reveals a beam shift to the opposite direction. The reason for that are inhomogeneities introduced by higher band coupling. In order to show this the spectra taken for different angles are compared to each other (Fig. 6.6). Thus, the evolution of the refraction peaks with the angle becomes more evident. It can be seen that with increasing angle the characteristic peaks which denote the strong beam shifts are moving to lower wavenumbers. Up to the second peak the curves for positive and negative incidence angle proceed symmetrical to each other. However, in the subsequent region of higher band coupling this symmetry is lost which is especially pronounced in the case of 40° and 50° . The origin of this effect cannot be assigned to the alignment of the setup since the first two peaks (R1 and B1 and R2 and B2, respectively) show a perfect correlation between positive and negative incidence angles. This is shown in the inset of Fig. 6.6. Merely, for the second peak deviations are visible for 10° and 60° . While the coupling within the third and fourth band agrees very well with the theoretical predictions, the conditions for higher frequencies and therefore for higher band coupling were not further investigated.

Nevertheless, the strong beam deflection after the second peak can be used for spectral widening of the beam. For example, at an incidence angle of -40° the intensity ratio changes from 0.68 at a wavenumber of 1504 cm^{-1} to 0.25 at 1529 cm^{-1} . With Eqs. 6.2 to 6.7 the corresponding beam shifts can be calculated. The difference between both shifts is $172 \mu\text{m}$ which means that

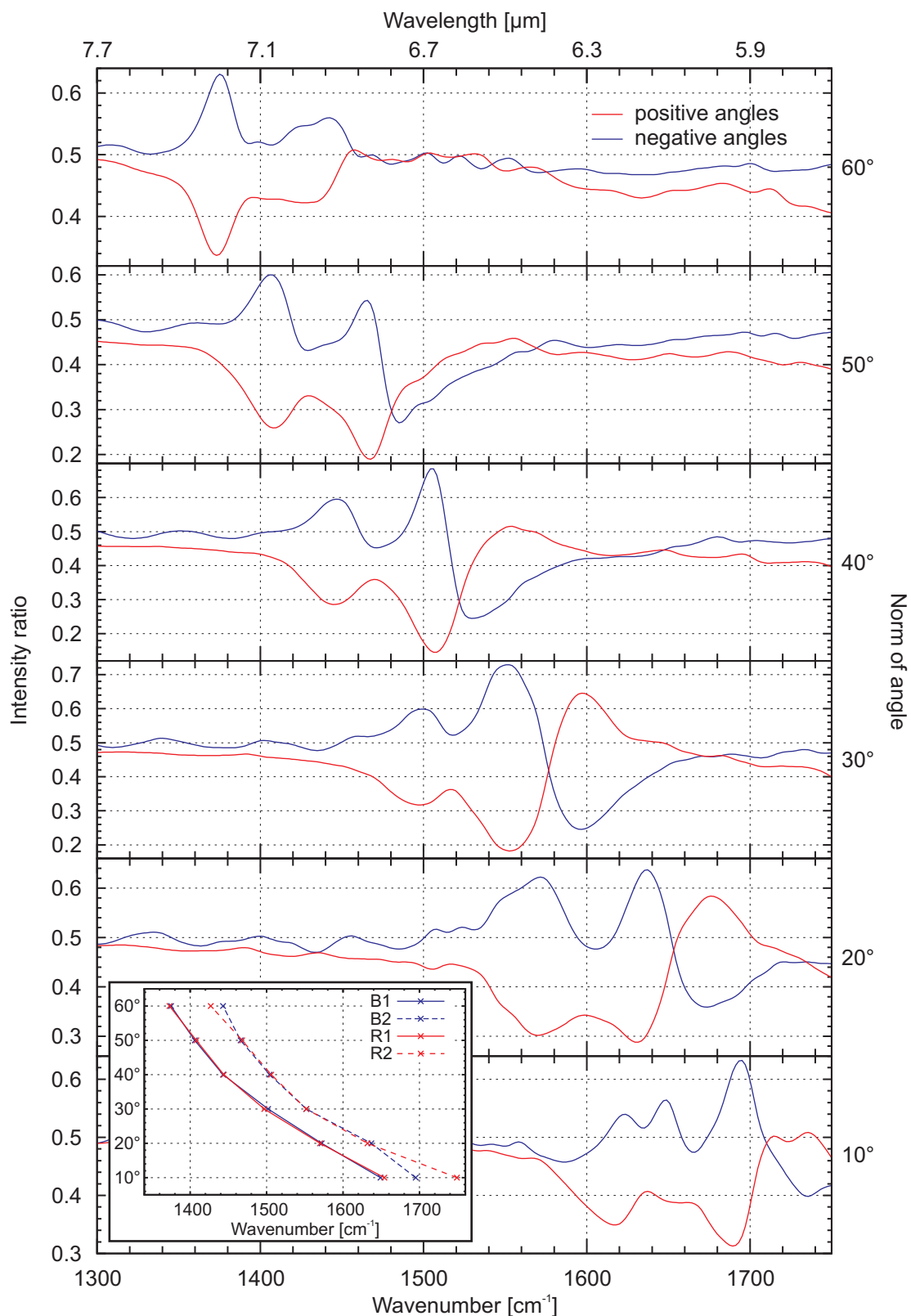


Figure 6.6: Comparative plot of the measured intensity ratios in dependence on the wavenumber for angles with an absolute value between 10° and 60°. Red lines denote positive angles while blue lines denote negative ones. In the inset the evolution of the peak positions is shown for the first two peaks R1, R2 and B1, B2, respectively.

the beam position moves by $172\text{ }\mu\text{m}$ when the wavenumber changes by only 25 cm^{-1} . It has to be stressed that this wavelength-dependent beam deflection comes only from the $23\text{ }\mu\text{m}$ thick photonic crystal layer. Due to the constant incidence angle also the beam shift induced by the bulk silicon is constant and thus it is subtracted if the difference between two intensity ratios is formed. In this particular case the $23\text{ }\mu\text{m}$ thick photonic crystal separates wavelengths between $6.65\text{ }\mu\text{m}$ and $6.54\text{ }\mu\text{m}$ on a width of $172\text{ }\mu\text{m}$. The crystal works as a prism. Thereby, this width is only dependent on the thickness of the photonic crystal and not on the distance to a plane of observation.

A last remark shall be given to the constant frequency measurement. With the mapping of different incidence angles as shown in Fig. 6.5 the EFC is redrawn in principle. Due to the fixed frequency the incident wave vector has the same length for all angles. Thus, by changing the incidence angle the wave vector passes over all points that are associated with the corresponding EFC of the photonic crystal. The measured intensity ratio which gives the deflection of the beam induced by the crystal is then correlated with the bending of the EFC. In that manner, the form of the EFC can be determined. However, this is only true as long as it can be ensured that only one beam is excited which means that there is no coupling to other sections of the same EFC and also no coupling to other bands for these incidence wave vectors.

Coupling An important point to determine the properties of a photonic device is the coupling efficiency. A wave from free space has to couple to a Bloch wave in the photonic crystal. In general, the coupling depends on the symmetry of the waves. A plane wave has always even symmetry with respect to its wave vector [150]. In contrast, Bloch modes can have even and odd symmetry and therefore the transmission efficiencies are dependent on the coupling coefficients.

In the frame of this work no detailed study of the coupling was done. For the experimental part the coupling is only important for the measurement of transmitted intensity. The determination of the beam deflection is independent of the coupling since only the detector position with respect to the transmitted beam was changed but not the parameters of the incident wave on the photonic crystal. The transmitted intensities considered in the preceding analysis were between 10% and 40%. Therefore it can be concluded that coupling of the external waves to the photonic crystal is sufficiently strong and that the observed effects are induced by the beam refraction caused by the dispersion relation of the photonic crystal [151].

Comparison Between Theory and Experiment Although the accordance between the theoretical predictions derived in the preceding chapter and the experimental characterization of the sample is excellent, some points should be mentioned shortly that mark a difference between experiment and theory. The first point to consider is the derivation of the model on which the calculations are based on. Its parameters are based on SEM micrographs of cleaved samples, averaged over several modulations and pores. Every pore of the etched sample has slight deviations from this ideal structure and thus imperfections lead to scattering. Furthermore, the model determines also the volume fractions of air and silicon in the photonic crystal. Deviations in this number lead to a mean dielectric constant different from the theoretical one and thus the bands are shifted towards higher frequencies for a higher air fraction and vice versa. This deviation is also meant to be the main component in the observed frequency offset between theory and experiment.

Another important part is that the incident beam in the experiment has a finite diameter and is not a parallel ray of light. This means that a light cone impinges on the sample rather than parallel rays with a single incidence angle. Hence, even if the frequency resolution is very good in the setup the angle resolution limits the sharpness of the peaks. This behavior can be improved by a pin hole in front of the sample. However, then also the number of scans has to be increased for each measurement which requires an even more stable background.

A last point that should be mentioned is the finite size of the photonic crystal. The calculations were performed under the assumption of an infinite crystal structure. In the experiment the sample was defined by thousands of modulations in the x- and y-direction but only eleven modulations in the z-direction. A systematic study of samples with a varying number of modulations has not yet been performed. However, the eleven modulations considered here are in accordance with photonic band gap measurements carried out on 3D crystals with twelve modulations [107] and 2D crystals with a variation of the pore rows between one and four [152] which justifies the treatment as an infinite structure.

6.4 Summary and Outlook

In this last chapter an experiment was designed which is capable of measuring the refraction properties of a photonic crystal. The dispersion properties of a 3D structure were measured and discussed and excellent agreement was found between the theoretical considerations from the preceding chapter and the experimentally measured data. Thereby, special emphasize was brought to the analysis of the third dimension, i.e. the modulated one of the macroporous silicon sample. The theoretically predicted phenomenon of negative refraction was experimentally confirmed. With negative refraction the freedom in the design of beam propagation devices can be enhanced. Based on the refraction properties further applications were shown to be feasible with this photonic crystal, e.g. angle-dispersion compensator or prism effect. An advantage of the presented method is that it can be applied in general for dispersion-related phenomena of photonic crystals.

The main conclusion that can be drawn from this chapter is that fabricated 3D macroporous silicon samples offer a quality high enough for photonic crystal applications. The experimental setup itself proved its reliability. However, the sample and beam alignment could be further improved in the future. The established method is suitable for the optical characterization of macroporous silicon samples in general and thus the treated structure does not represent a design optimized for a certain application. With the focus brought to a certain effect the properties of the photonic crystal can be optimized. For example, an increase of the air fraction in the considered structure would lead to bands that have less overlap with other bands and therefore the simultaneous coupling to several bands is prevented. In contrast, an increase in the dielectric contrast, e.g. if germanium is used instead of silicon, leads to larger EFCs and so the corresponding EFC of the incident wave would fit within the photonic crystal EFC. Thus, all-angle negative refraction can be achieved which is a necessary precondition for the proposed perfect lens applications [136]. Furthermore, the conservation of momentum can be used to access other regions of the band structure. For example, the considerations above can be repeated for wave vectors k_y different from zero or photonic crystal surfaces prepared along other symmetry directions. In that way the response of the photonic crystal can be optimized for the required specifications.

Conclusions

The subject-matter of this work was the fabrication and characterization of macroporous silicon. Fabricated in a photo-assisted electrochemical etching process macroporous silicon is a flexible material system for the preparation of ordered porous structures within two or even three dimensions. That makes this material system interesting for applications in materials science. In combination with post treatment steps the shape of the material as well as the material itself can be altered. This was shown in the second chapter of the thesis in which the combination of macroporous silicon and atomic layer deposition was investigated. Due to the self-limiting chemical reactions in atomic layer deposition, the entire porous structure can be coated homogeneously. Furthermore, the replication into different materials was proposed and proven using the example of titanium dioxide. In result, this technique is a competitive method for fabricating ordered porous structures – especially three-dimensionally shaped ones – which are flexible in their geometry and in the utilized material.

The main focus of the work was the application of macroporous silicon as a photonic crystal. For applications in the field of telecommunication a device should work in a wavelength region of $1.5\text{ }\mu\text{m}$. Based on earlier findings a 3D simple cubic arrangement of air spheres in silicon was taken as a reference design. As emphasized in chapter four the lattice constant of the structure has to be reduced to the sub-micrometer range to achieve the goal of operating at a wavelength of $1.5\text{ }\mu\text{m}$. The material at hand had a doping density of $N_D = 8 \cdot 10^{16}\text{ cm}^{-3}$ and a predefined lattice with a periodicity of 700 nm . It was shown that the controlled etching of straight pores as well as modulated pores is feasible with this material. However, for applications as a 3D photonic crystal the quality of the pore shape of the modulated samples has to be improved. In accordance with the experimental observations due to the variation of certain parameters two major factors could be isolated which have to be optimized for a better sample quality. On the one hand the importance of a uniform lithography was pointed out. On the other hand the electric conditions in the space charge region were studied and discussed in detail. The major conclusion that can be drawn from this part of the work is that especially the etching of 3D structures with a lattice constant below one micrometer is close to physical limits given by the required doping density of the material and the resulting breakdown conditions for small pore radii. From the presented calculations an optimized doping density of $N_D = 2 \cdot 10^{16}\text{ cm}^{-3}$ could be derived for a material with a lattice constant of 700 nm . Although the breakdown voltage in this optimized material would still be low, a considerable decrease in the corrosion of the pore walls can be expected. Thus, it should be possible to realize 3D photonic crystals with improved optical capabilities compared to the presented measurement of a photonic stop band in the etching direction.

Beside the photonic band gap as an important property of a photonic crystal further effects

related to the dispersion relation can be expected. A detailed investigation of this topic was given in the last two chapters. Thereby, both aspects, theory and experiment, were considered and compared to each other. In the theory chapter the necessary background was introduced to calculate and analyze the complete dispersion relation of a photonic crystal. Especially for effects based on the refraction properties of a photonic crystal the entire reciprocal space has to be examined. For comparison with etched 3D macroporous silicon samples a model was proposed to describe the dielectric function of the crystals. The calculated dispersion relation of a 3D structure was analyzed and different effects were discussed. In particular, the negative refraction could be shown to be possible with the 3D macroporous silicon sample under consideration. The proposed process of characterizing the sample geometry and of calculating its dispersion relation is thereby of general meaning since it can be applied for different designs just by changing the description of the pore geometry.

In the frame of this work the theory was closely coupled to the experimental capabilities which enabled the possibility to directly compare theoretical and experimental results. Therefore, an experiment was designed which can be used to measure the beam shift induced by the refraction in the photonic crystal layer. It was found that the experimental characterization of the macroporous silicon sample is in excellent agreement with the theoretically predicted refraction behavior. Evidence was given for the fundamental phenomenon of negative refraction which is possible in the presented 3D structure and also for other effects related to the dispersion relation like beam shaping or prism-like spectral beam widening. Thereby, special attention should be given to the fact that all the achievements in this work rely on 3D photonic crystal structures operating in the infrared region of the electromagnetic spectrum.

Finally it can be concluded, that the material system macroporous silicon is a promising candidate for the future integration of photonic technologies and devices in silicon.

Bibliography

- [1] R. Chau, B. Doyle, S. Datta, J. Kavalieros, and K. Zhang. *Integrated nanoelectronics for the future*. Nat. Mater. **6** (11), 810–812 (2007).
- [2] S. Prucnal, J. M. Sun, W. Skorupa, and M. Helm. *Switchable two-color electroluminescence based on a Si metal-oxide-semiconductor structure doped with Eu*. Appl. Phys. Lett. **90** (18), 181121 (2007).
- [3] R. J. Walters, G. I. Bourianoff, and H. A. Atwater. *Field-effect electroluminescence in silicon nanocrystals*. Nat. Mater. **4** (2), 143–146 (2005).
- [4] H. Rong, A. Liu, R. Jones, O. Cohen, D. Hak, R. Nicolaescu, A. Fang, and M. Paniccia. *An all-silicon Raman laser*. Nature **433** (7023), 292–294 (2005).
- [5] H. Rong, R. Jones, A. Liu, O. Cohen, D. Hak, A. Fang, and M. Paniccia. *A continuous-wave Raman silicon laser*. Nature **433** (7027), 725–728 (2005).
- [6] H. Rong, S. Xu, Y.-H. Kuo, V. Sih, O. Cohen, O. Raday, and M. Paniccia. *Low-threshold continuous-wave Raman silicon laser*. Nat. Photonics **1** (4), 232–237 (2007).
- [7] A. Liu, R. Jones, L. Liao, D. Samara-Rubio, D. Rubin, O. Cohen, R. Nicolaescu, and M. Paniccia. *A high-speed silicon optical modulator based on a metal-oxide-semiconductor capacitor*. Nature **427** (6975), 615–618 (2004).
- [8] W. M. Green, M. J. Rooks, L. Sekaric, and Y. A. Vlasov. *Ultra-compact, low RF power, 10 Gb/s silicon Mach-Zehnder modulator*. Opt. Express **15** (25), 17106–17113 (2007).
- [9] B. Jalali. *Teaching silicon new tricks*. Nat. Photonics **1** (4), 193–195 (2007).
- [10] A. W. Fang, H. Park, Y.-h. Kuo, R. Jones, O. Cohen, D. Liang, O. Raday, M. N. Sysak, M. J. Paniccia, and J. E. Bowers. *Hybrid silicon evanescent devices*. Mater. Today **10** (7-8), 28–35 (2007).
- [11] M. E. Davis. *Ordered porous materials for emerging applications*. Nature **417** (6891), 813–821 (2002).
- [12] A. Uhler. *Electrolytic Shaping of Germanium and Silicon*. Bell System Tech. J. **35**, 333–347 (1956).
- [13] D. R. Turner. *Electropolishing Silicon in Hydrofluoric Acid Solutions*. J. Electrochem. Soc. **105** (7), 402–408 (1958).

- [14] D. H. Everett. *IUPAC, Manual of Symbol and Terminology for Physicochemical Quantities and Units, Appendix, Definitions, Terminology and Symbols in Colloid and Surface Chemistry, Part I*. Pure Appl. Chem. **31** (4), 577 (1972).
- [15] V. Lehmann and U. Gösele. *Porous silicon formation: A quantum wire effect*. Appl. Phys. Lett. **58** (8), 856–858 (1991).
- [16] L. T. Canham. *Silicon quantum wire array fabrication by electrochemical and chemical dissolution of wafers*. Appl. Phys. Lett. **57** (10), 1046–1048 (1990).
- [17] V. Lehmann, R. Stengl, and A. Luigart. *On the morphology and the electrochemical formation mechanism of mesoporous silicon*. Mater. Sci. Eng. B **69–70**, 11–22 (2000).
- [18] V. Lehmann and S. Rönnebeck. *The Physics of Macropore Formation in Low-Doped p-Type Silicon*. J. Electrochem. Soc. **146** (8), 2968–2975 (1999).
- [19] V. Lehmann and H. Föll. *Formation Mechanism and Properties of Electrochemically Etched Trenches in n-Type Silicon*. J. Electrochem. Soc. **137** (2), 653–659 (1990).
- [20] V. Lehmann. *The Physics of Macropore Formation in Low Doped n-Type Silicon*. J. Electrochem. Soc. **140** (10), 2836–2843 (1993).
- [21] H. Föll, M. Christophersen, J. Carstensen, and G. Hasse. *Formation and application of porous silicon*. Mater. Sci. Eng. R **39** (4), 93–141 (2002).
- [22] X. G. Zhang. *Morphology and Formation Mechanisms of Porous Silicon*. J. Electrochem. Soc. **151** (1), C69–C80 (2004).
- [23] X. G. Zhang. *Electrochemistry of Silicon and its Oxide*. Kluwer Academic / Plenum Publishers, New York (2001).
- [24] V. Lehmann. *Electrochemistry of Silicon: Instrumentation, Science, Materials and Applications*. Wiley-VCH Verlag GmbH (2002).
- [25] R. L. Smith and S. D. Collins. *Porous silicon formation mechanisms*. J. Appl. Phys. **71** (8), R1–R22 (1992).
- [26] S. Matthias. *Herstellung und Charakterisierung von 3D-photonischen Kristallen aus makroporösem Silizium*. PhD Thesis, Martin-Luther-Universität Halle-Wittenberg (2005).
- [27] T. M. Geppert. *Towards Photonic Crystal-Based Spectroscopic Gas Sensors*. PhD Thesis, Martin-Luther-Universität Halle-Wittenberg (2006).
- [28] J. Carstensen, M. Christophersen, G. Hasse, and H. Föll. *Parameter Dependence of Pore Formation in Silicon within a Model of Local Current Bursts*. Phys. Status Solidi A **182** (1), 63–69 (2000).
- [29] P. Kleimann, J. Linnros, and S. Petersson. *Formation of wide and deep pores in silicon by electrochemical etching*. Mater. Sci. Eng. B **69–70**, 29–33 (2000).
- [30] J. Schilling, F. Müller, S. Matthias, R. B. Wehrspohn, U. Gösele, and K. Busch. *Three-dimensional photonic crystals based on macroporous silicon with modulated pore diameter*. Appl. Phys. Lett. **78** (9), 1180–1182 (2001).

- [31] S. Matthias, F. Müller, J. Schilling, and U. Gösele. *Pushing the limits of macroporous silicon etching*. Appl. Phys. A: Mater. Sci. Process. **80** (7), 1391–1396 (2005).
- [32] C. C. Büttner and M. Zacharias. *Retarded oxidation of Si nanowires*. Appl. Phys. Lett. **89** (26), 263106 (2006).
- [33] M. H. Klühr, A. Sauermann, C. A. Elsner, K. H. Thein, and S. K. Dertinger. *Partially Oxidized Macroporous Silicon: A Three-Dimensional Photonic Matrix for Microarray Applications*. Adv. Mater. **18** (23), 3135–3139 (2006).
- [34] H. Seidel, L. Csepregi, A. Heuberger, and H. Baumgärtel. *Anisotropic Etching of Crystalline Silicon in Alkaline Solutions*. J. Electrochem. Soc. **137** (11), 3612–3632 (1990).
- [35] W. Lee, R. Ji, C. A. Ross, U. Gösele, and K. Nielsch. *Wafer-Scale Ni Imprint Stamps for Porous Alumina Membranes Based on Interference Lithography*. Small **2** (8–9), 978–982 (2006).
- [36] L. J. Guo. *Nanoimprint Lithography: Methods and Material Requirements*. Adv. Mater. **19** (4), 495–513 (2007).
- [37] H. Masuda and K. Fukuda. *Ordered Metal Nanohole Arrays Made by a Two-Step Replication of Honeycomb Structures of Anodic Alumina*. Science **268** (5216), 1466–1468 (1995).
- [38] W. Lee, R. Ji, U. Gösele, and K. Nielsch. *Fast fabrication of long-range ordered porous alumina membranes by hard anodization*. Nat. Mater. **5** (9), 741–747 (2006).
- [39] J. M. Macák, H. Tsuchiya, and P. Schmuki. *High-Aspect-Ratio TiO₂ Nanotubes by Anodization of Titanium*. Angew. Chem. Int. Ed. **44** (14), 2100–2102 (2005).
- [40] H. Tsuchiya and P. Schmuki. *Thick self-organized porous zirconium oxide formed in H₂SO₄/NH₄F electrolytes*. Electrochem. Commun. **6** (11), 1131–1134 (2004).
- [41] I. Sieber, H. Hildebrand, A. Friedrich, and P. Schmuki. *Formation of self-organized niobium porous oxide on niobium*. Electrochem. Commun. **7** (1), 97–100 (2005).
- [42] H. Tsuchiya and P. Schmuki. *Self-organized high aspect ratio porous hafnium oxide prepared by electrochemical anodization*. Electrochem. Commun. **7** (1), 49–52 (2005).
- [43] H. Tsuchiya, J. M. Macák, I. Sieber, L. Taveira, A. Ghicov, K. Sirotna, and P. Schmuki. *Self-organized porous WO₃ formed in NaF electrolytes*. Electrochem. Commun. **7** (3), 295–298 (2005).
- [44] S.-S. Chang, S. Kurokawa, and A. Sakai. *Properties of annealed anodically etched porous Zn studied by scanning tunneling microscopy*. Appl. Surf. Sci. **217** (1–4), 50–55 (2003).
- [45] H.-C. Shin, J. Dong, and M. Liu. *Porous Tin Oxides Prepared Using an Anodic Oxidation Process*. Adv. Mater. **16** (3), 237–240 (2004).
- [46] I. Sieber, B. Kannan, and P. Schmuki. *Self-Assembled Porous Tantalum Oxide Prepared in H₂SO₄/HF Electrolytes*. Electrochem. Solid-State Lett. **8** (3), J10–J12 (2005).
- [47] C. Fang, H. Föll, and J. Carstensen. *Electrochemical pore etching in germanium*. J. Electroanal. Chem. **589** (2), 259–288 (2006).

- [48] H. Föll, S. Langa, J. Carstensen, M. Christophersen, and I. Tiginyanu. *Pores in III-V Semiconductors*. Adv. Mater. **15** (3), 183–198 (2003).
- [49] H. Föll, J. Carstensen, S. Langa, M. Christophersen, and I. M. Tiginyanu. *Porous III-V compound semiconductors: formation, properties, and comparison to silicon*. Phys. Status Solidi A **197** (1), 61–70 (2003).
- [50] Y. A. Vlasov, X.-Z. Bo, J. C. Sturm, and D. J. Norris. *On-chip natural assembly of silicon photonic bandgap crystals*. Nature **414** (6861), 289–293 (2001).
- [51] M. Deubel, M. Wegener, A. Kaso, and S. John. *Direct laser writing and characterization of "Slanted Pore" Photonic Crystals*. Appl. Phys. Lett. **85** (11), 1895–1897 (2004).
- [52] M. Campbell, D. N. Sharp, M. T. Harrison, R. G. Denning, and A. J. Turberfield. *Fabrication of photonic crystals for the visible spectrum by holographic lithography*. Nature **404** (6773), 53–56 (2000).
- [53] S. Kawata, H.-B. Sun, T. Tanaka, and K. Takada. *Finer features for functional microdevices*. Nature **412** (6848), 697–698 (2001).
- [54] M. Deubel, G. von Freymann, M. Wegener, S. Pereira, K. Busch, and C. M. Soukoulis. *Direct laser writing of three-dimensional photonic-crystal templates for telecommunications*. Nat. Mater. **3** (7), 444–447 (2004).
- [55] D. Meisel, M. Diem, M. Deubel, F. Pérez-Willard, S. Linden, D. Gerthsen, K. Busch, and M. Wegener. *Shrinkage Precompensation of Holographic Three-Dimensional Photonic-Crystal Templates*. Adv. Mater. **18** (22), 2964–2968 (2006).
- [56] S. Passinger, M. S. M. Saifullah, C. Reinhardt, K. R. V. Subramanian, B. N. Chichkov, and M. E. Welland. *Direct 3D Patterning of TiO₂ Using Femtosecond Laser Pulses*. Adv. Mater. **19** (9), 1218–1221 (2007).
- [57] X. Chen, M. Steinhart, C. Hess, and U. Gösele. *Ordered Arrays of Mesoporous Microrods from Recyclable Macroporous Silicon Templates*. Adv. Mater. **18** (16), 2153–2156 (2006).
- [58] S. Grimm, K. Schwirn, P. Göring, H. Knoll, P. T. Miclea, A. Greiner, J. H. Wendorff, R. B. Wehrspohn, U. Gösele, and M. Steinhart. *Nondestructive Mechanical Release of Ordered Polymer Microfiber Arrays from Porous Templates*. Small **3** (6), 993–1000 (2007).
- [59] L. Zhao, N. Li, A. Langner, M. Steinhart, T. Y. Tan, E. Pippel, H. Hofmeister, K.-N. Tu, and U. Gösele. *Crystallization of Amorphous SiO₂ Microtubes Catalyzed by Lithium*. Adv. Funct. Mater. **17** (12), 1952–1957 (2007).
- [60] T. Suntola and J. Antson. *US Patent*. 4 058 430 (1977).
- [61] R. L. Puurunen. *Surface chemistry of atomic layer deposition: A case study for the trimethylaluminum/water process*. J. Appl. Phys. **97** (12), 121301 (2005).
- [62] M. R. Hoffmann, S. T. Martin, W. Choi, and D. W. Bahnemann. *Environmental Applications of Semiconductor Photocatalysis*. Chem. Rev. **95** (1), 69–96 (1995).

- [63] U. Diebold. *The surface science of titanium dioxide*. Surf. Sci. Rep. **48** (5–8), 53–229 (2003).
- [64] J. Aarik, A. Aidla, T. Uustare, M. Ritala, and M. Leskelä. *Titanium isopropoxide as a precursor for atomic layer deposition: characterization of titanium dioxide growth process*. Appl. Surf. Sci. **161** (3–4), 385–395 (2000).
- [65] N. W. Choi, M. Cabodi, B. Held, J. P. Gleghorn, L. J. Bonassar, and A. D. Stroock. *Microfluidic scaffolds for tissue engineering*. Nat. Mater. **6** (11), 908–915 (2007).
- [66] J. D. Joannopoulos, R. D. Meade, and J. N. Winn. *Photonic Crystals – Molding the Flow of Light*. Princeton University Press (1995).
- [67] E. Yablonovitch. *Photonic Crystals: What’s in a Name?* Optics & Photonics News **18** (3), 12–13 (2007).
- [68] E. Yablonovitch. *Inhibited Spontaneous Emission in Solid-State Physics and Electronics*. Phys. Rev. Lett. **58** (20), 2059–2062 (1987).
- [69] S. John. *Strong localization of photons in certain disordered dielectric superlattices*. Phys. Rev. Lett. **58** (23), 2486–2489 (1987).
- [70] P. W. Anderson. *Absence of Diffusion in Certain Random Lattices*. Phys. Rev. **109** (5), 1492–1505 (1958).
- [71] E. Yablonovitch, T. J. Gmitter, and K. M. Leung. *Photonic band structure: The face-centered-cubic case employing nonspherical atoms*. Phys. Rev. Lett. **67** (17), 2295–2298 (1991).
- [72] K. M. Ho, C. T. Chan, and C. M. Soukoulis. *Existence of a photonic gap in periodic dielectric structures*. Phys. Rev. Lett. **65** (25), 3152–3155 (1990).
- [73] E. Yablonovitch and T. J. Gmitter. *Photonic band structure: The face-centered-cubic case*. Phys. Rev. Lett. **63** (18), 1950–1953 (1989).
- [74] K. Sakoda. *Optical Properties of Photonic Crystals*. Springer Berlin Heidelberg New York (2005).
- [75] S. G. Johnson and J. D. Joannopoulos. *Block-iterative frequency-domain methods for Maxwell’s equations in a planewave basis*. Opt. Express **8** (3), 173–190 (2001).
- [76] H. S. Sözüer, J. W. Haus, and R. Inguva. *Photonic bands: Convergence problems with the plane-wave method*. Phys. Rev. B **45** (24), 13962–13972 (1992).
- [77] K. M. Ho, C. T. Chan, C. M. Soukoulis, R. Biswas, and M. Sigalas. *Photonic Band Gaps in Three Dimensions: New Layer-by-Layer Periodic Structures*. Solid State Commun. **89** (5), 413–416 (1994).
- [78] E. Ozbay, E. Michel, G. Tuttle, R. Biswas, M. Sigalas, and K.-M. Ho. *Micromachined millimeter-wave photonic band-gap crystals*. Appl. Phys. Lett. **64** (16), 2059–2061 (1994).

- [79] S. Y. Lin, J. G. Fleming, D. L. Hetherington, B. K. Smith, R. Biswas, K. M. Ho, M. M. Sigalas, W. Zubrzycki, S. R. Kurtz, and J. Bur. *A three-dimensional photonic crystal operating at infrared wavelengths*. *Nature* **394** (6690), 251–253 (1998).
- [80] S. Noda, K. Tomoda, N. Yamamoto, and A. Chutinan. *Full Three-Dimensional Photonic Bandgap Crystals at Near-Infrared Wavelengths*. *Science* **289** (5479), 604–606 (2000).
- [81] F. García-Santamaría, M. Xu, V. Lousse, S. Fan, P. V. Braun, and J. A. Lewis. *A Germanium Inverse Woodpile Structure with a Large Photonic Band Gap*. *Adv. Mater.* **19** (12), 1567–1570 (2007).
- [82] O. Toader, M. Berciu, and S. John. *Photonic Band Gaps Based on Tetragonal Lattices of Slanted Pores*. *Phys. Rev. Lett.* **90** (23), 233901 (2003).
- [83] O. Toader and S. John. *Slanted-pore photonic band-gap materials*. *Phys. Rev. E* **71** (3), 036605 (2005).
- [84] N. Tétéault, G. von Freymann, M. Deubel, M. Hermatschweiler, F. Pérez-Willard, S. John, M. Wegener, and G. A. Ozin. *New Route to Three-Dimensional Photonic Bandgap Materials: Silicon Double Inversion of Polymer Templates*. *Adv. Mater.* **18** (4), 457–460 (2006).
- [85] M. Christophersen, J. Carstensen, A. Feuerhake, and H. Föll. *Crystal orientation and electrolyte dependence for macropore nucleation and stable growth on p-type Si*. *Mater. Sci. Eng. B* **69–70**, 194–198 (2000).
- [86] T. Y. M. Chan and S. John. *Blueprint for wafer-scale three-dimensional photonic band-gap synthesis by photoelectrochemical etching*. *Phys. Rev. E* **68** (4), 046607 (2003).
- [87] O. Toader and S. John. *Proposed Square Spiral Microfabrication Architecture for Large Three-Dimensional Photonic Band Gap Crystals*. *Science* **292** (5519), 1133–1135 (2001).
- [88] K. K. Seet, V. Mizeikis, S. Matsuo, S. Juodkazis, and H. Misawa. *Three-Dimensional Spiral-Architecture Photonic Crystals Obtained By Direct Laser Writing*. *Adv. Mater.* **17** (5), 541–545 (2005).
- [89] R. Hillebrand, S. Senz, W. Hergert, and U. Gösele. *Macroporous-silicon-based three-dimensional photonic crystal with a large complete band gap*. *J. Appl. Phys.* **94** (4), 2758–2760 (2003).
- [90] J. Schilling, J. White, A. Scherer, G. Stupian, R. Hillebrand, and U. Gösele. *Three-dimensional macroporous silicon photonic crystal with large photonic band gap*. *Appl. Phys. Lett.* **86** (1), 011101 (2005).
- [91] K. Busch and S. John. *Photonic band gap formation in certain self-organizing systems*. *Phys. Rev. E* **58** (3), 3896–3908 (1998).
- [92] A. Blanco, E. Chomski, S. Grabtchak, M. Ibisate, S. John, S. W. Leonard, C. Lopez, F. Meseguer, H. Miguez, J. P. Mondia, G. A. Ozin, O. Toader, and H. M. van Driel. *Large-scale synthesis of a silicon photonic crystal with a complete three-dimensional bandgap near 1.5 micrometres*. *Nature* **405** (6785), 437–440 (2000).

- [93] H. S. Sözüer and J. W. Haus. *Photonic bands: simple-cubic lattice*. J. Opt. Soc. Am. B **10** (2), 296–302 (1993).
- [94] S. W. Leonard. *Complete three-dimensional band gap in macroporous silicon photonic crystals*. Appl. Phys. Lett. **81** (16), 2917–2919 (2002).
- [95] A.-P. Hynninen, J. H. J. Thijssen, E. C. M. Vermolen, M. Dijkstra, and A. van Blaaderen. *Self-assembly route for photonic crystals with a bandgap in the visible region*. Nat. Mater. **6** (3), 202–205 (2007).
- [96] R. D. Meade, K. D. Brommer, A. M. Rappe, and J. D. Joannopoulos. *Existence of a photonic band gap in two dimensions*. Appl. Phys. Lett. **61** (4), 495–497 (1992).
- [97] P. R. Villeneuve and M. Piché. *Photonic band gaps in two-dimensional square lattices: Square and circular rods*. Phys. Rev. B **46** (8), 4973–4975 (1992).
- [98] P. V. Braun, S. A. Rinne, and F. García-Santamaría. *Introducing Defects in 3D Photonic Crystals: State of the Art*. Adv. Mater. **18** (20), 2665–2678 (2006).
- [99] S. Noda, M. Fujita, and T. Asano. *Spontaneous-emission control by photonic crystals and nanocavities*. Nat. Photonics **1** (8), 449–458 (2007).
- [100] A. Birner, K. Busch, and F. Müller. *Photonische Kristalle*. Phys. Bl. **55** (4), 27–33 (1999).
- [101] A. Birner, R. B. Wehrspohn, U. M. Gösele, and K. Busch. *Silicon-Based Photonic Crystals*. Adv. Mater. **13** (6), 377–388 (2001).
- [102] P. Kramper, M. Agio, C. M. Soukoulis, A. Birner, F. Müller, R. B. Wehrspohn, U. Gösele, and V. Sandoghdar. *Highly Directional Emission from Photonic Crystal Waveguides of Subwavelength Width*. Phys. Rev. Lett. **92** (11), 113903 (2004).
- [103] O. Painter, R. K. Lee, A. Scherer, A. Yariv, J. D. O’Brien, P. D. Dapkus, and I. Kim. *Two-Dimensional Photonic Band-Gap Defect Mode Laser*. Science **284** (5421), 1819–1821 (1999).
- [104] S. Noda. *Seeking the Ultimate Nanolaser*. Science **314** (5797), 260–261 (2006).
- [105] S. Ogawa, M. Imada, S. Yoshimoto, M. Okano, and S. Noda. *Control of Light Emission by 3D Photonic Crystals*. Science **305** (5681), 227–229 (2004).
- [106] P. Lodahl, A. Floris van Driel, I. S. Nikolaev, A. Irman, K. Overgaag, D. Vanmaekelbergh, and W. L. Vos. *Controlling the dynamics of spontaneous emission from quantum dots by photonic crystals*. Nature **430** (7000), 654–657 (2004).
- [107] S. Matthias, F. Müller, C. Jamois, R. B. Wehrspohn, and U. Gösele. *Large-Area Three-Dimensional Structuring by Electrochemical Etching and Lithography*. Adv. Mater. **16** (23–24), 2166–2170 (2004).
- [108] P. R. Griffiths and J. A. de Haseth. *Fourier Transform Infrared Spectrometry*. John Wiley & Sons (1986).

- [109] J. Schilling. *Herstellung und optische Eigenschaften von 2D- und 3D-photonischen Kristallen aus makroporösem Silizium*. PhD Thesis, Martin-Luther-Universität Halle-Wittenberg (2002).
- [110] S. Matthias, F. Müller, and U. Gösele. *Controlled nonuniformity in macroporous silicon pore growth*. Appl. Phys. Lett. **87** (22), 224106 (2005).
- [111] A. Birner. *Optische Wellenleiter und Mikroresonatoren in zweidimensionalen Photonischen Kristallen aus Makroporösem Silizium*. PhD Thesis, Martin-Luther-Universität Halle-Wittenberg (2000).
- [112] A. Loni, L. T. Canham, M. G. Berger, R. Arens-Fischer, H. Münder, H. Lüth, H. F. Arrand, and T. M. Benson. *Porous silicon multilayer optical waveguides*. Thin Solid Films **276** (1–2), 143–146 (1996).
- [113] S. M. Sze. *Physics of semiconductor devices*. Wiley (1981).
- [114] X. G. Zhang. *Mechanism of Pore Formation on n-Type Silicon*. J. Electrochem. Soc. **138** (12), 3750–3756 (1991).
- [115] I. N. Bronstein, K. A. Semendjajew, G. Musiol, and H. Mühlig. *Taschenbuch der Mathematik*. Verlag Harri Deutsch (1999).
- [116] M. Notomi. *Theory of light propagation in strongly modulated photonic crystals: Refractionlike behavior in the vicinity of the photonic band gap*. Phys. Rev. B **62** (16), 10696–10705 (2000).
- [117] S. Foteinopoulou and C. M. Soukoulis. *Negative refraction and left-handed behavior in two-dimensional photonic crystals*. Phys. Rev. B **67** (23), 235107 (2003).
- [118] S. Y. Lin, V. M. Hietala, L. Wang, and E. D. Jones. *Highly dispersive photonic band-gap prism*. Opt. Lett. **21** (21), 1771–1773 (1996).
- [119] H. Kosaka, T. Kawashima, A. Tomita, M. Notomi, T. Tamamura, T. Sato, and S. Kawakami. *Superprism phenomena in photonic crystals*. Phys. Rev. B **58** (16), R10096–R10099 (1998).
- [120] H. Kosaka, T. Kawashima, A. Tomita, M. Notomi, T. Tamamura, T. Sato, and S. Kawakami. *Self-collimating phenomena in photonic crystals*. Appl. Phys. Lett. **74** (9), 1212–1214 (1999).
- [121] V. G. Veselago. *The electrodynamics of substances with simultaneously negative values of ϵ and μ* . Sov. Phys. Usp. **10** (4), 509–514 (1968).
- [122] R. A. Shelby, D. R. Smith, and S. Schultz. *Experimental Verification of a Negative Index of Refraction*. Science **292** (5514), 77–79 (2001).
- [123] A. Grbic and G. V. Eleftheriades. *Overcoming the Diffraction Limit with a Planar Left-Handed Transmission-Line Lens*. Phys. Rev. Lett. **92** (11), 117403 (2004).
- [124] N. Fang, H. Lee, C. Sun, and X. Zhang. *Sub-Diffraction-Limited optical Imaging with a Silver Superlens*. Science **308** (5721), 534–537 (2005).

- [125] I. I. Smolyaninov, Y.-J. Hung, and C. C. Davis. *Magnifying Superlens in the Visible Frequency Range*. *Science* **315** (5819), 1699–1701 (2007).
- [126] Z. Liu, H. Lee, Y. Xiong, C. Sun, and X. Zhang. *Far-Field Optical Hyperlens Magnifying Sub-Diffraction-Limited Objects*. *Science* **315** (5819), 1686 (2007).
- [127] J. B. Pendry, D. Schurig, and D. R. Smith. *Controlling Electromagnetic Fields*. *Science* **312** (5781), 1780–1782 (2006).
- [128] D. Schurig, J. J. Mock, B. J. Justice, S. A. Cummer, J. B. Pendry, A. F. Starr, and D. R. Smith. *Metamaterial Electromagnetic Cloak at Microwave Frequencies*. *Science* **314** (5801), 977–980 (2006).
- [129] V. A. Podolskiy and E. E. Narimanov. *Strongly anisotropic waveguide as a nonmagnetic left-handed system*. *Phys. Rev. B* **71** (20), 201101–4 (2005).
- [130] A. J. Hoffman, L. Alekseyev, S. S. Howard, K. J. Franz, D. Wasserman, V. A. Podolskiy, E. E. Narimanov, D. L. Sivco, and C. Gmachl. *Negative refraction in semiconductor metamaterials*. *Nat. Mater.* **6** (12), 946–950 (2007).
- [131] V. M. Shalaev. *Optical negative-index metamaterials*. *Nat. Photonics* **1** (1), 41–48 (2007).
- [132] A. Farjadpour, D. Roundy, A. Rodriguez, M. Ibanescu, P. Bermel, J. D. Joannopoulos, S. G. Johnson, and G. W. Burr. *Improving accuracy by subpixel smoothing in the finite-difference time domain*. *Opt. Lett.* **31** (20), 2972–2974 (2006).
- [133] C. Luo, S. G. Johnson, J. D. Joannopoulos, and J. B. Pendry. *All-angle negative refraction without negative effective index*. *Phys. Rev. B* **65** (20), 201104 (2002).
- [134] X. Wang, Z. Ren, and K. Kempa. *Unrestricted superlensing in a triangular two dimensional photonic crystal*. *Opt. Express* **12** (13), 2919–2924 (2004).
- [135] S. Foteinopoulou and C. M. Soukoulis. *Electromagnetic wave propagation in two-dimensional photonic crystals: A study of anomalous refractive effects*. *Phys. Rev. B* **72** (16), 165112 (2005).
- [136] J. B. Pendry. *Negative Refraction Makes a Perfect Lens*. *Phys. Rev. Lett.* **85** (18), 3966–3969 (2000).
- [137] D. R. Smith and N. Kroll. *Negative Refractive Index in Left-Handed Materials*. *Phys. Rev. Lett.* **85** (14), 2933 (2000).
- [138] R. Gajić, R. Meisels, F. Kuchar, and K. Hingerl. *Refraction and rightness in photonic crystals*. *Opt. Express* **13** (21), 8596–8605 (2005).
- [139] N. Garcia and M. Nieto-Vesperinas. *Left-Handed Materials Do Not Make a Perfect Lens*. *Phys. Rev. Lett.* **88** (20), 207403 (2002).
- [140] P. M. Valanju, R. M. Walser, and A. P. Valanju. *Wave Refraction in Negative-Index Media: Always Positive and Very Inhomogeneous*. *Phys. Rev. Lett.* **88** (18), 187401 (2002).
- [141] S. Foteinopoulou, E. N. Economou, and C. M. Soukoulis. *Refraction in Media with a Negative Refractive Index*. *Phys. Rev. Lett.* **90** (10), 107402 (2003).

- [142] C. Luo, S. G. Johnson, J. D. Joannopoulos, and J. B. Pendry. *Subwavelength imaging in photonic crystals*. Phys. Rev. B **68** (4), 045115 (2003).
- [143] E. Cubukcu, K. Aydin, E. Ozbay, S. Foteinopoulou, and C. M. Soukoulis. *Electromagnetic waves: Negative refraction by photonic crystals*. Nature **423** (6940), 604–605 (2003).
- [144] P. V. Parimi, W. T. Lu, P. Vodo, and S. Sridhar. *Photonic crystals: Imaging by flat lens using negative refraction*. Nature **426** (6965), 404 (2003).
- [145] A. Berrier, M. Mulot, M. Swillo, M. Qiu, L. Thylen, A. Talneau, and S. Anand. *Negative Refraction at Infrared Wavelengths in a Two-Dimensional Photonic Crystal*. Phys. Rev. Lett. **93** (7), 073902 (2004).
- [146] P. T. Rakich, M. S. Dahlem, S. Tandon, M. Ibanescu, M. Soljačić, G. S. Petrich, J. D. Joannopoulos, L. A. Kolodziejski, and E. P. Ippen. *Achieving centimetre-scale supercollimation in a large-area two-dimensional photonic crystal*. Nat. Mater. **5** (2), 93–96 (2006).
- [147] Z. Lu, S. Shi, J. A. Murakowski, G. J. Schneider, C. A. Schuetz, and D. W. Prather. *Experimental Demonstration of Self-Collimation inside a Three-Dimensional Photonic Crystal*. Phys. Rev. Lett. **96** (17), 173902 (2006).
- [148] D. W. Prather, S. Shi, D. M. Pustai, C. Chen, S. Venkataraman, A. Sharkawy, G. J. Schneider, and J. Murakowski. *Dispersion-based optical routing in photonic crystals*. Opt. Lett. **29** (1), 50–52 (2004).
- [149] E. Schonbrun, Q. Wu, W. Park, T. Yamashita, C. J. Summers, M. Abashin, and Y. Fainman. *Wave front evolution of negatively refracted waves in a photonic crystal*. Appl. Phys. Lett. **90** (4), 041113 (2007).
- [150] M. Qiu, S. Xiao, A. Berrier, S. Anand, L. Thylén, M. Mulot, M. Swillo, Z. Ruan, and S. He. *Negative refraction in two-dimensional photonic crystals*. Appl. Phys. A: Mater. Sci. Process. **80** (6), 1231–1236 (2005).
- [151] R. Meisels, R. Gajic, F. Kuchar, and K. Hingerl. *Negative refraction and flat-lens focusing in a 2D square-lattice photonic crystal at microwave and millimeter wave frequencies*. Opt. Express **14** (15), 6766–6777 (2006).
- [152] S. W. Leonard, H. M. van Driel, K. Busch, S. John, A. Birner, A.-P. Li, F. Müller, U. Gösele, and V. Lehmann. *Attenuation of optical transmission within the band gap of thin two-dimensional macroporous silicon photonic crystals*. Appl. Phys. Lett. **75** (20), 3063–3065 (1999).

Acknowledgment

In the end I would like to express my gratitude to everyone who supported and assisted me with my work during the last three years.

Thank you, Prof. Ulrich Gösele for the opportunity to work at the Max Planck Institute of Microstructure Physics and for the financial support. I learned a lot from all the stories you told me that have been written by your life. Thanks for sharing them with me.

I would like to thank my supervising tutor Dr. Frank Müller for many fruitful discussions and for sensitizing me to all the multi-faceted aspects, problems and open questions related to my work.

I would also like to say thanks to the other (former) members of the photonic crystal group – namely Dr. Reinald Hillebrand, Dr. Sven Matthias, Dr. Torsten Geppert, and Klaus Mathwig – for providing me with a platform for critical discussions of my work and the results and the development of continuative ideas.

I thank the ordered porous materials group of Dr. Martin Steinhart for broadening my horizon with chemistry and polymers.

For the assistance in the daily lab work I am especially thankful to Kornelia Sklarek. I could hand over a lot of the time consuming preparation procedures and organizing stuff to you.

I thank Dr. Mato Knez and Seung-Mo Lee for the sample preparation with atomic layer deposition and Matthias Geilhufe for support in the etching of samples for some collaboration partners.

I would like to thank my mentor in the IMPRS Prof. Wolfram Hergert for spending time to discuss some of my ideas in an environment outside the institute. I thank Oleksiy Kiriyyenko for the first model calculations of air spheres in silicon.

I thank Dr. Monika Kämpfe for the coordination of the IMPRS and the members of the IMPRS for numerous scientific discussions which are an extremely efficient way for progress.

I would like to say thank you to all the people helped to keep up the infrastructure, e.g. working computers, monthly salary, workshops, literature supply, sophisticated print-outs, running electron microscopes etc.

For the relaxing atmosphere outside the lab I say thank you to all the Ph.D. students sharing the same workaday problems like me and all the other people with a smile on their face.

Finally, I am thankful to all my friends for mental distraction. I would especially like to say thank you to my family and my girlfriend Claudia for personal support and motivation during my time here in Halle.

Statutory Declaration

I hereby declare that I have prepared this thesis by myself and without the use of resources other than the ones indicated in this thesis. Quotations – verbatim or with regard to content – from other sources are marked as such.

Andreas Langner

Halle (Saale), March 31, 2008

Eidesstattliche Erklärung

Ich erkläre, dass ich keine anderen als die von mir angegebenen Quellen und Hilfsmittel zur Erstellung meiner Dissertation verwendet habe. Den benutzten Werken wörtlich oder inhaltlich entnommene Stellen sind als solche gekennzeichnet.

Andreas Langner

Halle (Saale), 31. März 2008

Curriculum Vitae

Personal Information

Name	Andreas Langner
Date of birth	December 4, 1978
Place of birth	Berlin, Germany
Nationality	German
Present address	Brüderstraße 14, 06108 Halle
E-mail	alangner@mpi-halle.mpg.de

Education

10/2005 – 07/2008	Member of the International Max Planck Research School for Science and Technology of Nanostructures
03/2005 – 02/2008	Ph.D. student at the Max Planck Institute of Microstructure Physics and the Martin Luther University Halle-Wittenberg, Halle
12/2004	Diploma – equivalent to Master – at the Humboldt University, Berlin Title: “Investigations of reflective liquid crystal spatial light modulators”
11/2004	Internship at the Fraunhofer Institute for Applied Polymer Research, Golm (Potsdam)
10/1999 – 10/2004	Study of Physics at the Humboldt University, Berlin
07/1998 – 07/1999	Civilian service in mobile domestic nursing, Berlin
06/1998	High school diploma at the high school “Louis Pasteur”, Berlin (Prenzlauer Berg)

Andreas Langner

Scientific Contributions

Conferences

- ▷ A. Langner, S. Matthias, F. Müller, U. Gösele. *Shrinking three-dimensional modulated macroporous silicon down to the submicrometer range*. 5th International Conference on Porous Semiconductors – Science and Technology, Sitges – Barcelona, Spain (March 2006), *Poster*.
- ▷ A. Langner, M. Knez, F. Müller, U. Gösele. *A toolbox for porous templates based on macroporous silicon and atomic layer deposition*. 6th International Conference on Porous Semiconductors – Science and Technology, Mallorca, Spain (March 2008), *Talk*.
- ▷ A. Langner, F. Müller, U. Gösele. *Macroporous silicon as a negative refracting photonic crystal*. 6th International Conference on Porous Semiconductors – Science and Technology, Mallorca, Spain (March 2008), *Invited Talk*.
- ▷ A. Langner, F. Müller, U. Gösele. *Negative refraction in 3D photonic crystals*. E-MRS Spring Meeting, Symposium C: Frontiers in Silicon-based Photonics, Strasbourg, France (May 2008), *Talk*.

Publications

- ▷ L. Zhao, N. Li, A. Langner, M. Steinhart, T. Y. Tan, E. Pippel, H. Hofmeister, K.-N. Tu, U. Gösele. *Crystallization of amorphous SiO₂ microtubes catalyzed by lithium*. Adv. Funct. Mater. 17 (12), 1952–1957 (2007).
- ▷ S. Grimm, R. Giesa, K. Sklarek, A. Langner, U. Gösele, H.-W. Schmidt, M. Steinhart. *Non-destructive replication of self-ordered nanoporous alumina membranes via crosslinked polyacrylate nanofiber arrays*. Nano Lett. 8 (7), 1954–1959 (2008).
- ▷ H. J. Fan, S. Kawasaki, J. M. Gregg, A. Langner, T. Leedham, J. F. Scott. *Concentric Metallic-Piezoelectric Microtube Arrays in Materials Science and Technology for Non-volatile Memories*, edited by O. Auciello, D. Wouters, S. Soss, S. Hong, Mater. Res. Soc. Symp. Proc. Volume 1071, 1071-F01-07, Warrendale, PA (2008).
- ▷ A. Langner, M. Knez, F. Müller, U. Gösele. *TiO₂ Microstructures by Inversion of Macroporous Silicon using Atomic Layer Deposition*. Appl. Phys. A, published online (2008).

- ▷ A. Langner, F. Müller, U. Gösele. *Macroporous Silicon*. Textbook chapter in *Molecular- and Nano-Tubes*, Editors O. Hayden, D. Wang, K. Nielsch, Springer, *accepted* (2008).
- ▷ B. Yameen, A. Kaltbeitzel, A. Langner, H. Duran, F. Müller, U. Gösele, O. Azzaroni, W. Knoll. *Facile Large-Scale Fabrication of Proton Conducting Channels*. J. Am. Chem. Soc., *accepted* (2008).
- ▷ A. Langner, M. Knez, U. Gösele. *Herstellung von Nanostrukturen mittels Atomlagenabscheidung*. Chem. Ing. Tech., *submitted* (2008).